Nanocrystalline Cellulose: Synthesis, Characterization and Optimization for use as Microbead Pigments

Connor Farrell

Department of Chemistry
McGill University
Montreal, Quebec, Canada

Submitted June 2023

A thesis submitted to McGill University in partial fulfillment of the requirements of the degree of Master of Science in Chemistry

Table of Contents

Abstract

Pigment microparticles (microspheres) were prepared by spray drying carboxylated cellulose nanocrystals, cCNC, combined with cationic polyelectrolytes, and anionic dye molecules in water. This sustainable approach to naturally sourced pigments conforms to many of the tenets of green chemistry and engineering. The pigments were prepared from three FD&C anionic dyes. Dye binding was assisted by attraction to a cationic polyelectrolyte complex (PEC) formed between PDDA and cCNC. Hues of green, orange and purple were prepared by binary competitive coadsorption of these dyes. When dispersed by ultrasound, the PEC yielded well-dispersed suspensions of charge inverted nanocrystals, $cCNC^{+}$. The PEC "platform" was then exposed to solutions of dye molecules. The resulting metachromic PEC suspension was spray dried to yield dry powders of vibrantly colored microbeads. The microbeads exhibited spherical morphology and diameter, D50, less than a target dimension of 4 μm. Studies were undertaken to understand how the optical properties evolved when binding anionic dye molecules to the $cCNC^{+}$ platform. Zeta potential and turbidimetry were used to find the range in which the PEC was stable against flocculation. In the end, a concentration of 14% w/w PDDA was recommended to give $cCNC^{+}$ concentrations that were stable against agglomeration. Having established conditions for the stability of the $cCNC^{+}$ platform, perturbations to the optical response from the binding of the different dyes to the PEC were studied. All dyes exhibit a hypsochromic shift in the absorption maximum when bound to $cCNC^{+}$.

Pigment color was assessed according to CIELAB reflectance protocols. Reflectance spectra of the Red 40 cellulose-based microbeads were compared with those of Red 40 Lake, a commercial hydrous alumina pigment widely used in the cosmetics industry. Using a standard cosmetics industry protocol, a quantitative assessment compared the coverage and saturation. Red 40 CNC pigment at 10% dye loading was inferior in terms of saturation and coverage compared with a commercial sample of Red 40 Lake. When adjusted for an increase in the dye loading, the pigments performed equally. The adjustment was made by developing a method based on Beer's law to pinpoint how much dye might be loaded on the $cCNC^{+}$ platform. This was used to maximize dye loading without generating free dye in solution. An extensive study of Red 40 nanocellulose pigment stability was conducted as a function of time and temperature over a range of fluids commonly used to formulate pigments for color cosmetics. The study used Red 40 Lake as a standard for comparison. Overall, the two pigment classes performed similarly. The

color stability study was extended to water as a host medium. Both the cellulose microbeads and Lake pigments released dye to the host medium. Comparatively, the release of Red 40 from the cellulose sphere was quantitatively less than from the Lake. It was discovered that Blue 1 and Yellow 5 desorbed from the cellulose microbead more readily than did Red 40.

Hyperspectral imaging (HSI) was introduced to examine the spatial distribution of dyes over the surface of the CNC microbeads. The technique was also shown to provide additional insight into dye desorption and competitive binding in aqueous media. On average, dye molecules appear to be uniformly distributed over the surface of the microbeads for Red 40, Blue 1 and Yellow 5. With minor exceptions, this state holds true for binary combinations of dye. Competitive binding studies were undertaken. These studies focused on the release and uptake of Red 40 and Blue 1 from their respective homoleptic dye-microsphere complexes. Uptake of blue dye by red microbeads was favored, a situation that likely reflects in part the lower binding affinity of Blue 1 at the surface of the $cCNC^{+}$ platform. The presence of a well-defined isosbestic point in these competitive exchange reactions suggested an equilibrium between binding and release.

Résumé

Des microparticules de pigment ont été préparées par séchage par atomisation des nanocristaux de cellulose carboxylée, cCNC, combinés avec le polyélectrolyte cationique et des molécules de colorant anionique dans l'eau. Les pigments ont été préparés à partir de trois colorants anioniques FD&C. La liaison du colorant a été facilitée par l'attraction d'un complexe polyélectrolyte cationique (CPE) formé entre PDDA et cCNC. Des teintes des couleurs diffèrent ont été préparées par coadsorption compétitive binaire de ces colorants. La suspension de CPE métachromique résultante a été séchée par atomisation pour donner des poudres sèches de microbilles de couleurs vives. Les microbilles avaient une morphologie sphérique et un diamètre, D50, inférieur à une dimension cible de 4 μm. Des études ont été entreprises pour comprendre comment les propriétés optiques évoluent lors de la liaison des molécules de colorant anionique à la plateforme $cCNC^{+}$. Le potentiel zêta et la turbidimétrie ont été utilisées pour trouver qu'une concentration de 14% p/p PDDA a été recommandée pour obtenir des concentrations de $cCNC^{+}$ stables contre l'agglomération. Cela étant, les perturbations de la réponse optique à la liaison des

différents colorants au CPE ont été étudiées. Tous les colorants présentent un décalage hypsochromique dans le maximum d'absorption lorsqu'ils sont liés à $cCNC^+$.

Les spectres de réflectance des microbilles à base de cellulose Rouge 40 ont été comparés à ceux du Rouge 40 Laque, un pigment commercial d'alumine hydratée largement utilisé dans l'industrie cosmétique. En utilisant un protocole standard de l'industrie cosmétique, une évaluation quantitative a comparé la couverture et la saturation. Le pigment Rouge 40 CNC à 10% de charge de colorant était inférieure en termes de saturation et de couverture par rapport de laque. Après ajustement en fonction d'une augmentation de la charge de colorant, les pigments ont donné des résultats équivalents. L'ajustement a été effectué en développant une méthode basée sur la loi de Beer pour déterminer la quantité de colorant qui peut être chargée sur la plateforme $cCNC^+$. Cela a permis de maximiser la charge de colorant sans générer de colorant libre dans la solution. Une étude approfondie de la stabilité en fonction du temps et de la température du pigment Rouge 40 CNC par rapport à son Laque respectif ont révélé que les deux types de pigments se comportaient de manière similaire. L'étude sur la stabilité de la couleur a été étendue à l'eau comme milieu hôte. Les microbilles de cellulose et les pigments laque ont libéré le colorant dans le milieu hôte. Comparativement, la libération de Rouge 40 à partir de la sphère de cellulose était quantitativement inférieure à celle du laque. Il a été découvert que le Bleu 1 et le Jaune 5 se désorbaient plus facilement de la microbille de cellulose que le Rouge 40.

L'imagerie hyperspectrale (IHS) a été introduite pour examiner la distribution spatiale des colorants sur la surface des microbilles CNC. Cette technique a également permis d'obtenir des informations supplémentaires sur la désorption des colorants et la liaison compétitive en milieu aqueux. En moyenne, les molécules de colorant semblent être uniformément réparties sur la surface des microbilles pour tous les colorants. À quelques exceptions près, cet état est vrai pour les combinaisons binaires de colorant. Des études de liaison compétitive ont été entreprises. Ces études se sont concentrées sur la libération et l'absorption de Rouge 40 et Bleu 1 à partir de leurs complexes colorant-microsphère homoleptiques respectifs. L'absorption du colorant bleu par les microbilles rouges ont été favorisées, une situation qui reflète probablement en partie la plus faible affinité de liaison du Bleu 1 à la surface de la plateforme $cCNC^+$. La présence d'un point isobestique bien défini dans ces réactions d'échanges compétitives suggèrent un équilibre entre la liaison et la libération.

Acknowledgments

I would like to thank, first and foremost, Professor Mark Andrews for his support throughout my undergraduate, and Master's studies. The inorganic chemistry course I completed in the second year of undergrad gave me the confidence required to strive to complete a graduate degree. The help provided to me throughout our time together has allowed me to improve and achieve things I previously thought impossible.

I would like to also thank all the previous Andrews' group members whose research I continued. The help provided by Xining Chen, Jialin Meng, Tim Morse, Monika Rak, Mary Bateman, and Alicia Wu, enabled me to launch my studies quickly. To all the current group members, Dr. Somayeh Sharafi, Dr. Liliane Samara, and Madelaine Wolff, thank you for your support and help throughout my thesis research.

Lastly, I thank my parents, and family for the support they continually gave to me through my education. I am incredibly privileged to have so much support in all fields I decide to pursue.

Contributions

The thesis was written entirely by Connor Farrell. Dr. Andrews edited all chapters. Dr. Somayeh Sharafi assisted in making the pigments. Scanning electron microscope SEM images and zeta-potential measurements were provided by Dr. Sharafi, who also collaborated on the time series stability tests. High-resolution SEM images were provided by Dr. Xining Chen. Hyperspectral imaging (HSI) data were acquired with the collaboration of McGill undergraduate student, Alessandro Busa. HSI data for the release and uptake of multiple pigments were obtained in collaboration with Madelaine Wolff (M.Sc. student, Andrews group), and Dr. Andrews.

List of Figures

List of Tables

Chapter 1- Introduction

1.1 Cellulose

Cellulose is the most abundant planetary organic polymer material. It is a key component for a third of advanced plants including wood, cotton, and flax. Cellulose comprises approximately 40 – 60 wt. % of dry wood and 90 % of raw cotton.[1] It is also produced by tunicates and some types of bacteria.[1, 2]

Cellulose is a hierarchical material that is assembled by combining linear chain polysaccharides of *D*-glucose monomers. Its physical properties arise from the different structural allomorphs and assemblies of elementary microfibrils that emerge as a result of hydrogen bonding among the polymer chains. As shown in Figure 1.1 below, two anhydroglucose rings comprise the repeat unit for a cellulose polymer. Anhydroglucose describes a glucose molecule that has undergone a dehydration reaction to form the cellulose polymer.[3] A β-1-4 glycosidic bond links the *D*-glucose units together. The symbol β indicates that the oxygen bound to the anomeric carbon at position 1 is in the axial position, and 1- 4 indicates the ether linkage between carbon 1 and 4 on the pyranose ring.[4]

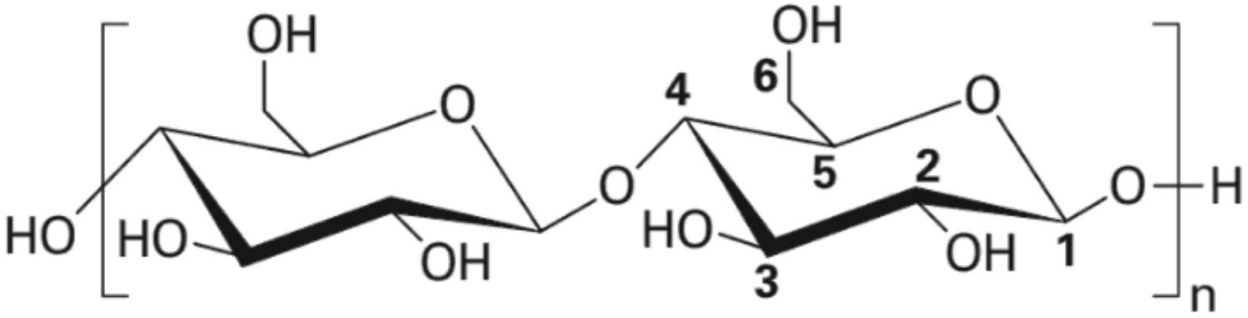

Figure 1.1: Basic chemical structure of cellulose, with the numbering system for one of the anhydroglucose units of cellulose.[5]

The abundant hydroxyl and oxygen groups result in van der Waals and intermolecular hydrogen bonds that drive the stacking of multiple chains during the biosynthesis of cellulose. This results in protofibrils that in turn combine to make microfibrils. The significant inter and intra-chain interactions give the cellulose fibrils high axial stiffness. Within the fibrils, there are regularly spaced highly disordered (amorphous) and highly ordered (crystalline) domains.[4, 6] An idealization of the two types of domain (region) is shown below in Figure 1.2 A. The percentage

of the crystalline domain in cellulose depends on the source; for bacteria and algae, it can reach 100 %, while the percentage from higher plants is lower.[7]

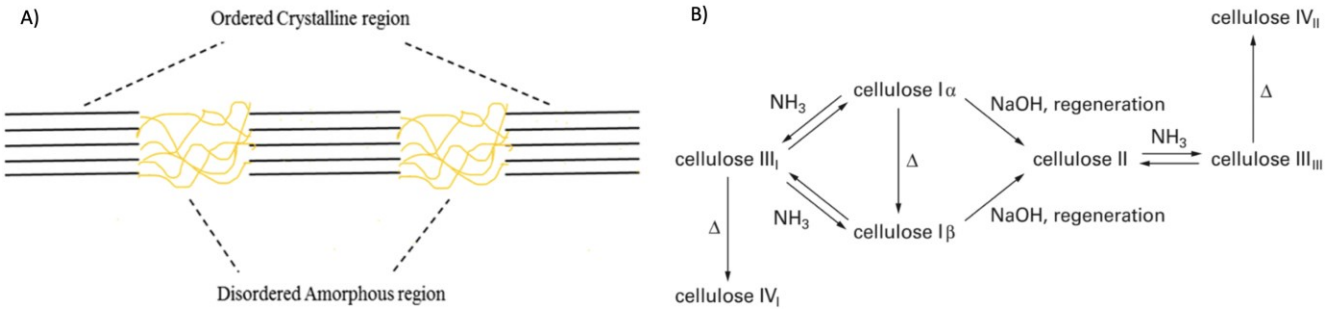

Figure 1.2: A) Crystalline and amorphous regions of cellulose.[6] B) Interconversion of the cellulose polymorphs.[5]

Cellulose I is the native allotrope. Its structure is defined by intrachain, interchain, and intersheet hydrogen bonding and van der Waals interactions. Chains of cellulose I align parallel to one another and are detectable in two main crystal structures: cellulose Iα (triclinic) and cellulose Iβ (monoclinic). Although both crystalline forms of cellulose I are present together, cellulose Iβ predominates in higher plants, whereas cellulose Iα abounds in bacterial and algal cellulose.[8] The physical properties of cellulose are determined by the underlying crystalline and amorphous nanostructure. The large number of hydrogen bonds means that cellulose can adopt other allotropic forms, identifiable by their different crystal packing. Accordingly, these polymorphs are cellulose II, III, and IV. The polymorph type depends on the source. Iβ is the major form in wood celluloses and cotton. It is possible to change the polymorph by chemical and physical treatments.[7] In contrast to naturally occurring cellulose I, cellulose II is a synthetic material that is produced when cellulose polymers are allowed to recrystallize with anti-parallel chains from solution. Interconversions among the allotropes are shown in Figure 1.2 B above. In this thesis, we use cellulose type I nanocrystals derived from the native cellulose I material that has been processed into a form of dissolving pulp called Temalfa 93.

1.2 Cellulose Nanocrystals

The term cellulose nanocrystal (CNC) is the preferred nomenclature in the hierarchy of TAPPI nomenclature.[9] One of the primary applications for CNC use is as a reinforcement for polymer nanocomposites. The polymer nanocomposites possess unique quality due to the high surface area of the reinforcing material, and their small size. The mechanical properties of the

polymer system are improved by adding CNC as a load-bearing component.[10-12] The resulting nanocomposites can be used to make different types of paper, biomimetic foams, flexible flat panel displays in electronics, and water repellents.[13-16] CNC has also been deployed in biomedicine as hydrogels, tissue engineering scaffolds, and wound healing patches.[12] CNC is known to be biocompatible. When labelled with fluorescent molecules, it has been used for biosensing, bioassay, and bioimaging applications, especially in studies of the interactions of living cells with CNC *in vivo*.[17, 18] Elsewhere, the small size, biocompatibility, and hydrophilicity of CNC encourage its development for drug delivery.[19] For example, the Coulombic potential associated with negatively charged CNC can be used to bind cationically charged drug molecules.[20] Surface modification of CNC with chitosan oligosaccharide encourages binding and release of nonionized or hydrophobic drugs.[21] In the next paragraphs, we provide some background about the methods used to make different types of CNC and some of the essential properties that make carboxylated CNC of interest to this thesis.

CNC particles are obtained from cellulose microfibrils by subjecting them to chemical, mechanical, or enzyme treatment. The nanoparticles are typically 5 to 10 nm in width by 100 to 300 nm in length, though the dimensions depend on the processing method and the cellulose biosource. As noted earlier, CNC particles are predominantly highly crystalline segments that have been excised from the alternating amorphous and crystalline domains of bulk cellulose.[12, 22] Mechanical processes like high-intensity ultrasonic treatment or high-pressure homogenization are effective in the extraction of cellulose microfibrils.[12] Chemical conversion of cellulose microfibrils into CNC dominates over the use of the mechanical methods; chemically processed CNC exhibits higher crystallinity whilst requiring less energy than mechanical processing.[23] In 1951, Ranby prepared the first colloidal suspension of cellulose by sulfuric acid-catalyzed degradation of cellulose fibers.[24] The sulfuric acid process was subsequently developed to yield sulfated CNC.

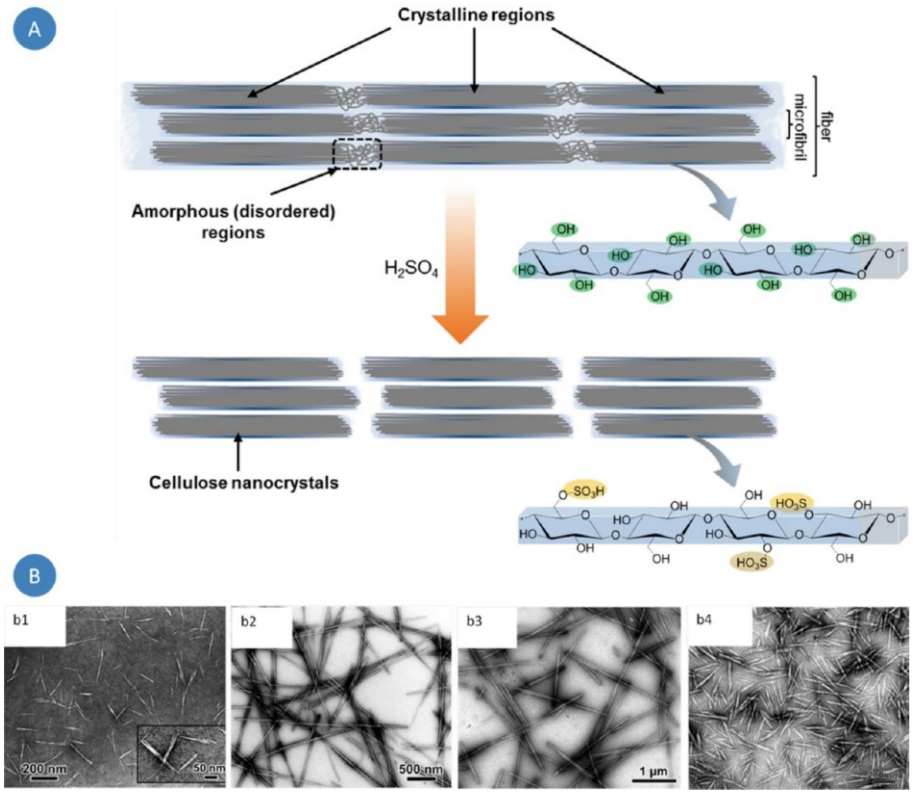

Figure 1.3: A) Schematic of idealized cellulose fibers, showing the cellulose nanocrystals after sulfuric acid hydrolysis including the sulfate half ester surface (sulfate) groups formed by conversion of hydroxyl at the C6 position on the pyranose ring. B) TEM micrographs of dispersion of cellulose nanocrystals from different sources.[25]

Chain disorder in the amorphous regions between the nanocrystalline domains simplifies attack and hydrolysis by strong acids. The crystalline domains resist attack owing to physical restrictions on accessing the cellulose chains. Figure 1.3 illustrates the process to make sulfated CNC from concentrated sulfuric acid. TEM images of typical nanocrystals are shown at the bottom of the figure. Hydrolysis with sulfuric acid results in a rapid decrease in the degree of polymerization, reaching a cut-off level called the level-off degree of polymerization (LODP). The LODP depends on the source of cellulose.[12] Nanoparticles with a diameter of 5-6 nm can be prepared by enzymatic hydrolysis in combination with mechanical shearing and homogenization.[26] Bacteria-derived CNC exhibits better thermal and mechanical properties than CNC obtained by sulfuric acid hydrolysis.[27] By increasing the chemical processing temperature, shorter CNC particles are obtained.[28, 29] An enormous literature including review articles and monographs has evolved that focuses on chemical modification of the surface of CNC.[5] The reader is referred to the literature for details. Here we emphasize chemical modifications that are

simultaneous with the preparation of CNC, i.e., methods that do not involve isolation and post synthetic surface modification. These are illustrated in Figures 1.3 and 1.4.

We have already alluded to the formation of sulfate esters (Figure 1.3) via the sulfuric acid process.[4] The degree of sulfation is increased with longer treatment time, though this can degrade the crystallinity and reduce the degree of polymerization.[30] Less common is the use of hydrochloric acid, which enhances surface hydroxyl.[31] Hydroxylated surfaces can also be produced by purely mechanical means, such as high-pressure homogenization.[4] Digestion by Fischer-Speier esterification with acetic acid yields acetylated surfaces.[22, 32] 2,2,6,6-tetramethyl-piperidinyl-1-oxyl (TEMPO) oxidation will selectively oxidize primary alcohol groups present in cellulose to produce a carboxylic acid decorated surface.[33]

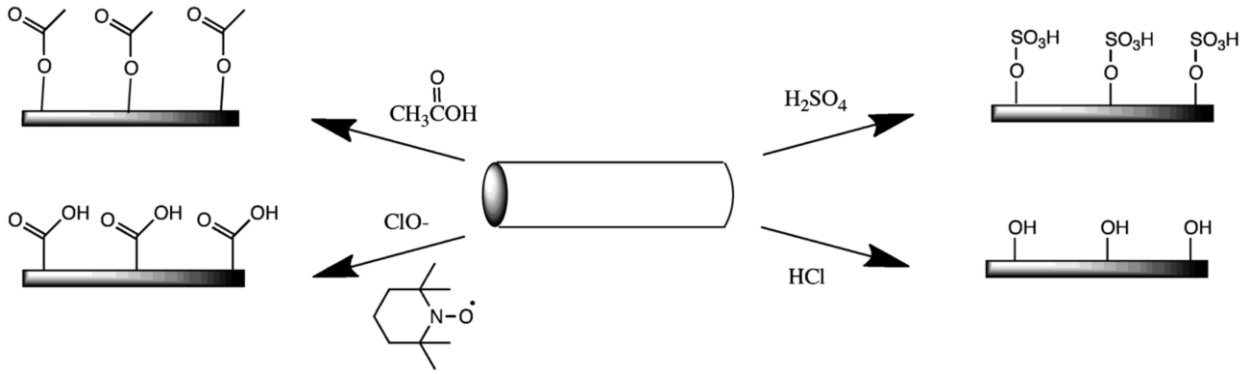

Figure 1.4: Common routes to modified CNC that provide distinct surface chemistries. Sulfuric acid treatment yields sulfate esters (top right), hydrochloric acid treatment yields hydroxyl (bottom right), acetic acid results in acetyl (top left), and TEMPO mediated hypochlorite treatment provides carboxylic-acid functionalities (bottom left).[4]

Motivated by a desire to produce a more sustainable pathway to the much-desired carboxylic acid functionalized CNC material, the Andrews group developed and patented a catalyst-free dilute aqueous hydrogen peroxide process.[34] The process subscribes to many of the 24 principles of Green Chemistry and Engineering, a precis of which is given in the reference by Tang et al. [35]. In respect of the 12 principles of green chemistry, the process yields predominantly dilute sugars and water as waste (minimizes waste). It uses renewable materials (wood products and wood waste). It conserves entropy (reduces energy consumption – does not disrupt the cellulose crystal lattice). It exhibits atom economy (carboxylic acid functionalities are introduced simultaneously during CNC production). The product is certified biodegradable (Meets OECD 310d test specifications). The product is safe and non-toxic. It uses only water as the solvent

medium. The process has been scaled to fully sustainable manufacturing, where it conforms to the principles of green engineering.

The process to make carboxylated CNC (cCNC) uses dissolving pulp, Temalfa 93, as feedstock for nanocrystal preparation. The pulp is supplied by Rayonier Advanced Materials, Canada, from its manufacturing site in Temiscaming, Quebec. The mechanism of peroxide oxidation of the native cellulose is unknown, though it is thought that peroxide radicals are instrumental. These are formed by UV light, heat, or both.[36] By TEM, the average length of the cCNC from the dissolving pulp is 200 nm and the width is 10 nm. These dimensions are similar to those obtained from the same grade of pulp by sulfuric acid hydrolysis.[36]

cCNC crystallinity depends only weakly on the cellulose feed source. By x-ray powder diffractometry, the crystallinity index of cCNC is 70-75 % when sourced from dissolving pulp or sawdust (biomass), or whether heat or UV light supplements the process. Within error, the crystallinity index is identical to that obtained when Temalfa 93 pulp is treated with sulfuric acid.[36] The crystallinity index of cCNC is in the center of the range of 54 -88 % found for CNC made from different biosources.[4]

As shown above, in Figure 1.4, methods to make CNC can alter its surface chemistry. These methods can affect the important property of surface charge, which is essential to regulate the dispersion of CNC particle types in aqueous media. Nanocrystals obtained by the sulfuric acid process are functionalized with sulfate moieties that introduce a negative electrostatic potential. This potential promotes dispersion and prevents the nanoparticles from agglomerating.[22] Similarly, carboxylate moieties present in cCNC lead to stable particle dispersions. The zeta potential of CNC obtained by the sulfuric acid and hydrogen peroxide methods are -61 mV and -49 mV, respectively.[36] Both values are well above the ±30 mV required to favor a stable colloidal suspension.[37] As determined by potentiometric titration, the carboxylate content of cCNC lies between 0.14 and 0.17 mmol/g, depending on the feedstock source.[36] A cCNC-based pigment can be made through the formation of a polyelectrolyte complex to enable the binding of anionic dyes to cCNC.[36] cCNC based pigments and their properties are the subject of this thesis.

1.3 Polyelectrolyte complexes

cCNC particles are the solid state nano platform used to make micron scale spherical pigment particles by spray drying.[36] Microbeads prepared this way from "pristine" (not chemically modified) cCNC emerge as a free-flowing white powder. cCNC is converted to a pigment by combining the nanocrystals with dye molecules to achieve the desired color. A key challenge is to bind the dye without introducing covalent bonds. This criterion was imposed because the target industries, like food, agriculture, cosmetics, paints, print and coatings, all seek performing pigments that are sustainably sourced and that utilize "off the shelf" components approved by certification bodies - certified FDA, EU, COSMOS approved dyes, and "benign" biodegradable and renewable substrates like cellulose. Covalent chemistry can be avoided by using a "trick" from the dye industry: use hydrogen bonding, van der Waals and coulombic forces that are commonly used to dye cotton, i.e., cellulose! Dyes currently approved for use in food and cosmetics are often anionic.[38] Because the cCNC surface is negatively charged (zeta potential -49 mV), binding of anionic dye molecules must overcome a repulsive coulombic potential. For this reason, the charge on cCNC must be converted from negative to positive. This can be accomplished by transforming cCNC into a polyelectrolyte complex (PEC).

A polyelectrolyte (PE) is a polymeric molecule that has repeating ionizable units that can become highly charged when placed in an ionizing solvent like water. The PEs are coupled with counterions to preserve their electro-neutrality [39, 40] The ionic groups, repeating units, and counter ions present in a PE determine its water solubility and electrical conductivity. These properties are strongly dependent on the pH, ion content, and solvent permittivity.[40] The properties of PEs can be modulated through the dissociation of their ionic groups triggered by the introduction of other ionic moieties like dyes.[41, 42] Some of the physical properties that can be modified are viscosity, diffusion coefficient, pH, ionization constant and ionic strength.[40] The relationships between the above properties give the PEC its tunable characteristic, as shown in Figure 1.5 below. It means control over the conditions of the PEC is essential for having the desired product. The aggregation (flocculation) properties of a polyelectrolyte are relevant to this thesis. Briefly, the inter-PE association is governed by charge screening and molecular weight. Charge screening refers to the process of fully or partially neutralizing the coulombic charge on the PE with large or small entity ions of opposite charge. Owing to like-charge repulsion, a highly charged PE will be more or less fully extended in solution. Changes in pH or the addition

of oppositely charged ions induce the polymer first to adopt a random coil configuration and then ultimately to aggregate by forming polyelectrolyte complexes (PECs) either with itself or with some additive. Aggregation is marked by an increase in the viscosity of the solution.[43]

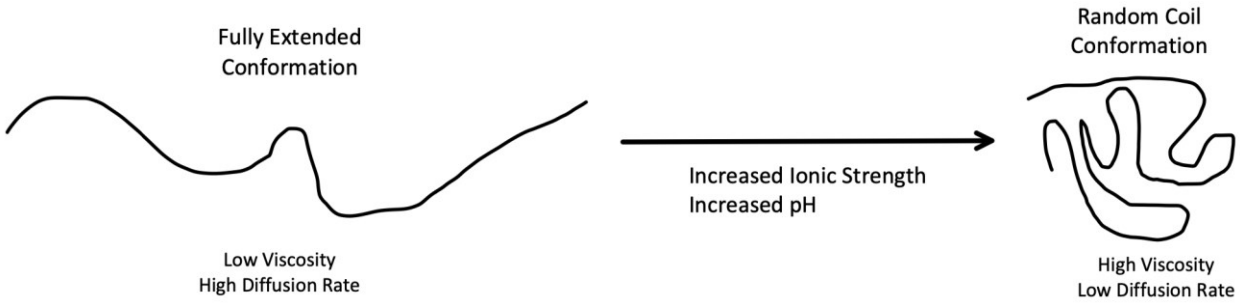

Figure 1.5: Solution properties' influences on polymer conformation and characteristics.

Separately, dyes and PE have versatile applications.[40] When combined with opposing charges, the two can interact to create a polyelectrolyte complex. The PEC can flocculate or remain in solution, depending on the charge screening, among other factors. A polyelectrolyte complex arises when the ionized polymer forms a complex with an oppositely charged species, in our case a dye. The intermolecular interactions, which can also include van der Waals and hydrogen bonding forces, yield non-permanent networks that can dissociate according to pH and ionic strength. Generally, PECs are biocompatible making them useful as pharmaceutical excipients, like use in drug compounding, delivery and release.[41, 44] Dye-PECs are useful to separate dyes from wastewater. As a pernicious problem in the dye industry, wastewater remediation by flocculation and filtration is generally difficult.[45, 46] The problem of dye removal by the formation of a PEC can be turned on its head by intentionally binding the dye to an appropriately designed cellulose matrix. This is the paradigm we use to make bio-based pigment particles from cCNC.

As noted above, PE properties depend on solution conditions like pH and ionic strength. Accordingly, this thesis explores in part the importance of adjusting the properties of the polycation so that the coulombic interaction can be partitioned between the cellulose nanocrystal PEC and the dye. By "partitioned" we mean the following. Our objective is to decorate individual cellulose nanocrystals with anionic dye. Success in doing so relies on finding a way to invert the negative charge on cCNC with cationic polyelectrolyte *without* causing flocculation. We theorize that this can be accomplished by binding just enough polyelectrolyte to surround a

nanocrystal whilst avoiding charge neutralization. In chapter 2 we describe how we use variations in polyelectrolyte concentration, ultrasound for dispersion, and diafiltration to remove salts from the cCNC-PE complex to create charged cCNC-PE entities called $cCNC^{+}$. The polyelectrolyte is poly(diallyldimethylammonium chloride) (PDDA). Diafiltration leaves a slight excess positive potential on the $cCNC^{+}$ whose repulsive potential is sufficient to disperse the particles and yet still bind anionic dye. The dye binding process relies not only on charge, but also on balances of hydrogen bonding, pKa, and van der Waals interactions.

There are three principal components to the pigment particle we investigated in this thesis. The first component comprises carboxylated cellulose nanocrystals (cCNCs) as described in section 1.2 and further in chapter 2.[36] The second component is the cationic polyelectrolyte, poly(diallyldimethylammonium chloride) (PDDA). The structure of PDDA is shown below in Figure 1.6. It is a polycation owing to the quaternized nitrogen repeat unit. The homopolymer is produced by an aqueous phase free radical addition reaction of diallyldimethylammonium chloride (DADMAC). Because PDDA is water soluble it is widely used in commercial products that are generated by aqueous phase processing.[47] PDDA therefore promotes the binding of anionic dye molecules. The common use and prior approval by the FDA are the reasons for the selection of PDDA as the polycation.

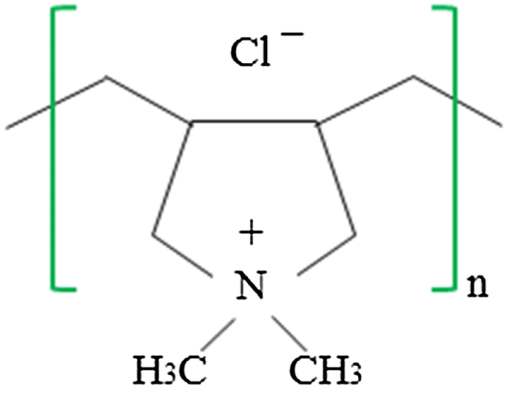

Figure 1.6: Structure of poly(diallyldimethylammonium chloride) (PDDA)[48]

In this thesis, we show that the addition of PDDA to form the cCNC-PDDA PEC ($cCNC^{+}$) must be done with precision. In our experience, slow additions of PDDA to suspensions of cCNC induce the zeta potential to gradually increase and approach zero. At zero potential, half of the surface of the cCNC entity is covered by cationic charge (PDDA) and the other half with anionic charge (carboxyl groups). The opposite charges attract and lead to irreversible aggregation

(flocculation).[49] It is necessary to avoid flocculation since our intention is to bind dye molecules to individual nanocrystals. To avoid flocculation, an amount of polymer calculated to completely coat the nanocrystal surface is added rapidly to ensure that electrostatic repulsion instead of attraction occurs between the particles. Sonication then disperses the cCNC so that the particles end up coated with PDDA without flocculating.[50] Upon the addition of the PDDA the reaction becomes visibly cloudy. Trial and error showed that a concentration of 0.5% w/v $cCNC^+$ should be maintained to avoid flocculation.[36] Having "built" the $cCNC^+$ platform one is then in a position to bind dye to the cationic cCNC-PDDA PEC. The nanoplatform is therefore uniquely positioned to accept the co-adsorption of different dye molecules so the "molecular mixing" in this manner has the potential to create a gamut of hues. The method is akin to dying cotton textiles but differs in that the nanoarchitecture of the PEC-dye complex comes into play together with the optical properties (scattering and refractive index) of the PEC.

1.4 Pigments

Pigments are compounds that are insoluble or nearly insoluble in fluid media and that bring color by virtue of the dye component or inorganic component that shows wavelength-selective absorption and scattering.[36] Pigments can be organic or inorganic. Phthalocyanine pigments are examples of insoluble *organic* compounds based on an internal 16-membered ring of alternate carbon and nitrogen atoms consisting of four iso-indole units. Chromium oxide, magnetite, hematite, lapis lazuli and so-called "Lakes" are examples of inorganic pigments. Unlike metal oxide, silicates and sulfur-containing inorganics, Lakes consist of synthetic (petroleum-based) dyes that are bound to inorganic substrates, usually alumina hydrate salts.[38] There are seven certified Food, Drug, and Cosmetic (FD&C) approved dyes for use in foods in the US. In this thesis we explored FD&C Yellow No. 5 (tartrazine), Red No. 40 (allura red), and Blue No. 1 (brilliant blue).[38] These were selected so that the dye, nanocrystal and PDDA, at least individually, comply with the most widely accepted regulatory standards. The chemical structures of these anionic dyes are shown in chapter 2, Figure 2.8. Yellow 5, and Red 40 are both azo dyes. Azo dyes currently makeup 50% of the dyes produced worldwide and a large proportion of the dyes approved by the FDA, hence their use in this thesis. Blue 1 is classified as a triphenylmethyl dye. There is pressure to replace these dyes because they and their metabolites are known to be carcinogenic and harmful to the environment.[51-53]

Naturally sourced (botanical) dyes are being explored as potential replacements for synthetic dyes, but it is naïve to think that natural dyes can be introduced as one-to-one replacements. At the risk of oversimplification, the use of natural dyes is unregulated, a state that risks abuse by companies and other entities seeking to take advantage of the growing market for natural colors. The term "natural dye" lacks a consistent definition and product safety specifications that typically comprise a harmonized regulatory framework. Chemically, most natural dyes are fugitive, meaning that they are unstable to heat, light, changes in pH, air oxidation and when formulated for markets like cosmetics, natural pigments can react with the chemical components.[54] Note that when writing here about dyes, we are not referring to pigments, which are the actual object of this thesis. Synthesis of "all-natural" *pigments* invites the development of characterization protocols that include ways to describe dye-substrate (cCNC) interactions. In our preliminary chapter 2 study of a botanically derived dye, we selected sodium copper chlorophyllin for conversion to a CNC microbead pigment. The dye is an extract from plant chlorophyll. It is a water-soluble phthalocyanine dye that combines anti-inflammatory, antibacterial, and antioxidant activities together with its intense green hue.[55]

1.5 Conclusions

This introductory chapter noted that the long period of dormancy after the Ranby discovery of cellulose nanocrystals finally resolved itself in the scaling of this specialty cellulose from the laboratory bench to the marketplace. En route, CNC was elaborated as a sulfated material via the ubiquitous sulfuric acid process. Sulfated CNC was rapidly adopted by the research community that articulated many of its attractive features based on the long history of carbohydrate chemistry. Since then, the hegemony of sulfated CNC has been challenged by new types of sulfate-free CNC based on bacterial sources and mechanical processing, and carboxylated CNC derived by TEMPO, periodate, and peroxide oxidation. The specialty carboxylated CNC (cCNC) of interest to this thesis was obtained by oxidation with dilute hydrogen peroxide. Spray drying was used to rescale the cellulose nanocrystals to microspheres. Spray drying was shown to be a viable route to pigment microbeads.

Previous studies had established that the negative potential of cCNC can be inverted from negative to positive through the formation of a polyelectrolyte complex (PEC) with the polyelectrolyte cation, PDDA. The resulting cCNC+ is a viable platform for binding anionic dye

molecules. Despite the breakthrough in making pigment particles from cCNC+, there remains a need to provide new knowledge regarding dye uptake and dye release processes, new knowledge of the factors that regulate "molecular mixing" on the cellulose nanocrystals, new knowledge of PEC formation and its impact on dye binding and release, and demonstrations of the new pigments in cosmetic formulations.

Molecular mixing at the nanoscale is exceptional in the color science literature. Nevertheless, the method required validation as to its reproducibility and potential to map out portions of the CIE color space. This thesis provides data that supports both reproducibility and the promise of an expanded color gamut.

This thesis also contrasts the performance of the cCNC-based pigments with that of commercial Lake pigments. The purpose is to benchmark the new pigments and to highlight their strengths and weaknesses when compared with commercial pigments.

This thesis describes how hyperspectral imaging provides new insight into the uptake and release of dye molecules in the pigment microbead particles. Uptake and release in this context stand as paradigms for drug delivery vehicles.

1.6 References

1. Kamide, K., *Cellulose and cellulose derivatives*. Elsevier: 2005.
2. Esa, F.; Tasirin, S. M.; Abd Rahman, N., Overview of bacterial cellulose production and application. *Agriculture and Agricultural Science Procedia* **2014,** *2*, 113-119.
3. Choudhary, V.; Burnett, R. I.; Vlachos, D. G.; Sandler, S. I., Dehydration of glucose to 5-(hydroxymethyl) furfural and anhydroglucose: thermodynamic insights. *The Journal of Physical Chemistry C* **2012,** *116* (8), 5116-5120.
4. Moon, R. J.; Martini, A.; Nairn, J.; Simonsen, J.; Youngblood, J., Cellulose nanomaterials review: structure, properties and nanocomposites. *Chemical Society Reviews* **2011,** *40* (7), 3941-3994.
5. Dufresne, A., *Nanocellulose: from nature to high performance tailored materials*. Walter de Gruyter GmbH & Co KG: 2017.
6. Rajinipriya, M.; Nagalakshmaiah, M.; Robert, M.; Elkoun, S., Importance of agricultural and industrial waste in the field of nanocellulose and recent industrial developments of wood based nanocellulose: a review. *ACS Sustainable Chemistry & Engineering* **2018,** *6* (3), 2807-2828.
7. Kovalenko, V. I., Crystalline cellulose: structure and hydrogen bonds. *Russian Chemical Reviews* **2010,** *79* (3), 231.

8. Atalla, R. H.; Vanderhart, D. L., Native cellulose: a composite of two distinct crystalline forms. *Science* **1984,** *223* (4633), 283-285.
9. TAPPI International Nanotechnology Division Roadmap for Development of International Standards for Nanocellulose. https://www.tappinano.org/media/1468/2011-roadmapfornanocellulosestandards.pdf.
10. Mathew, A. P.; Dufresne, A., Morphological investigation of nanocomposites from sorbitol plasticized starch and tunicin whiskers. *Biomacromolecules* **2002,** *3* (3), 609-617.
11. George, J.; Kumar, R.; Sajeevkumar, V. A.; Ramana, K. V.; Rajamanickam, R.; Abhishek, V.; Nadanasabapathy, S., Hybrid HPMC nanocomposites containing bacterial cellulose nanocrystals and silver nanoparticles. *Carbohydrate polymers* **2014,** *105*, 285-292.
12. George, J.; Sabapathi, S., Cellulose nanocrystals: synthesis, functional properties, and applications. *Nanotechnology, science and applications* **2015**, 45-54.
13. Svagan, A. J.; Samir, M. A. A.; Berglund, L. A., Biomimetic foams of high mechanical performance based on nanostructured cell walls reinforced by native cellulose nanofibrils. *Advanced Materials* **2008,** *20* (7), 1263-1269.
14. Henriksson, M.; Berglund, L. A.; Isaksson, P.; Lindström, T.; Nishino, T., Cellulose nanopaper structures of high toughness. *Biomacromolecules* **2008,** *9* (6), 1579-1585.
15. Nogi, M.; Yano, H., Transparent nanocomposites based on cellulose produced by bacteria offer potential innovation in the electronics device industry. *Advanced materials* **2008,** *20* (10), 1849-1852.
16. Bayer, I. S.; Fragouli, D.; Attanasio, A.; Sorce, B.; Bertoni, G.; Brescia, R.; Di Corato, R.; Pellegrino, T.; Kalyva, M.; Sabella, S., Water-repellent cellulose fiber networks with multifunctional properties. *ACS applied materials & interfaces* **2011,** *3* (10), 4024-4031.
17. Dong, S.; Roman, M., Fluorescently labeled cellulose nanocrystals for bioimaging applications. *Journal of the American Chemical Society* **2007,** *129* (45), 13810-13811.
18. Mahmoud, K. A.; Mena, J. A.; Male, K. B.; Hrapovic, S.; Kamen, A.; Luong, J. H., Effect of surface charge on the cellular uptake and cytotoxicity of fluorescent labeled cellulose nanocrystals. *ACS applied materials & interfaces* **2010,** *2* (10), 2924-2932.
19. Taheri, A.; Mohammadi, M., The use of cellulose nanocrystals for potential application in topical delivery of hydroquinone. *Chemical biology & drug design* **2015,** *86* (1), 102-106.
20. Plackett, D.; Letchford, K.; Jackson, J.; Burt, H., A review of nanocellulose as a novel vehicle for drug delivery. *Nordic Pulp & Paper Research Journal* **2014,** *29* (1), 105-118.
21. Akhlaghi, S. P.; Berry, R. C.; Tam, K. C., Surface modification of cellulose nanocrystal with chitosan oligosaccharide for drug delivery applications. *Cellulose* **2013,** *20*, 1747-1764.
22. Habibi, Y.; Lucia, L. A.; Rojas, O. J., Cellulose nanocrystals: chemistry, self-assembly, and applications. *Chemical reviews* **2010,** *110* (6), 3479-3500.
23. Sacui, I. A.; Nieuwendaal, R. C.; Burnett, D. J.; Stranick, S. J.; Jorfi, M.; Weder, C.; Foster, E. J.; Olsson, R. T.; Gilman, J. W., Comparison of the properties of cellulose nanocrystals and cellulose nanofibrils isolated from bacteria, tunicate, and wood processed using

acid, enzymatic, mechanical, and oxidative methods. *ACS applied materials & interfaces* **2014,** *6* (9), 6127-6138.
24. Rånby, B. G., Fibrous macromolecular systems. Cellulose and muscle. The colloidal properties of cellulose micelles. *Discussions of the Faraday Society* **1951,** *11*, 158-164.
25. Domingues, R. M.; Gomes, M. E.; Reis, R. L., The potential of cellulose nanocrystals in tissue engineering strategies. *Biomacromolecules* **2014,** *15* (7), 2327-2346.
26. Pääkkö, M.; Ankerfors, M.; Kosonen, H.; Nykänen, A.; Ahola, S.; Österberg, M.; Ruokolainen, J.; Laine, J.; Larsson, P. T.; Ikkala, O., Enzymatic hydrolysis combined with mechanical shearing and high-pressure homogenization for nanoscale cellulose fibrils and strong gels. *Biomacromolecules* **2007,** *8* (6), 1934-1941.
27. George, J.; Ramana, K.; Bawa, A., Bacterial cellulose nanocrystals exhibiting high thermal stability and their polymer nanocomposites. *International Journal of Biological Macromolecules* **2011,** *48* (1), 50-57.
28. Elazzouzi-Hafraoui, S.; Nishiyama, Y.; Putaux, J.-L.; Heux, L.; Dubreuil, F.; Rochas, C., The shape and size distribution of crystalline nanoparticles prepared by acid hydrolysis of native cellulose. *Biomacromolecules* **2008,** *9* (1), 57-65.
29. Håkansson, H.; Ahlgren, P., Acid hydrolysis of some industrial pulps: effect of hydrolysis conditions and raw material. *Cellulose* **2005,** *12*, 177-183.
30. Dong, X. M.; Revol, J.-F.; Gray, D. G., Effect of microcrystallite preparation conditions on the formation of colloid crystals of cellulose. *Cellulose* **1998,** *5*, 19-32.
31. Araki, J.; Wada, M.; Kuga, S.; Okano, T., Influence of surface charge on viscosity behavior of cellulose microcrystal suspension. *Journal of wood science* **1999,** *45* (3), 258-261.
32. Braun, B.; Dorgan, J. R., Single-step method for the isolation and surface functionalization of cellulosic nanowhiskers. *Biomacromolecules* **2009,** *10* (2), 334-341.
33. Saito, T.; Nishiyama, Y.; Putaux, J.-L.; Vignon, M.; Isogai, A., Homogeneous suspensions of individualized microfibrils from TEMPO-catalyzed oxidation of native cellulose. *Biomacromolecules* **2006,** *7* (6), 1687-1691.
34. Andrews, M. P.; Morse, T., Method for producing functionalized nanocrystalline cellulose and functionalized nanocrystalline cellulose thereby produced. Google Patents: 2021.
35. Tang, S. Y.; Bourne, R. A.; Smith, R. L.; Poliakoff, M., The 24 principles of green engineering and green chemistry:“Improvements Productively”. *Green Chemistry* **2008,** *10* (3), 268-269.
36. Morse, T. Nanocrystalline Cellulose: Surface Chemical Transformation and Applications. McGill University, 2015.
37. Zhou, Y.; Fu, S.; Zheng, L.; Zhan, H., Effect of nanocellulose isolation techniques on the formation of reinforced poly (vinyl alcohol) nanocomposite films. *Express Polymer Letters* **2012,** *6* (10).
38. Lehmkuhler, A.; Miller, M. D.; Bradman, A.; Castorina, R.; Chen, M.-A.; Xie, T.; Mitchell, A. E., Levels of FD&C certified food dyes in foods commonly consumed by children. *Journal of Food Composition and Analysis* **2022,** *112*, 104649.

39. Lankalapalli, S.; Kolapalli, V., Polyelectrolyte complexes: A review of their applicability in drug delivery technology. *Indian journal of pharmaceutical sciences* **2009,** *71* (5), 481.
40. Chakraborty, G.; Bhattarai, A.; De, R., Polyelectrolyte–dye interactions: An overview. *Polymers* **2022,** *14* (3), 598.
41. Meka, V. S.; Sing, M. K.; Pichika, M. R.; Nali, S. R.; Kolapalli, V. R.; Kesharwani, P., A comprehensive review on polyelectrolyte complexes. *Drug discovery today* **2017,** *22* (11), 1697-1706.
42. De, R.; Ray, D.; Das, B., Influence of temperature, added electrolyte, and polymer molecular weight on the counterion-condensation phenomenon in aqueous solution of sodium polystyrenesulfonate: A scaling theory approach. *RSC Advances* **2015,** *5* (68), 54890-54898.
43. Viken, A. L.; Skauge, T.; Svendsen, P. E.; Time, P. A.; Spildo, K., Thermothickening and salinity tolerant hydrophobically modified polyacrylamides for polymer flooding. *Energy & Fuels* **2018,** *32* (10), 10421-10427.
44. Wu, D.; Zhu, L.; Li, Y.; Zhang, X.; Xu, S.; Yang, G.; Delair, T., Chitosan-based colloidal polyelectrolyte complexes for drug delivery: a review. *Carbohydrate polymers* **2020,** *238*, 116126.
45. Oyarce, E.; Butter, B.; Santander, P.; Sánchez, J., Polyelectrolytes applied to remove methylene blue and methyl orange dyes from water via polymer-enhanced ultrafiltration. *Journal of Environmental Chemical Engineering* **2021,** *9* (6), 106297.
46. Fukae, K.; Terashima, T.; Sawamoto, M., Cation-condensed microgel-core star polymers as polycationic nanocapsules for molecular capture and release in water. *Macromolecules* **2012,** *45* (8), 3377-3386.
47. Lubrizol Merquat 100 Polymer. https://www.lubrizol.com/Personal-Care/Products/Product-Finder/Products-Data/Merquat-100-polymer (accessed May 2).
48. Rivas, B. L.; Espinosa, C.; Sánchez, J., Application of the liquid-phase polymer-based retention technique to the sorption of molybdenum (VI) and vanadium (V). *Polymer Bulletin* **2019,** *76*, 539-552.
49. Somasundaran, P., *Encyclopedia of surface and colloid science*. CRC press: 2006; Vol. 5.
50. Gicquel, E.; Bras, J.; Rey, C.; Putaux, J.-L.; Pignon, F.; Jean, B.; Martin, C., Impact of sonication on the rheological and colloidal properties of highly concentrated cellulose nanocrystal suspensions. *Cellulose* **2019,** *26*, 7619-7634.
51. Bafana, A.; Devi, S. S.; Chakrabarti, T., Azo dyes: past, present and the future. *Environmental Reviews* **2011,** *19* (NA), 350-371.
52. Chung, K.-T., Azo dyes and human health: A review. *Journal of Environmental Science and Health, Part C* **2016,** *34* (4), 233-261.
53. Li, Y.; Yang, C.-X.; Qian, H.-L.; Zhao, X.; Yan, X.-P., Carboxyl-functionalized covalent organic frameworks for the adsorption and removal of triphenylmethane dyes. *ACS Applied Nano Materials* **2019,** *2* (11), 7290-7298.

54. Simon, J. E.; Decker, E. A.; Ferruzzi, M. G.; Giusti, M. M.; Mejia, C. D.; Goldschmidt, M.; Talcott, S. T., Establishing standards on colors from natural sources. *Journal of food science* **2017,** *82* (11), 2539-2553.
55. Tumolo, T.; Lanfer-Marquez, U. M., Copper chlorophyllin: A food colorant with bioactive properties? *Food Research International* **2012,** *46* (2), 451-459.

Chapter 2- Making and Characterizing CNC-Based Microbead Pigments

2.1 Introduction

The motivation for our research into the properties of CNC-based pigments comes not just from our interest in their chemical and physical properties, but also a need to validate the materials against a standard that is motivated to engage new color sources that make use of naturally sourced materials and that can be traced to sustainable practices. To this end, the research described in this thesis was funded by the Ministère de l'Économie, de l'Innovation (Quebec MEI), Axelys (a non-profit organization funded by MEI to accelerate the development of new technologies of benefit to Quebec), and Anomera, Inc (a McGill spin-off). In this context, the primary objective of the research was to advance knowledge of the chemical and physical properties of the CNC pigments against the backdrop of a viable industry test framework – the color cosmetics industry.

As introduced in chapter 1, the CNC pigments are based on combining electronegative dye molecules with nanocrystals whose charge has been inverted by forming a polyelectrolyte complex (PEC). In effect, we carry out an unprecedented form of pigment production by replacing conventional metal oxide (alumina) carriers of dye (the origin of the term "Lake pigments") with a single cCNC nanocrystal that hosts individual dye molecules. Moreover, color mixing to make different hues of greens, reds, purples, etc., is achieved not by mixing pigments but by mixing the appropriate combination of colored dye molecules directly on the individual nanocrystals. Very vibrant colors covering an enormous color gamut are obtained this way.

We now provide a brief description of the PEC used to make the CNC-based pigments. A more detailed discussion of the PEC is given in the introductory chapter 1. There are three principal components to the pigment particle, the first being carboxylated cellulose nanocrystals (cCNCs).[1] The second component is poly(diallyldimethylammonium chloride) (PDDA). It is a cationic polyelectrolyte exhibiting a quaternized nitrogen. PDDA is used to reverse the surface charge of the CNC from negative to positive. This then promotes the binding of the last component of the PEC, anionic dyes.

After spray drying, agglomerated cCNC makes up the bulk of the pigment particle. Prior to spray drying we create a PEC platform that binds the dye. The platform comprises cCNC + PDDA. As discussed below, it is important to avoid flocculation prior to dye binding. During the addition of PDDA to an aqueous suspension of cCNC, the reaction mixture becomes cloudy,

indicating particle agglomeration. Sonication disperses the larger agglomerates yielding a translucent fluid with a blue hue due to Tyndall scattering. (The blue hue is due to the inverse 4th power scattering of wavelengths of light favouring blue over other wavelengths in the 400-700 nm range. The effect is most pronounced when the scattering particles are smaller than the wavelength of visible light and are suspended in a transparent medium.) A picture of the cCNC and PDDA suspension is shown below. Throughout this chapter, the positively charged product will be referred to as cCNC^{+}.

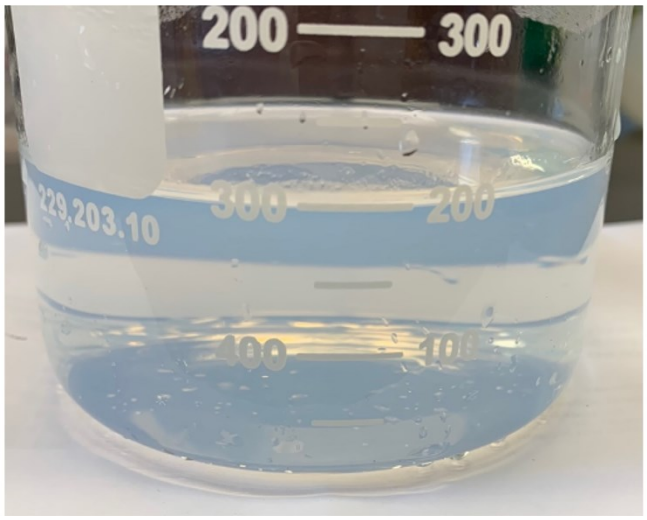

Figure 2.1: cCNC and PDDA suspension in the form of the cationic complex cCNC^{+}

Having created the cCNC^{+} suspension, the product is purified by removing excess salt through the process of diafiltration. The high concentration of chloride ion from PDDA, screens the charge on the cationic particles. Charge screening promotes association, causing the viscosity of the suspension to increase through particle-particle aggregation. Obviously, excess chloride would compete with anionic dye binding. With diafiltration (Figure 2.2 and also 2.6) the chloride ions are removed. Chloride removal reduces charge screening, raising the interparticle repulsive potential, thereby decreasing the viscosity as a result of increased dispersion of the cCNC-PDDA complex. Diafiltration functions using tangential flow filtration. The particle feed is pumped parallel to the filtration membrane face. Due to the pressure from the peristaltic pump, a portion of the feed passes through the membrane to yield the filtrate (permeate). The remaining feed (retentate) is recirculated to the feed reservoir.[2] The permeate is purified until the conductivity of the sample is decreased to less than 30 μS/cm, indicating a decrease in salt concentration.

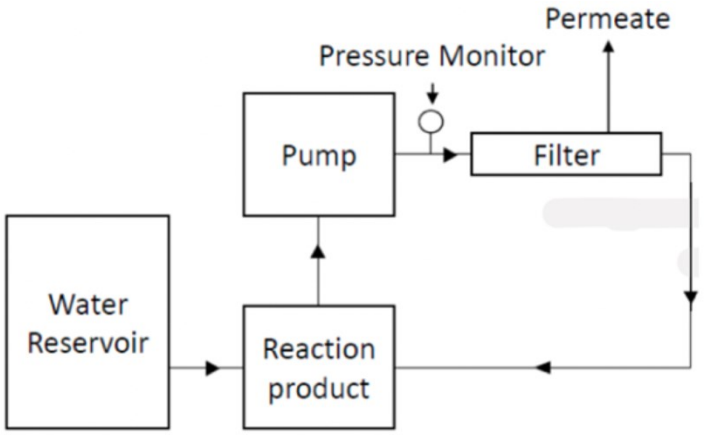

Figure 2.2: Schematic of the diafiltration setup. Arrows show the direction of flow.[1]

After filtration of cCNC^{+}, the anionic dye is added to obtain the final, colored PEC. This "metachromatic" complex is then ready to be spray dried. It is important here to note that our process "conserves entropy". Instead of putting energy into dissolving the hydrogen-bonded lattice of cCNC to solubilize cellulose polymers, we use the nanocrystal directly. We then rescale the nanoscale particles into macroscale pigment particles by spray drying to yield spherical, intensely colored pigment microbeads that are smaller than 7 μm. A schematic of a spray dryer is shown below in Figure 2.3. The spray dryer functions by delivering the feedstock fluid to an atomizer inside a spray-drying chamber concurrently with a hot drying gas. The material is delivered to an atomizer via a peristaltic pump and atomized using a pressure nozzle. When the hot drying gas combines with the feedstock fluid in the nozzle, the fluid atomizes into micron-sized droplets that host the spherical assembly of the pigment nanoparticles, rapidly forming a microbead as the solvent evaporates. The microbead continues to evaporate water in the stream of the drying gas as it exits the drying chamber and enters the cyclone. In the cyclone, the microbeads are separated into either a product collection container or are trapped as waste. For our studies, the spray dryer was operated using a single-pass mode, meaning that the drying gas passed through the system once and was immediately vented into the waste stream.[3]

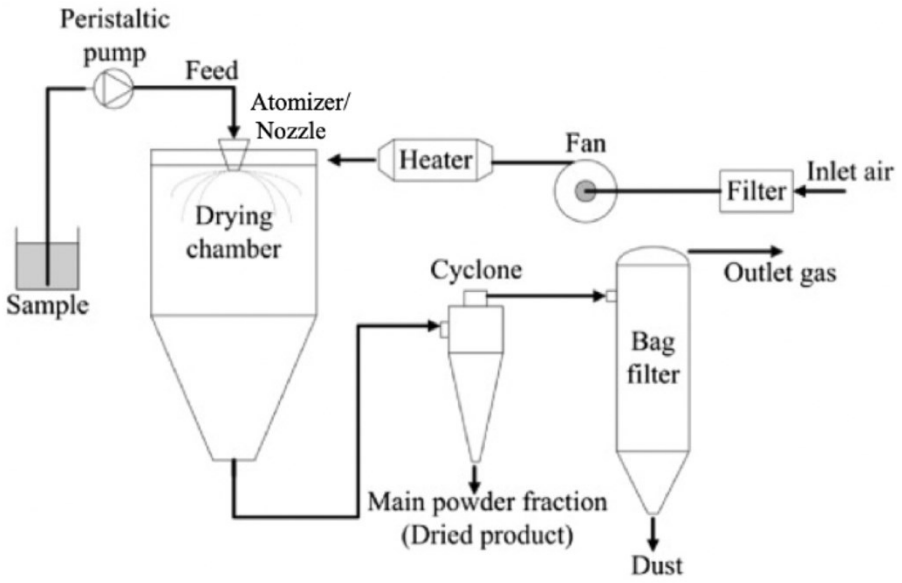

Figure 2.3: Schematic of the spray drying process [4]

Microdroplet drying can be broken down into several key events that take place within micro- to milli-seconds (Figure 2.4 A). First, the atomizer converts the feed solution into microdroplets. The droplets contact the hot drying gas, and the evaporation process begins. Due to the high temperature, solvent evaporation occurs rapidly. The evaporation is quickest at the surface of the droplet that experiences an increasing concentration of the precipitating PEC. A skin forms at the microdroplet surface. Because the viscous skin prevents diffusion, further solvent evaporation is impeded. In certain circumstances, the center of the droplet solidifies and both the skin layer and core become coextensive yielding a spherical particle.[3] The particle size of spray-dried CNC has a complex nonlinear relationship with the different operating variables. Droplet formation is controlled by the liquid breakup process that involves the aerodynamic disruptive forces of the gas flow rate and the consolidation forces of the viscosity and surface tension of the feed solution. This means that the gas flow rate, and the liquid feed rate can have a large impact on particle size due to their correlation with droplet size. The morphology of the spray-dried particles can be altered by adjusting several parameters. The two main parameters are the outlet temperature and feed concentration.[5] In our studies, the spray-dried CNC microparticles exhibited two main morphologies, either spherical or deformed mushroom cap (or donut)-shape. The differing morphologies are caused in part by the chaotic interaction of the airflow and solution droplets.[6] Binding of PDDA to make cCNC$^+$ increases the sphericity, and the binding of anionic dyes to the PEC yields the most spherical particles. This trend reflects the

way that the phenomenological Peclet number determines particle morphology.[7] In particular, particle size depends strongly on atomizing air flow and solids concentration in the feed liquid and in the forming droplet. A spherical particle is the desired morphology for the spray-dried pigment microbead. In part, this is because the spherical pigment particles are much sought-after in cosmetics because of their extraordinarily soft feel. SEM images of the microparticles after spray-drying 3 different feedstocks are shown below in Figure 2.4 B. We discuss the particle size distributions later.

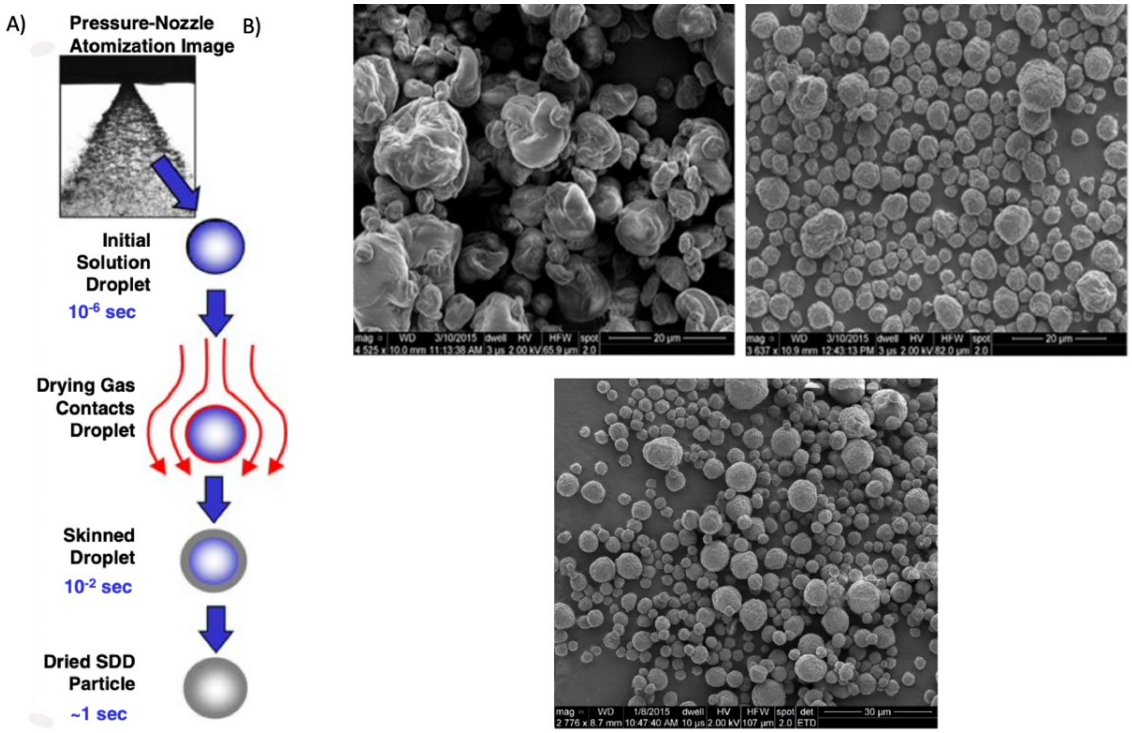

Figure 2.4: A) Schematic for the formation of a dried spray-dried dispersion (SDD) particle. [3] *B) SEM images of spray-dried cCNC (top left), cCNC*$^{+}$*(top right), and CNC pigment (bottom).*[1]

A widely used pigment industry color model is the CIE (Commission Internationale de l'Eclairage) L* a* b* color system. The model is commonly referred to as CIELAB, which is based on the so-called opponent color theory of vision. CIELAB is one of many models that admit numerical quantification of colors using a three-axis system like that shown in Figure 2.5. The L* value indicates lightness. Its value ranges from 0 (black) to 100 (white) and is assigned to the vertical axis. The a* value represents the red-green component of a color. Its value is positive for red and negative for green. The b* component represents the yellow and blue values of a

color. Its values are positive for yellow and negative for blue.[8, 9] The three components make up the axes of a sphere for visually representing colors shown in Figure 2.5.

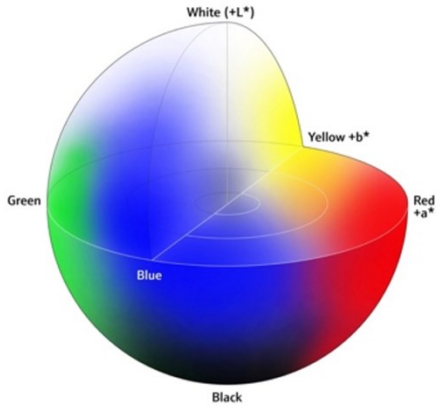

Figure 2.5: CIE L a* b* color sphere* [10]

In our studies, we are interested in the L*a*b values of the CNC-based pigments. These values allow us to assess the run-to-run reproducibility of different pigments. Moreover, quantification in CIELAB terms allows us to compare the new pigments against "lake pigments" that are widely used in cosmetics industries. This is especially important when formulating the nanocellulose based pigments in oils, emulsions, and other ingredients for comparison against competitive pigments. As described below, L*a*b values are determined by measuring reflectance spectra. To compare two colors, or to chart the time series change in a color with respect to a control, the difference between the L*a*b components of two samples is determined. The differences are represented as ΔL*, Δa*, and Δb*. These three values can then be combined as in equation 2.1 to obtain ΔE* (read, "delta-E"). Delta-E can then be used as a single value to compare two colors.

$$\Delta E^* = \sqrt{(\Delta L^*)^2 + (\Delta a^*)^2 + (\Delta b^*)^2} \qquad (2.1)$$

Values of the total color difference delta-E in the range below 3.0 in CIELAB units indicate differences in the color between two pigments that are imperceptible to the human eye. [11] Values in the range 3.0–6.0 suggest very clear differences in color, and values exceeding 6.0 indicate strong differences. Time series analysis is particularly useful in the study of pigment stability as functions of host fluid medium and temperature. We give a detailed example of a time series analysis in the results and discussion section below.[1]

Saturation and coverage are important parameters to determine and interpret when contrasting the properties of the CNC-based pigments with the corresponding Lakes. Saturation (S*), also known as chroma (C^*_{ab}), indicates how clear, bright, or brilliant a color appears to the eye. A color with high saturation will be further from the L* axis. Saturation can be calculated using Δa* and Δb* (equation 2.2). Saturation is sometimes denoted ΔE^*_{ab}.[12, 13]

$$S^* = \sqrt{(\Delta a^*)^2 + (\Delta b^*)^2} \qquad (2.2)$$

Coverage is determined by a simple technique used to indicate how much light passes through a layer of pigment. Accordingly, L* values are first obtained for a sample supported on a black background and then on a white background. The difference between the two L* values is the coverage of the sample. Strong coverage is desired as it means that less pigment must be used to achieve the hiding effect.

2.2 Experimental

2.2.1 Materials

Samples of cCNC (trade name DextraCel™) were obtained from Anomera, Inc. as a 3.75 wt% water suspension. For sonication, a 6 mm Sonics Industries microtip was used in combination with a Sonics vibra-cell VCX 130 probe sonicator. High molecular weight (400,000-500,000 M_w) PDDA (poly(diallyldimethylammonium chloride)), 20 % in water was obtained from Sigma Aldrich and used as received. Figure 2.6 shows a photograph of the diafiltration unit. This employed a Repligen Minikros Sampler 20 cm, 10 kDa diafiltration tube in combination with MasterFlex L/S® 36 High-Performance Precision Pump Tubing. A MasterFlex L/S economy drive peristaltic pump with a MasterFlex L/S easy-load II pump head provided flow control.

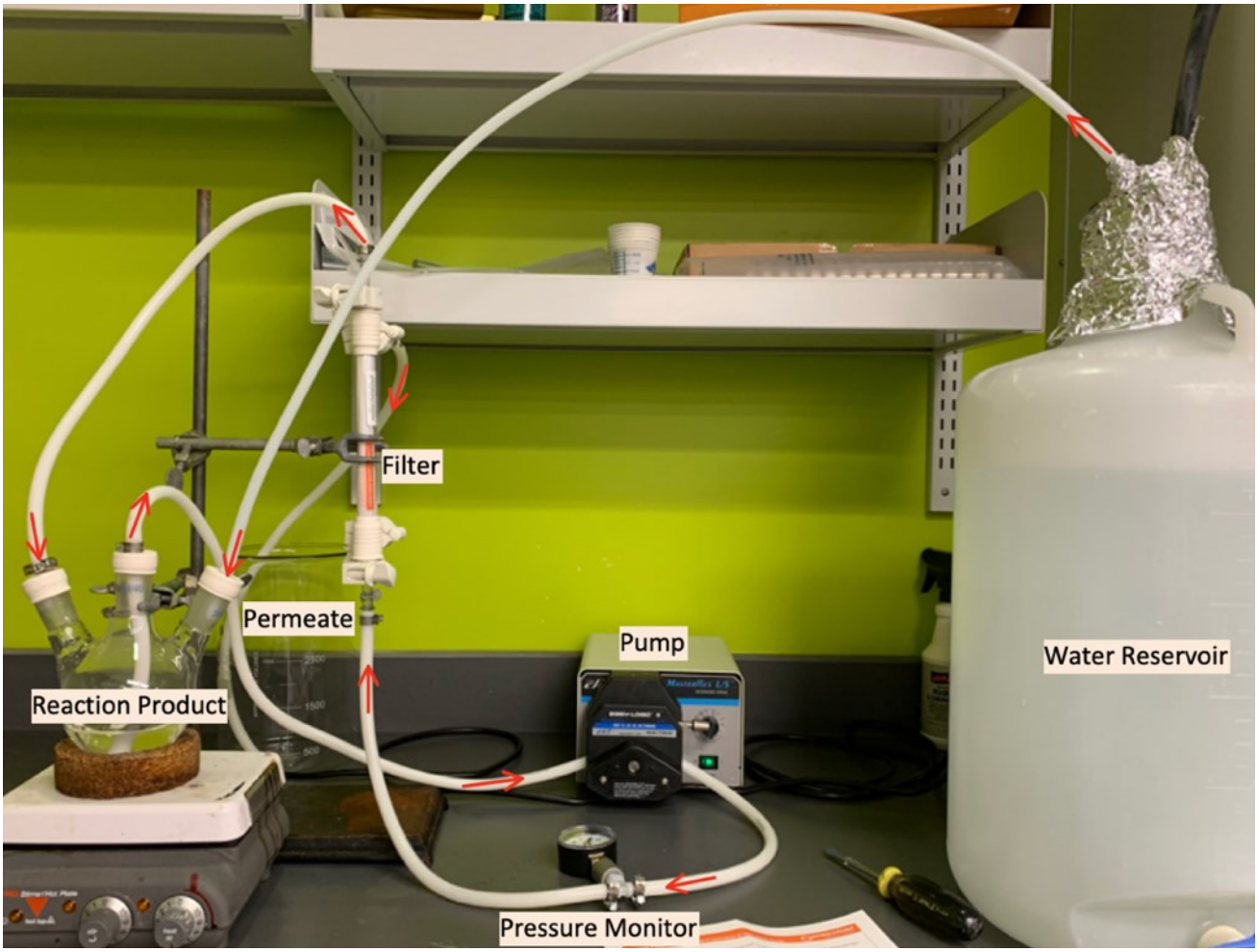

Figure 2.6: Diafiltration set-up. Red arrows indicate the direction of the flow.

Spray-drying was carried out with a Büchi Mini Spray Dryer B-191 (Büchi Corporation, New Castle, USA) with inlet and outlet temperatures of 175 °C and 104 °C, respectively, 30% pump speed and 70% aspirator (see below for individual microbead types). The various components of the spray dryer are identified in Figure 2.8.

Figure 2.7: Buchi Mini Spray Dryer B-191 after spray drying red CNC pigment.

The following dyes were used in our studies. These are identified in Figure 2.9 below along with their respective chemical structures.

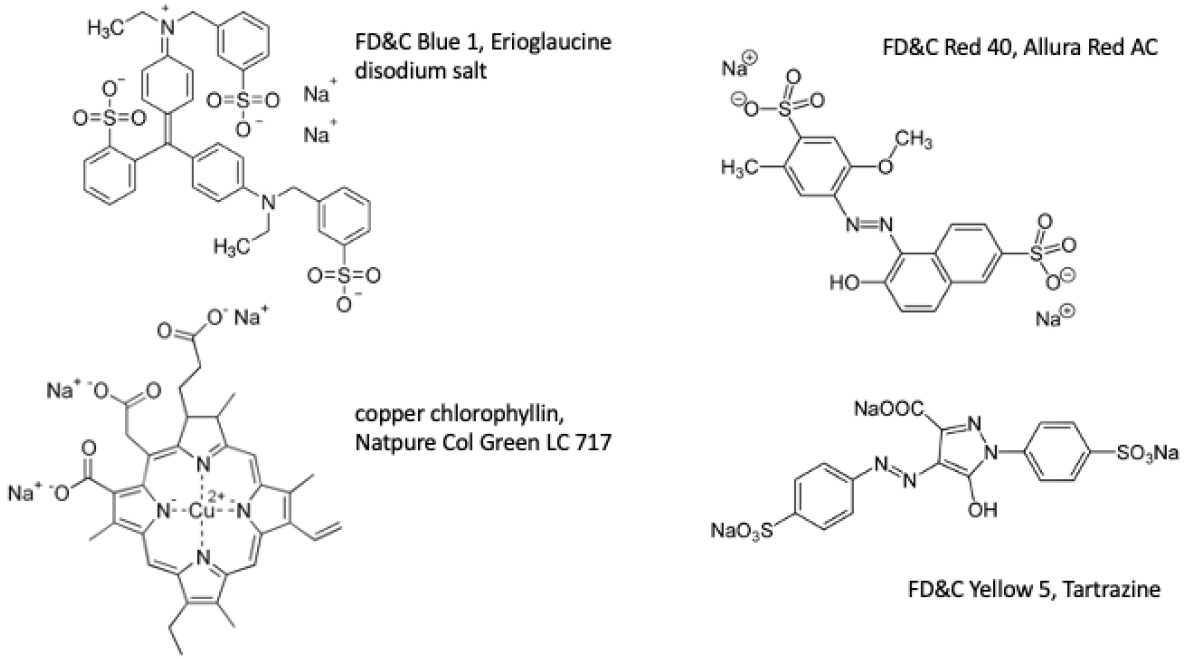

Figure 2.8: Chemical structures of dyes used to make cCNC microbead pigments.

Sources of the anionic dyes: FD&C Blue 1, Erioglaucine disodium salt (861146, Sigma-Aldrich). FD&C Yellow 5, Tartrazine (≥ 85%, Sigma-Aldrich). FD&C Red 40, Allura Red AC (≥ 80%, Sigma-Aldrich). The naturally sourced green pigment was made by binding copper chlorophyllin, Natpure Col Green LC 717 to the $cCNC^{+}$. Orange pigments were prepared by "molecular mixing" of well-defined ratios of Red 40 and Yellow 5. A green pigment was obtained by molecular mixing 1:1 Yellow 5 and Blue 1. A purple pigment was obtained by co-locating Blue 1 and Red 40 in a 1:1 ratio on the nanocrystals. The corresponding Blue 1, Yellow 5 and Red 40 Lakes were obtained from Sensient Technologies.

2.2.2 cCNC Pigment Preparation

$cCNC^{+}$ Preparation

A 200 mL suspension of cCNC in water (0.5% w/v, 1 g) was prepared in a 600 mL beaker by dispersion with sonication and a stir bar. A 4 mL solution of PDDA in water (3.5% w/v, 0.14 g) was added all at once to the cCNC solution. Immediately before adding the PDDA, slow stirring and pulse sonication at 70% output (10 s on, 5 s off) were activated. Stirring and

sonication continued for 37.5 minutes total (time including when the sonicator was off) to yield a stable viscous suspension. The sample was purified by diafiltration until the conductivity of the water permeate was 30 μS/cm, yielding a stable translucent suspension of positively charged $cCNC^+$.

Dye-loaded $cCNC^+$ preparation

Before adding dye, a 200 mL suspension of $cCNC^+$ was poured (0.5 wt%, 1g $cCNC^+$) into a 600 mL beaker. The suspension was rapidly mixed with a Rayneri mixer equipped with a three-blade propeller. A 20 mL solution of dye dissolved in water (0.5 % w/v, 0.1 g) was slowly added to the above suspension while stirring with the mixer at 700 rpm. Once the dye was added, stirring was continued for an additional 20 minutes. The 220 mL sample was then spray dried using the Buchi (model B191) tool with a 175 °C inlet temperature, 30% pump speed, and 70% aspirator.

2.2.3 Preparation of Pristine cCNC and $cCNC^+$ Microbeads

Pristine (no dye) microbead powder samples of cCNC and $cCNC^+$ were made by spray drying. The pristine cCNC was spray dried from a 0.5 wt%, 200 mL suspension of cCNC. The $cCNC^+$ was made by spray drying the 200 mL suspension of $cCNC^+$ obtained after the diafiltration step as described above. The spray drying parameters were: 175 °C inlet temperature, 30% pump speed, and 70% aspirator.

2.2.4 Formulation of Time Series Stability Samples

The aim of this study was to evaluate the color stability of cCNC microbead pigments equipped with Red 40 dye and subsequently heated in a temperature-regulated incubator oven (Fisher 6500 incubator) at 45 °C for 1, 2, and 5 weeks. In this study, stability refers to the resistance of pigment particles to the leaching of dye from pigment into a host fluid medium and/or resistance to fragmentation to yield nanoparticles or larger fragments in the fluid medium. Lake pigments (Sensient Technologies) were used for comparison. The study is relevant to framing the stability range of the new cCNC-based pigments when used in conventional cosmetic fluid formulations and subject to aging at a well-defined temperature. The study was intended to provide a quantitative contrast with the performance of the commercial Lake pigments.

In separate 7-dram vials, 5 mg of R40 dye was added to 1 g of four different oils (one of each): Pentaerythrityl Tetraisostearate (e.g. Crodamol PTIS), ethyldodecanol (Euthanol G), polybutene (Polybutene 10), diisostearyl malate (Salacos 222) and water. The structures of the oils except for polybutene are shown in Figure 2.9 below. The resulting dispersions were manually stirred for a few minutes (2-3 min) until they became homogeneous. They were then kept in the oven at 45°C for 1, 2, and 5 weeks. After each time point, the samples were removed from the oven and manually stirred again for 3-4 min to homogeneity. An aliquot of dispersion was then deposited on a microscope slide to determine its color parameters (L, a, and b) from its reflectance spectrum (Konica Minolta). Particle size analysis was completed using digital microscopy (Keyence VHX-6000).

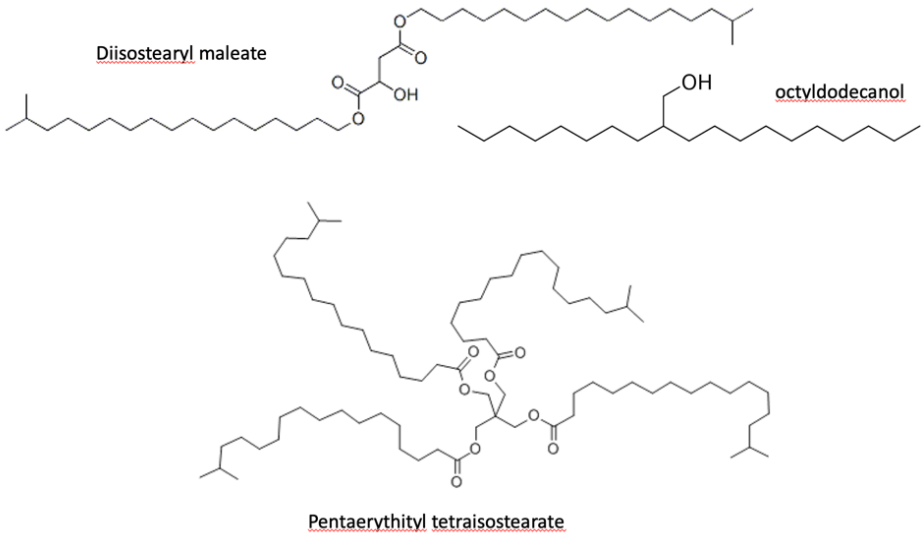

Figure 2.9: Chemical structures of oils used in the time series study.

2.2.5 Optical Characterization

Reflectance spectra were obtained for all CNC pigment types. The corresponding lake pigments were also analyzed. Spectra were obtained with a Konica Minolta Sensing spectrophotometer CM-700d and analyzed using the Spectra Magic NX Colour Data Software CM-S100w. To obtain reflectance (hence L*a*b values) a small amount of pigment powder (~30 mg) was added to a 1-dram vial to provide a uniform layer across the bottom of the vial. The vial was then placed on top of the specimen measuring port of the spectrophotometer and the L*a*b values were obtained. Otherwise, reflectance spectra of fluid samples for the time series analysis were acquired as described in the preceding section. Note that the CM700d is really a compact

integrating sphere that has been optimized to reject specular reflection and gather scattered light at an 8^0 angle. Emphasizing only the L*a*b values misses valuable information contained in the full reflectance spectrum. We address the importance of gathering the spectral reflectance data in our section on the time series analysis of a cCNC-based Red 40 pigment.

Coverage and Saturation

Coverage and saturation values were obtained only for the red 40 CNC pigment and a red 40 lake as reference. The pigment was dispersed with 1g of diisostearyl malate in a 7-dram vial, and 4 different concentrations were prepared: 1, 2, 3, 4 wt%. The sample was then mixed for 15 seconds using a vortex mixer to ensure uniform dispersion. The fluid dispersion was sampled with a Pasteur pipette. Droplets were deposited on a microscope slide, and a glass cover slip was then placed over the sample. The a^* and b^* values were obtained with the Konica Minolta unit. To obtain coverage, the sample L^* value was determined with a white sheet behind the microscope slide. Then the sample L^* value was obtained with a black sheet behind the microscope slide. The difference between the black background L^* and the white background L^* was reported as the coverage value for the sample.

2.2.6 Scanning Electron Microscopy

The scanning electron microscopy (SEM) samples were prepared by first coating them with 2- 4 nm of gold-palladium. The SEM images were then obtained using an FEI Quanta 450 Environmental Scanning Electron Microscope (FE-ESEM with EDAX Octane Super 60 mm2 SDD and TEAM EDS Analysis). The SEM images were analyzed using a custom ImageJ[14] macro to measure the length and width of individual particles. With these values, the median particle diameter (D50) value was obtained. Some images were also obtained using high-resolution scanning electron microscopy (HR-SEM). The HR-SEM images were obtained using an FEI Tecnai 12 BioTwin at 120 kV using an AMT XR80C CCD Camera System.

2.3 Results and Discussion

2.3.1 CNC Pigment powders

Blue, yellow, and red CNC-based microbead pigments were first made with Blue 1, Yellow 5, and Red 40 anionic dyes. Hues of orange, green and purple were prepared by competitive binding of 2 types of dye to the $cCNC^+$ PEC complex. Green resulted by combining

a 1:1 solution of Blue 1 and Yellow 5 dyes with $cCNC^{+}$. Purple resulted from the 1:1 combination of Blue 1 and Red 40. Orange hues were prepared either from a 1:1 or 2:1 combination of Red 40 and Yellow 5. Lastly, a green pigment was made using copper chlorophyllin. Some of the dye pigments produced are shown in Figure 2.10. Their yields after spray drying are collected below in Table 2.1.

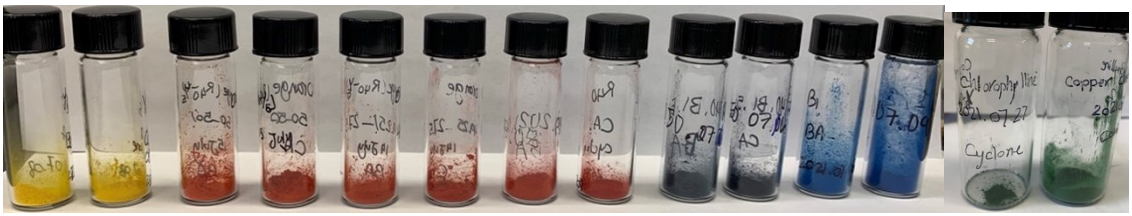

Figure 2.10: Initial CNC pigments produced, (left to right) yellow 5, orange 2:1, orange 1:1, red 40, 'purple' 1:1, blue 1, natural green.

Table 2.1: CNC pigment yields

Pigment	**Percent Yield (%)**
Blue 1 - 1	32.9
Red 40 - 1	37.0
Blue 1 - 2	46.5
Yellow 5	37.6
Orange 2:1	42.0
Orange 1:1	43.4
Purple	34.8
Green	51.6
Natural green	38.8
Red 40 - 2	41.8

The range of yields obtained for the CNC pigments, 32 – 52 %, reflects the sensitive dependence of the spray drying process on the starting feed concentration for fixed spray drying conditions of inlet/outlet temperature, pressure, and feed rate. Accordingly, the yields are not to be construed as being low, but instead as the result of the challenges in controlling the spray drying parameters, including the subtle and complex mixing dynamics in the nozzle head. A greater focus was placed on the properties of the individual pigments obtained.

2.3.2 Optical Characterization of CNC Pigments

The reflectance values of the individual dye CNC pigments and equivalent lake pigments are shown in Table 2.2 below. The ΔE* values were obtained for each of the respective dyes by comparing the values of the CNC and lake pigments.

Table 2.2: Reflectance values (L, a*, b*,* ΔE*) for CNC microbead and lake pigments.

Pigment	**L***	**a***	**b***	**ΔE***
CNC Red 40	57.38	29.71	13.61	6.95
Lake Red 40	54.63	23.52	12.07	
CNC Blue 1	55.99	-8.31	-17.62	3.86
Lake Blue 1	53.73	-5.33	-18.59	
CNC Yellow 5	80.18	12.62	51.8	8.08
Lake Yellow 5	78.25	20.34	50.48	

The cCNC red pigments have a high positive value for a*, which indicates an enhanced red component to its color. Why should this be the case when both pigments are made with the same dye? Comparing the Red 40 CNC with the Red 40 lake, we direct attention to the ΔE* value of 6.95. The two types of pigment are perceptibly different to the human eye, with the cCNC-based pigment appearing more vibrant. Most of the difference can be attributed to the higher a* value for the cCNC Red 40. We point out that the delta-E between the commercial Red 40 Lake and the nanocellulose-based pigment is not a sign of failure of the cCNC-based pigment to match the color characteristics of the commercial lake pigment. This was not the intention of the comparison. In fact, while absolute L*, a*, b* values are necessary components in color difference calculations, they are not necessarily a part of formulating color match predictions. Color matching software utilizes variations of the Kubelka-Munk equation to determine the actual reflectance data of a color target. We did not invoke this kind of analysis because color matching was not our objective. In our case, the delta-E for the Red 40 pigments points to a difference in the underlying optical physics. Without going into detail, scattering from the cCNC-based pigments includes the refractive index (n) difference between supporting nanocrystals, the PDDA and that of the dye, whose latter index is a complex number (n+ik) in

the visible domain due to its dispersive (n) and absorptive (ik) components. The real (dispersive) part of the refractive index of the (chiral) cCNC pigment carrier is approximately n = 1.5. That of the Lake hydrous alumina is on the order of 1.6. In terms of optical properties, this is a rather large difference between the carrier substrates. The Konica-Minolta measures diffuse reflectance, but the scattering properties of the two classes of pigments differ. The cCNC microbeads are rather uniform in size and appear spherical (spherical scatterers). The Lake pigment comprises particles of nonuniform size ranging in scale from micrometers to nanometers. Not surprisingly, for similar dye loadings and access to the dye component (more on this in Chapter 4), the optical response over the CIELAB range is the same.

The blue pigments exhibit a negative b*, indicating blue hue in the vector space of CIE. Comparing the blue 1 CNC and Lake, the reflectance values are very similar, with a ΔE* value of 3.86, which is not detectable by the eye. Lastly, the yellow pigments have an expectedly very high b* value. There is a small difference in ΔE*, 8.08, between the lake and CNC pigment. Most of this difference is from the CNC yellow having a significantly lower a* value indicating that the color appears less red than the yellow lake pigment. We next examine the CIELAB output from the reflectance from the pigments prepared by competitive molecular mixing of two different dye molecules on the cellulose nanocrystals. The findings are collected in Table 2.3.

Table 2.3: Reflectance values (L, a*, b*,)* for mixed dye CNC pigments.

Pigment	**L***	**a***	**b***
CNC Red 40: Yellow 5 (2:1)	59.44	30.88	17.55
CNC Red 40: Yellow 5 (1:1)	61.46	31.55	20.75
CNC Blue 1: Yellow 5 (1:1)	56.07	-15.21	9.04
CNC Red 40: Blue 1 (1:1)	51.67	0.87	-2.61

The Red 40 combined with the Yellow 5 dye yields two hues of orange whose optical properties depend on the ratio of the dyes used to make the pigments. Both hues appear more red-orange (i.e. “cooler”) than yellow-orange, and this is reflected in both having a high a* value, even higher than the value for the mono-dyed Red 40 cCNC pigment. The b* value is also significantly reduced when compared to the mono-dyed Yellow 5 pigment. The reflectance

values for the two orange hues are similar. A difference is that the 2:1 Red 40: Yellow 5 sample exhibits a smaller b*. Surprisingly the a* marginally decreases when the red 40 ratio increases. Co-binding of Blue 1 and Yellow 5 dyes yields a green CNC pigment. The green shows the expected negative a* value and a correspondingly strong green hue. The 1:1 combination of Red 40 and Blue 1 dyes was intended to make purple. Visually, the resulting pigment was a very dark, almost blue-black, as seen in Figure 2.10. The reflectance values show a low saturation with a* and b* values close to 0.

Saturation and Coverage

For saturation and coverage, we restricted our attention to Red 40 pigments, which are of great interest to the cosmetics industry. The findings are collected in Table 2.4.

Table 2.4: Red 40 pigments saturation values with varying concentrations in diisostearyl malate

CNC Red 40 Sample (w/v)	**Saturation**		**Lake Red 40 Sample**
1 %	21.80	22.09	1 %
2 %	19.81	22.07	2 %
3 %	23.58	23.50	3 %
4 %	23.04	26.51	4 %

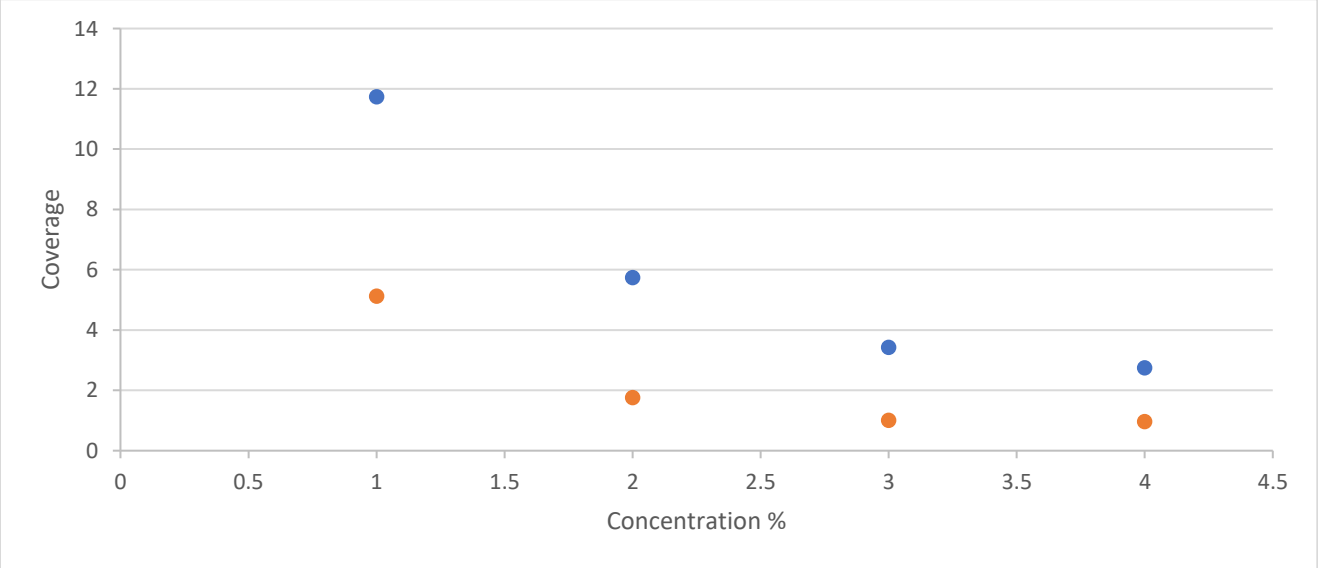

Figure 2.11: Coverage of red 40 pigments with varying concentrations in diisostearyl malate. Orange dots – Red 40 Lake pigment; blue dots – CNC Red 40 pigment.

The saturation values for the CNC Red 40 pigment are close to those of the Lake Red 40 pigment sample at 1 % concentration, with both around 22. Saturation associated with increasing concentration of Red 40 CNC shows little change, a finding we cannot explain. Saturation for the Red 40 lake pigment increases with pigment concentration as expected. Nevertheless, both types of pigment show similar saturation. If the data are meaningful, the findings for the cCNC-based Red 40 suggest that less pigment can be used to make a saturated color via the cellulose nanocrystal route. At a 1% pigment concentration, the coverage was significantly better for the lake pigment (lower numbers mean better coverage). With increasing the concentration, the difference in coverage between the lake and CNC pigment becomes smaller. Overall, the differences between the cCNC-based Red 40 pigment and the Red 40 Lake lie in part in differences in dye content/loading. The CNC pigment contains 10 wt. % dye compared with 40 % for the commercial Lake. Having four times the amount of dye enables the lake to have greater coverage and saturation. To adjust for the difference in dye loading between the 2 pigment types, a sample of CNC pigment with increased dye loading was made. The findings are described in chapter 3. Saturation and coverage also depend on particle size. Smaller spherical cellulose microbead particles offer more surface area for matter-photon interactions. As implied earlier, the difference in refractive index between the pigment particle and the host medium also contributes to coverage. The larger the difference, the greater the coverage for a given particle size and shape. This suggests that for a given refractive index difference, not only dye loading but also particle size need to be adjusted to improve saturation and coverage. We examine cellulose microbead pigment particle surface morphology in the next section.

2.3.3 Microbead Morphology

Previous research has found that spray-dried cCNC resulted in distorted microparticles with poor sphericity. The addition of PDDA to make $cCNC^+$ powders induces a shape morphology transition to a more spherical object. “Pristine” cCNC microbeads were derived from 4 %w/v CNC suspension, whereas $cCNC^+$ powders were prepared from 0.5% w/v aqueous CNC. The higher feed viscosity of the more concentrated aqueous CNC suspension used to make the “pristine” powder is known to be associated with deformations of the spray droplets.[1] By matching the concentrations used to prepare pristine and CNC^+ at 0.5% w/v, we observe that the

pristine microbeads become more spherical, now resembling the spherical morphology of the CNC^+. This is evident from the SEM images of the cCNC and $cCNC^+$ microbeads in Figure 2.12.

cCNC	$cCNC^+$
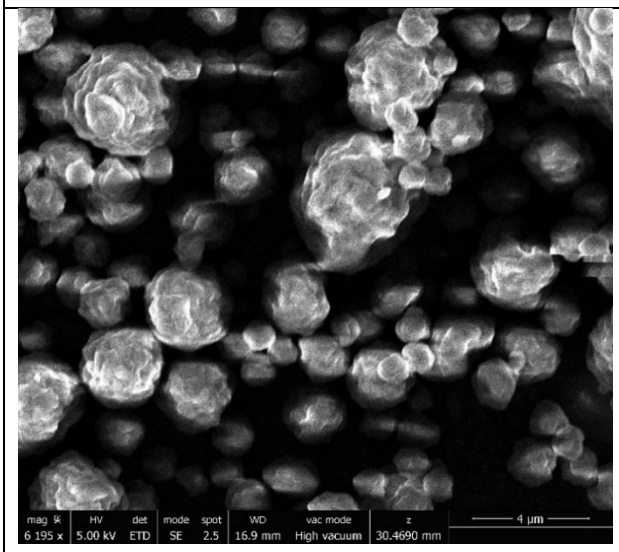	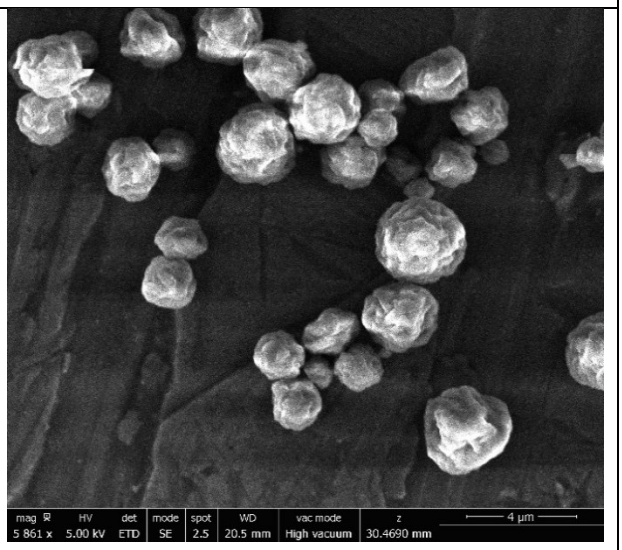

Figure 2.12: SEM image of pristine cCNC microbeads (left) and cCNC+ microbeads (right) when prepared from feed suspensions of 0.5% w/v solids.

We then used very high-resolution SEM (see experimental section) to take a closer look at the surface of pristine CNC and CNC^+ microbeads. The images are displayed in Figure 2.13 below. The images were selected from a large dataset of microbeads and should therefore represent the average morphology of the 2 categories of microbeads. Both types of microbeads are roughly spherical and show highly textured surfaces. Note that the samples were metallized with ~ 2- 4 nm of Au-Pd prior to imaging. We turn first to the pristine cCNC microbead of images A and C. The object is about 4µm in diameter. Its surface appears to consist of patches that likely comprise agglomerates of nanocrystals, perhaps smoothed in appearance by the AuPd metallization layer. Image c) is a closeup of the surface. We know that the nanocrystals are about 250 × 10 nm in dimension. The patchwork appears to consist of twisted agglomerates of nanocrystals that resemble thick twisted ropes. These agglomerates are about 500 nm long and 150 nm in thickness. Given enough time and the correct concentration, the nanocrystals would undergo an isotropic to chiral nematic phase transition. We see no evidence of such order at the surface of the pristine cCNC microbeads. This is not surprising, since the microbeads are formed

rapidly under kinetic trapping conditions. The $cCNC^+$ microbead is also about 4 μm in diameter. Addition of PDDA to make $cCNC^+$ in the feed results in a different surface texture, one that is characterized by broad islands of matter that reveal none of the ultrastructural features exhibited by the pristine cCNC microbeads. This is evident in the island-like texture of Figure 2.13 d).

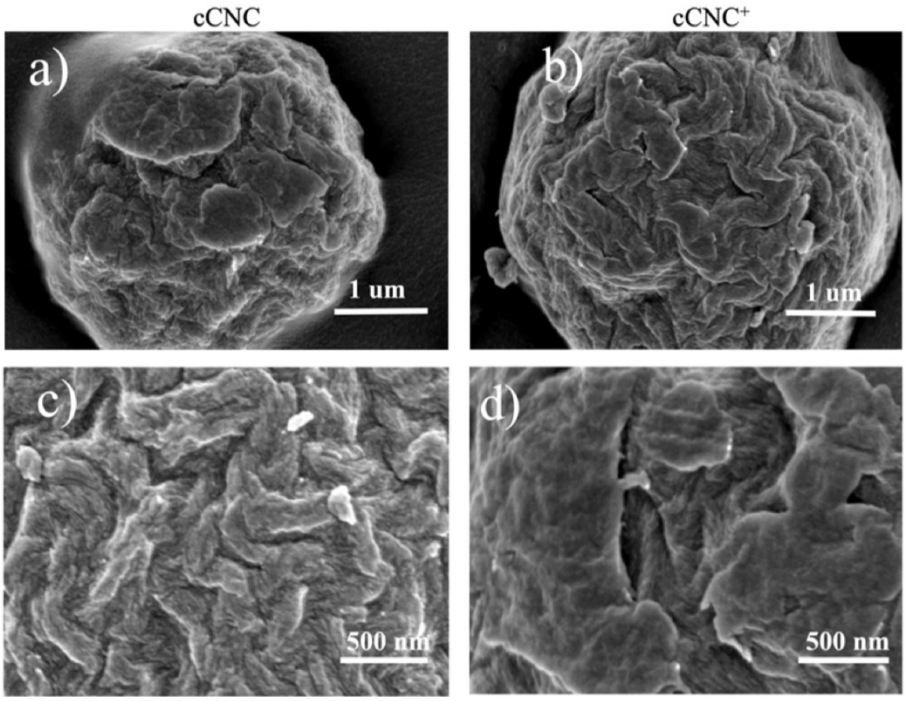

Figure 2.13: HR-SEM images of both a pristine cCNC microbead (a & c), and a $cCNC^+$ microbead (b & d)

It is well known that the addition of small molecules and polymers, changes in solvent and other variables like pressure and temperature, can alter the morphology and surface texture of particles produced by spray drying. The above examples contrasting pristine cCNC with $cCNC^+$ would seem to be cases in point. Our findings are further exemplified when exploring the pigmented microbeads by SEM. These findings are discussed next.

SEM images were obtained for all the pigment microbeads discussed in this thesis. An important objective in our study was to adjust the spray drying parameters so that spherical microbead particles would be obtained and that their diameter would fall in the range < 4 μm. This size regime would yield pigment particles with improved coverage, whilst retaining a desirable feel. In this case, "feel" refers to the sensation of smoothness caused by the "ball-bearing effect" as the microbeads roll on the skin. As evident from Figure 2.14, the first objective was met. All the pigments possess the desired spherical shape. Some of the images are

blurred due to the charging of the microparticle surfaces. The results obtained from the SEM were then used to calculate the mean size distribution of the respective pigments.

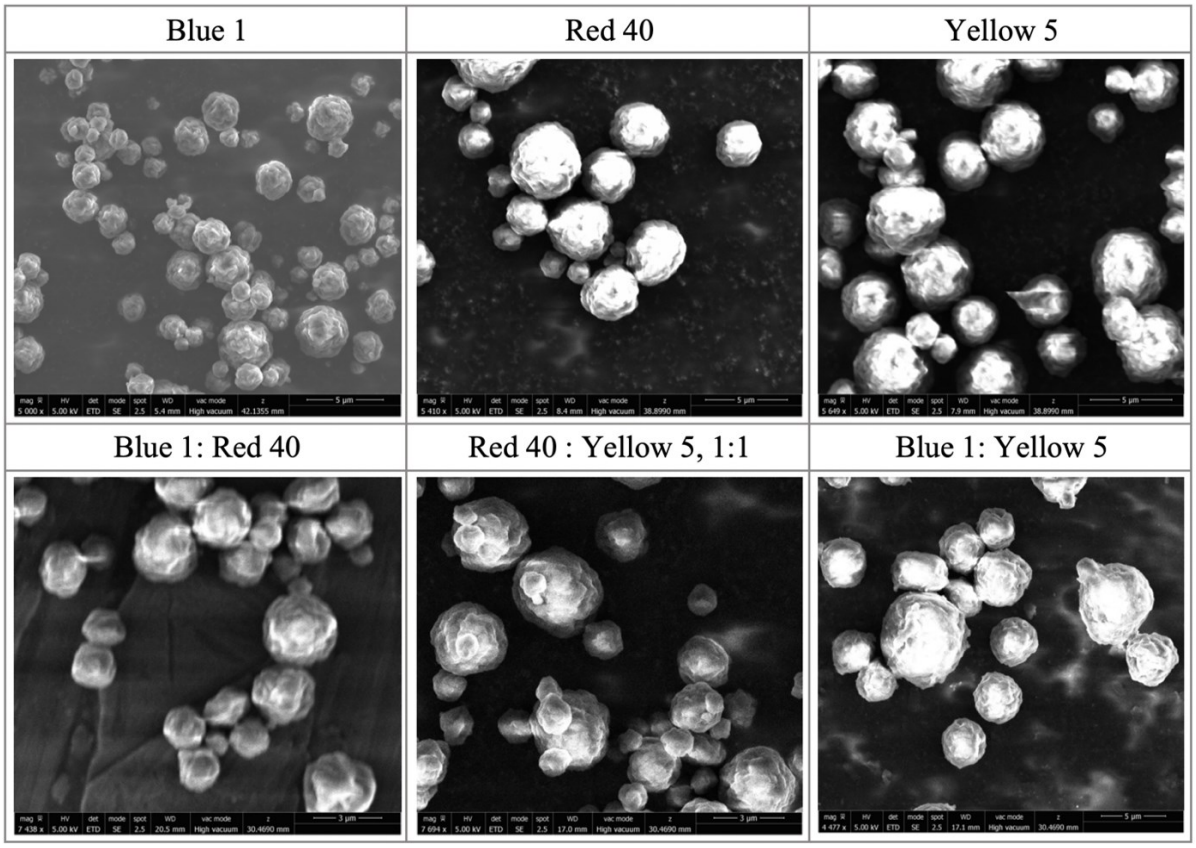

Figure 2.14: SEM images of CNC pigments

2.3.4 Microbead size distributions

We determined the median size distribution (D50) for each pigment type. As seen in Table 2.5, all the produced pigments are below the target < 4 μm diameter D_{50} range.

Table 2.5: CNC pigments median size distribution

Pigment	***D50 (***μm)
CNC Red 40 - 1	*3.5*
CNC R40 - 2	*2.0*
CNC Blue 1	*2.6*
CNC Yellow 5	*3.8*
CNC Dye Mixtures	*Average = 3.69*

In the Table, Red 40-1 and Red 40-2 refer to different runs with different preparation conditions. The size distribution for the Red 40 CNC (Run 2) pigment is shown in Figure 2.15 below. The particle sizes fall within the range of 1.6 – 3.2 µm. The particle size distribution is almost Gaussian.

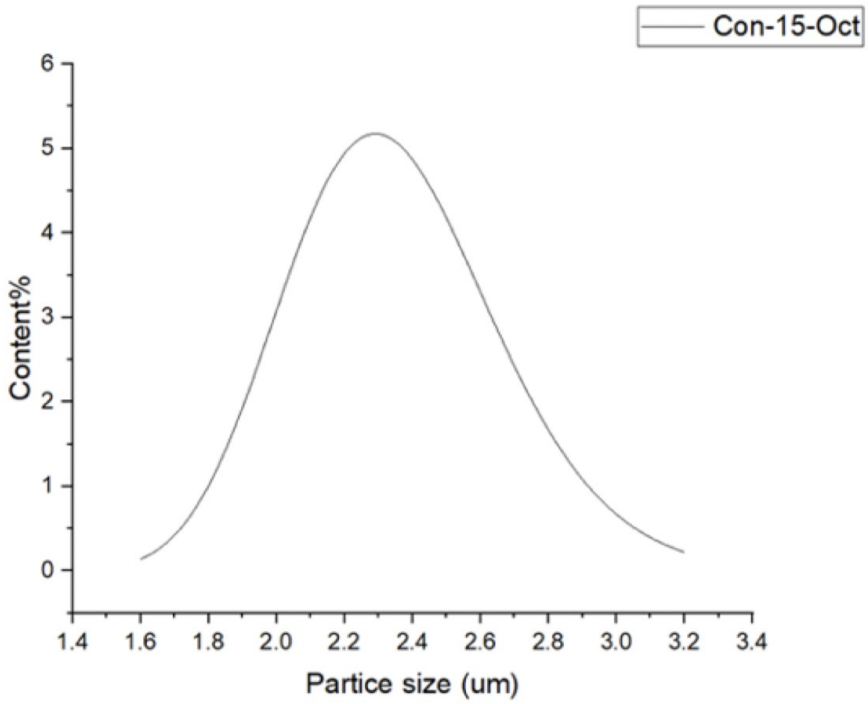

Figure 2.15: CNC Red 40 – 2, pigment size distribution.

2.3.5 Time series analysis of Red 40 pigment

The Tables below collect the raw reflectance data for all fluid media for both the cCNC Red 40 and Red 40 Lake pigments in the four different oils.

*Table 2.6: Collection of time series reflectance data, L*a*b and related parameters for cCNC Red 40 and Red 40 Lake hosted in various fluid media at 45 ^{0}C.*

Oil	Pigment	Target: at 0 time Sample: After 1 week	Target: at 0 time Sample: After 2 weeks	Target: at 0 time Sample: After 5 weeks
Malate	R40	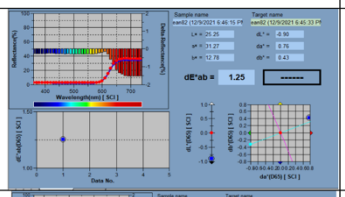	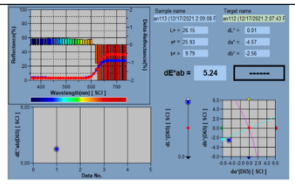	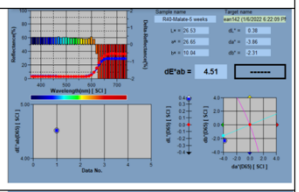
	Lake	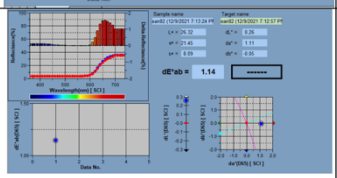	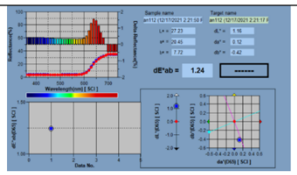	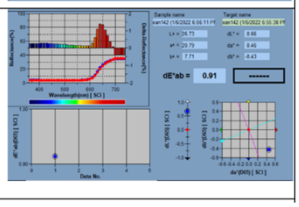
		Target: at 0 time Sample: After 1 week	**Target: at 0 time Sample: After 2weeks**	**Target: at 0 time Sample: After 5 weeks**
Crodamol (PTSI)	R40	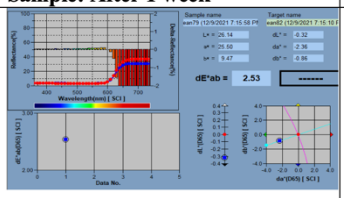	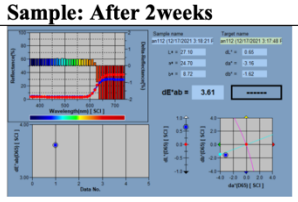	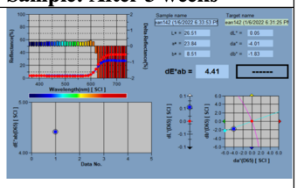
	Lake	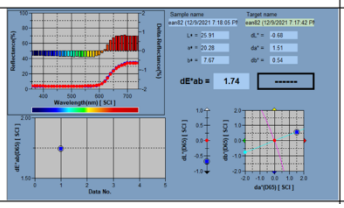	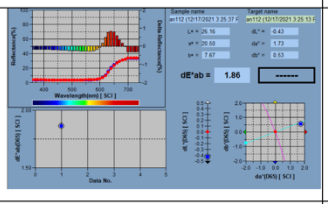	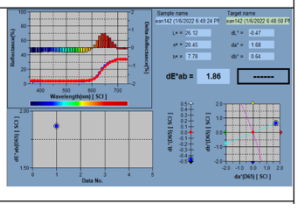
		Target: at 0 time Sample: After 1 week	**Target: at 0 time Sample: After 2 weeks**	**Target: at 0 time Sample: After 5 weeks**
Polybutene	R40	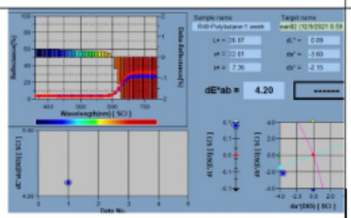	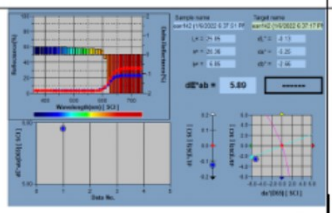	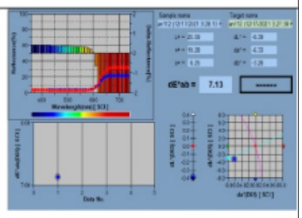
	Lake	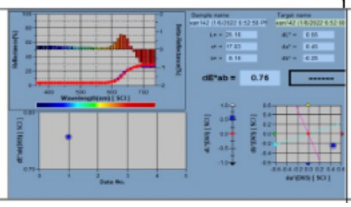	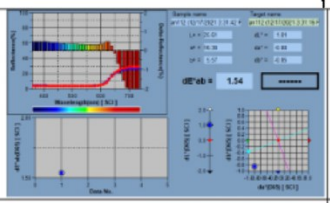	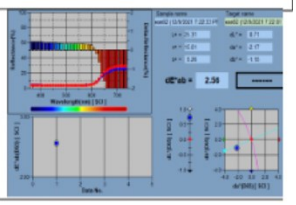

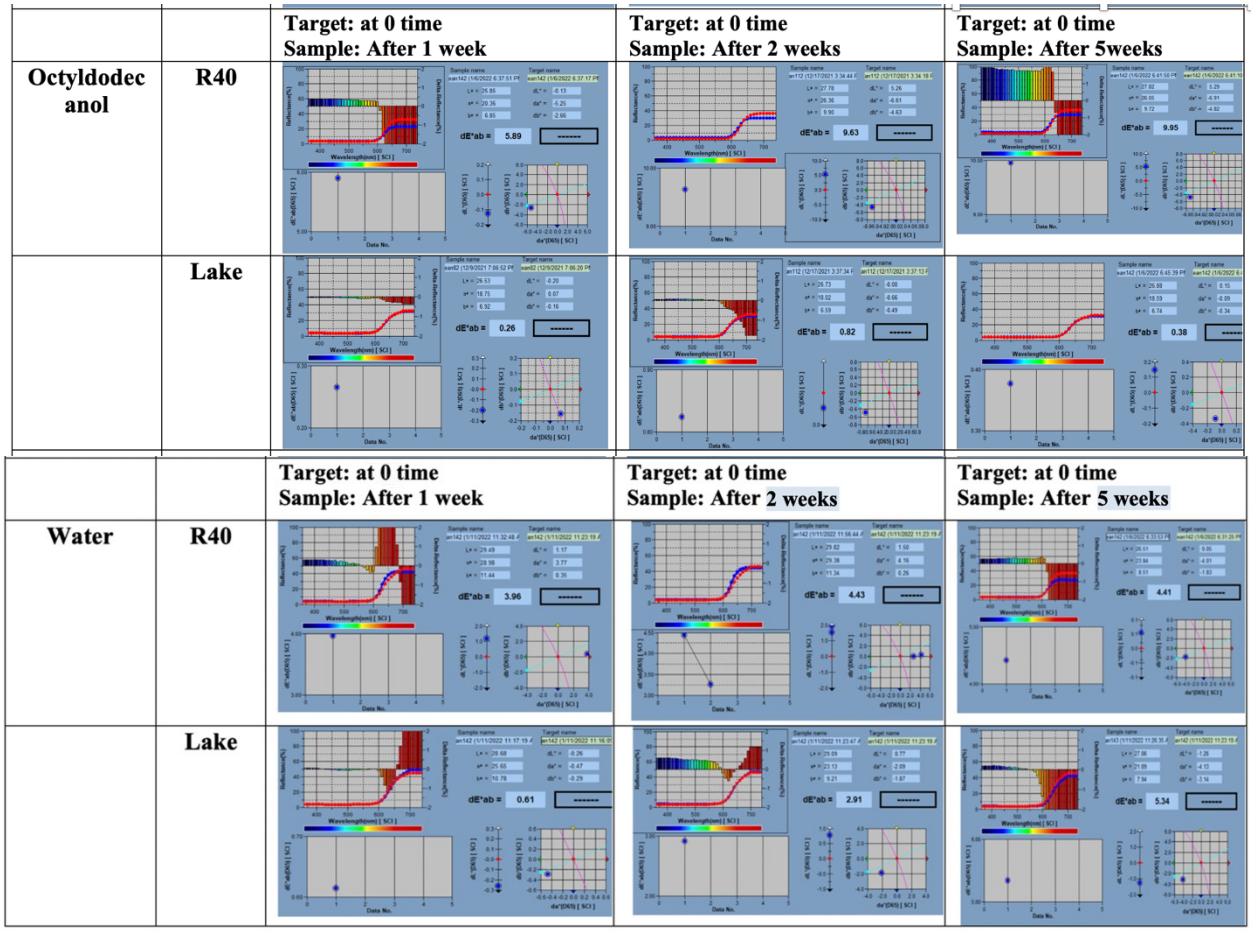

We begin with the reflectance curves. These are shown in the top left of every panel. The "Target" is a control sample, either Red 40 CNC or Red 40 Lake. These were freshly prepared in the sample fluids and not heated, which is why they are described as "at 0 time". The red dots in the reflectance curves correspond to this reference case. The blue dots correspond to reflectance from the aged samples. Above the reflectance curves, we plot the difference between the Target and Sample as a collection of bar graphs.

The first thing to note is that the Target reflectance curves for Red 40 CNC and Red 40 Lake differ in the shape of the profiles in the region 600 – 750 nm. Both curves plateau, but the reflectance for the Red 40 CNC rises more rapidly and plateaus earlier than the curve for Red 40 Lake. In both cases, the dye is the same. It is the substrate supporting the dye that differs. This observation goes to our earlier argument where we suggested that refractive index differences and size-dependent optical scattering might be responsible for the apparent difference in color quality. The difference curves tell a story that shows up with more clarity in the evolution of the

L*, a* and b* parameters. We choose only one example, malate, since interpretations for the other oils track what we say about the malate host. We turn our attention to the top left reflectance curves at weeks 1, 2 and 5. After 1 week at 45 ^{0}C, the difference plot for Red 40 CNC shows what appear to be significant changes in the red reflectance. This is evident from the negative vertical red bars in the region 600 – 750 nm. There is a decrease in reflectance of about 1.5% after 1 week, a number that increases to a maximum of 2% after 5 weeks. Interestingly, the Red 40 Lake shows a 1.5% *increase* in reflectance in the malate over the same time frame. The increase is detected as a positive bar graph difference plot that maximizes around 640 nm.

Figure 2.16 plots the luminosity of the pigments as a function of solvent and the time kept at 45 °C in the oven. Luminosity is expressed in the parameter ΔL* that presents the light-dark axis.

Figure 2.16: Plots of the change in luminosity (ΔL) as a function of solvent for both R40 CNC (blue) and Lake pigments (dark orange). The top left is the change after 1 week, the top right is for after 2 weeks and the bottom is for 5 weeks.*

Evidently, in Figure 2.16, the ΔL* parameters vary with the type of solvent and the storage time at 45 °C. The delta L* values range from less than ± 1 for almost all fluids. This means that the changes are largely imperceptible to the eye. Octyldodecanol appears as an exception. After 2 and 5 weeks the Red 40 CNC pigment shows a perceptible change in luminosity, though the change is small in terms of human eye perception. We conclude that the combinations of solvent and storage time at 45 °C in the oven have a small impact on the variable luminosity. We next examine the impact on the intensity in the red spectral range through changes in the parameter a*. The data are collected in Figure 2.17.

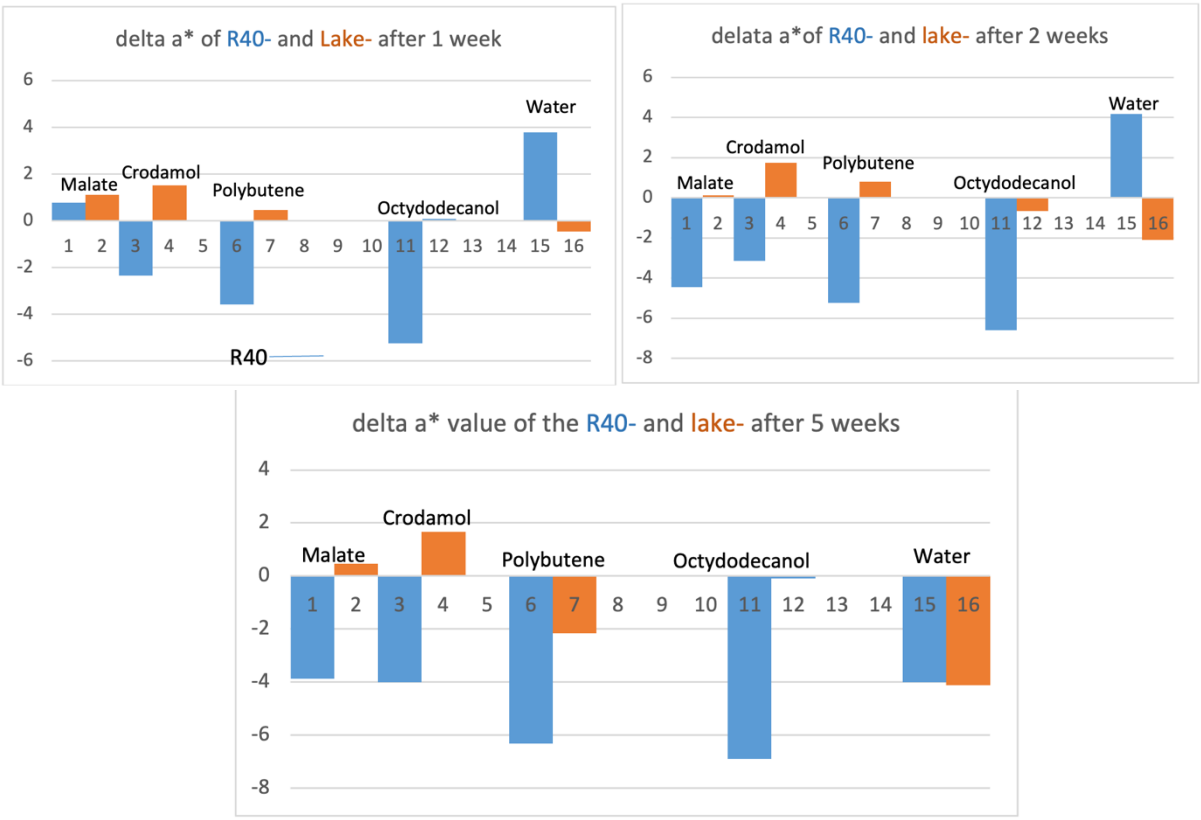

Figure 2.17: Plot of Δa values as a function of solvent for both R40 CNC (blue) and Lake pigments (dark orange). The top left is the change after 1 week, the top right is for after 2 weeks and the bottom is for 5 weeks.*

Compared with the Red Lake, the Red 40 CNC pigment tends to lose red intensity in malate and Crodamol. The largest decreases in a* occur for Red 40 CNC in polybutene 10 and octyldecanol, but overall, the color changes remain small. Both the Red 40 CNC and Red 40 Lake lose red intensity in water. In the last comparison, we examine the variations in the blue and yellow components of the pigments. These are collected in Figure 2.18.

Figure 2.18: Plots of Δb* as a function *of solvent for both R40 CNC (blue) and Lake pigments (dark orange). The top left is the change after 1 week, the top right is for after 2 weeks and the bottom is for 5 weeks.*

As shown in Figure 2.18, the Δb* parameter varies with the type of oil and storage time at 45 °C. The Red 40 CNC pigment exhibits slightly larger changes in the parameter than does the Red 40 Lake. Overall, there is a tendency to exhibit a more yellow color than blue as the samples age.

In this last section, we use digital microscopy to analyze the impact of time, temperature and the host fluid medium on the pigment particles and particle size distribution, focusing primarily on the Red 40 CNC pigment. The following figures document the outcomes:

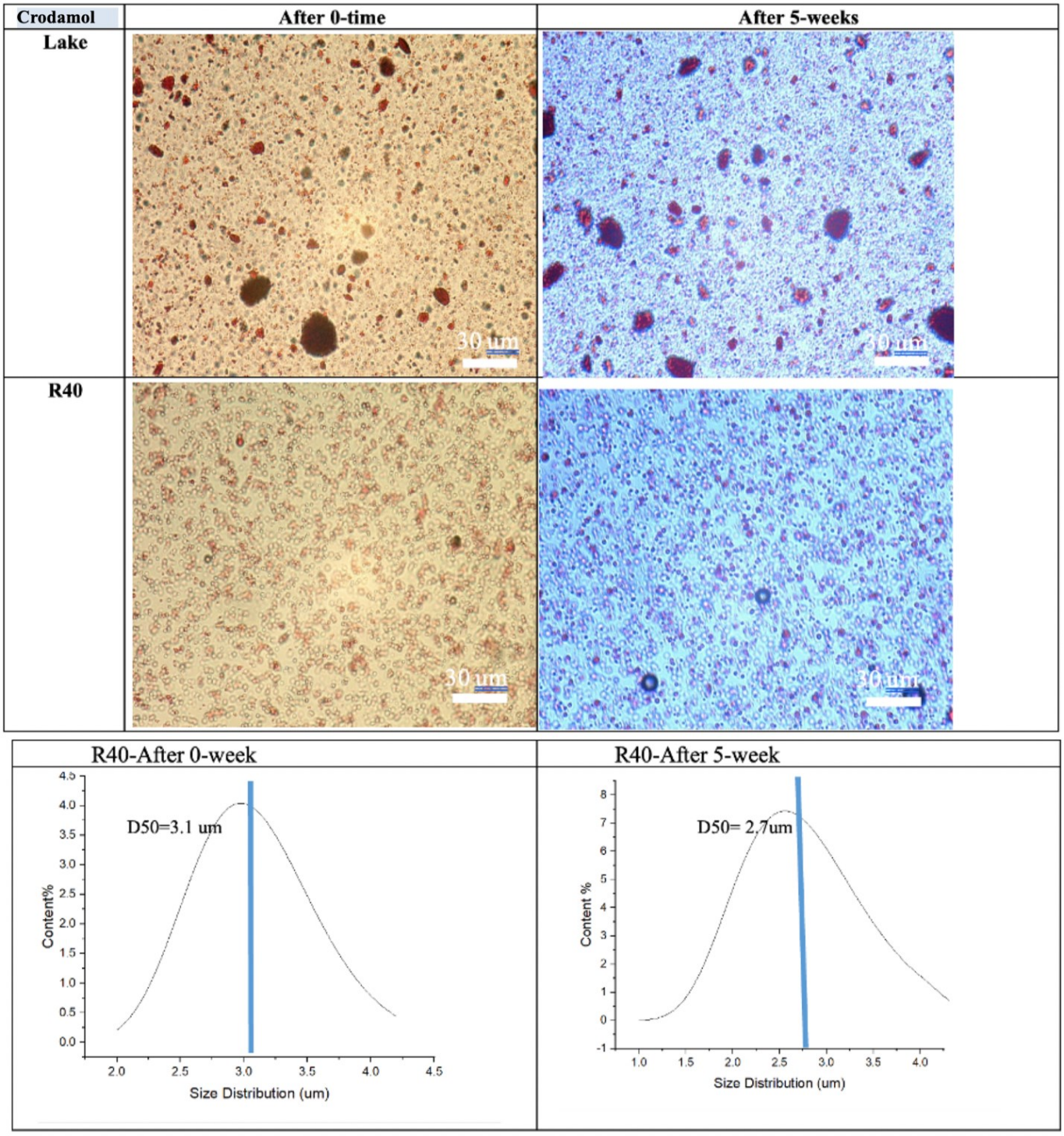

Figure 2.19: Optical microscope images and particle size distributions of Red 40 CNC and Red 40 Lake in Crodamol at week = 0 and 5 weeks at 45 °C.

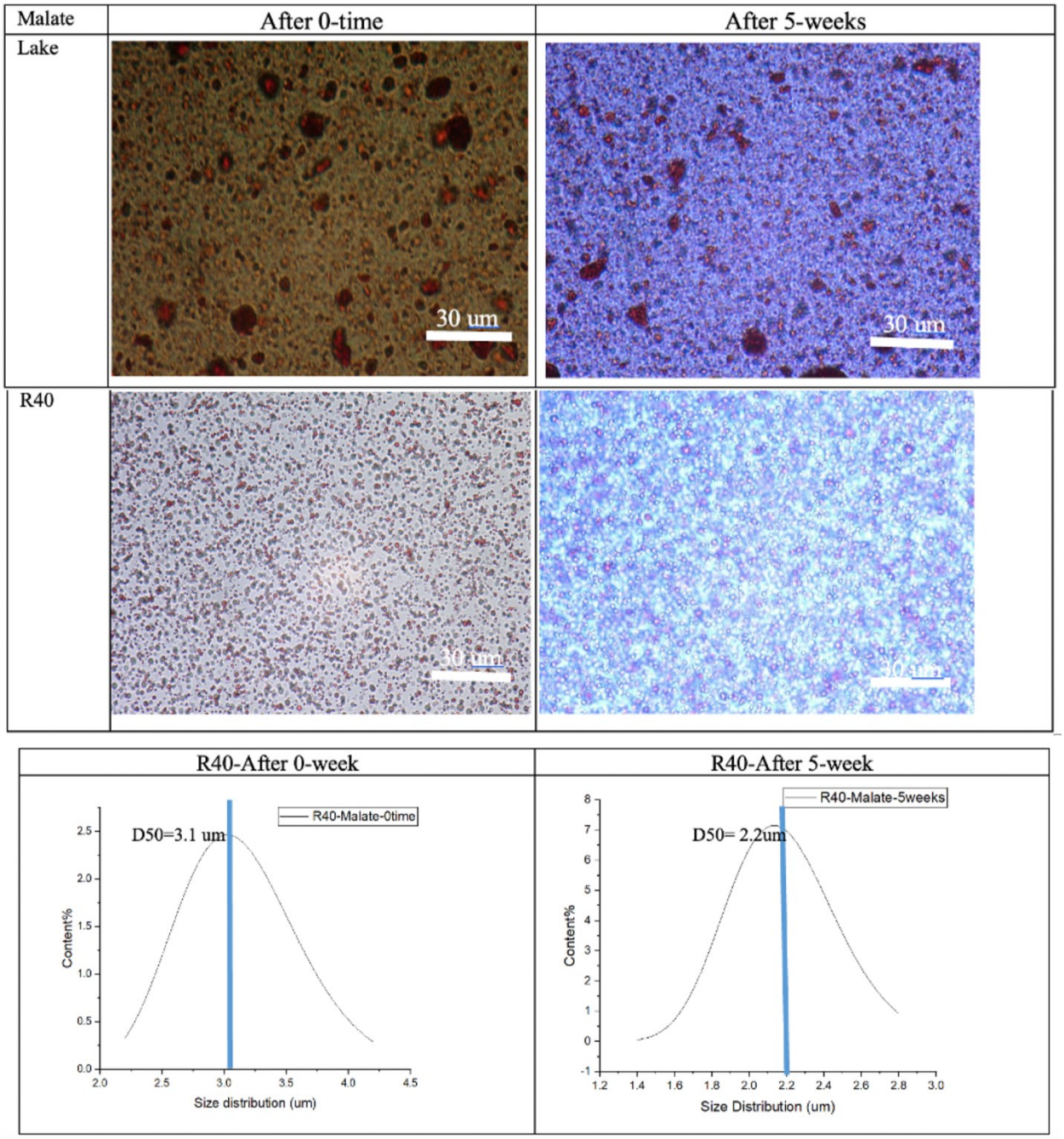

Figure 2.20: Optical microscope images and particle size distributions of Red 40 CNC and Red 40 Lake in Malate at week = 0 and 5 weeks at 45 °C.

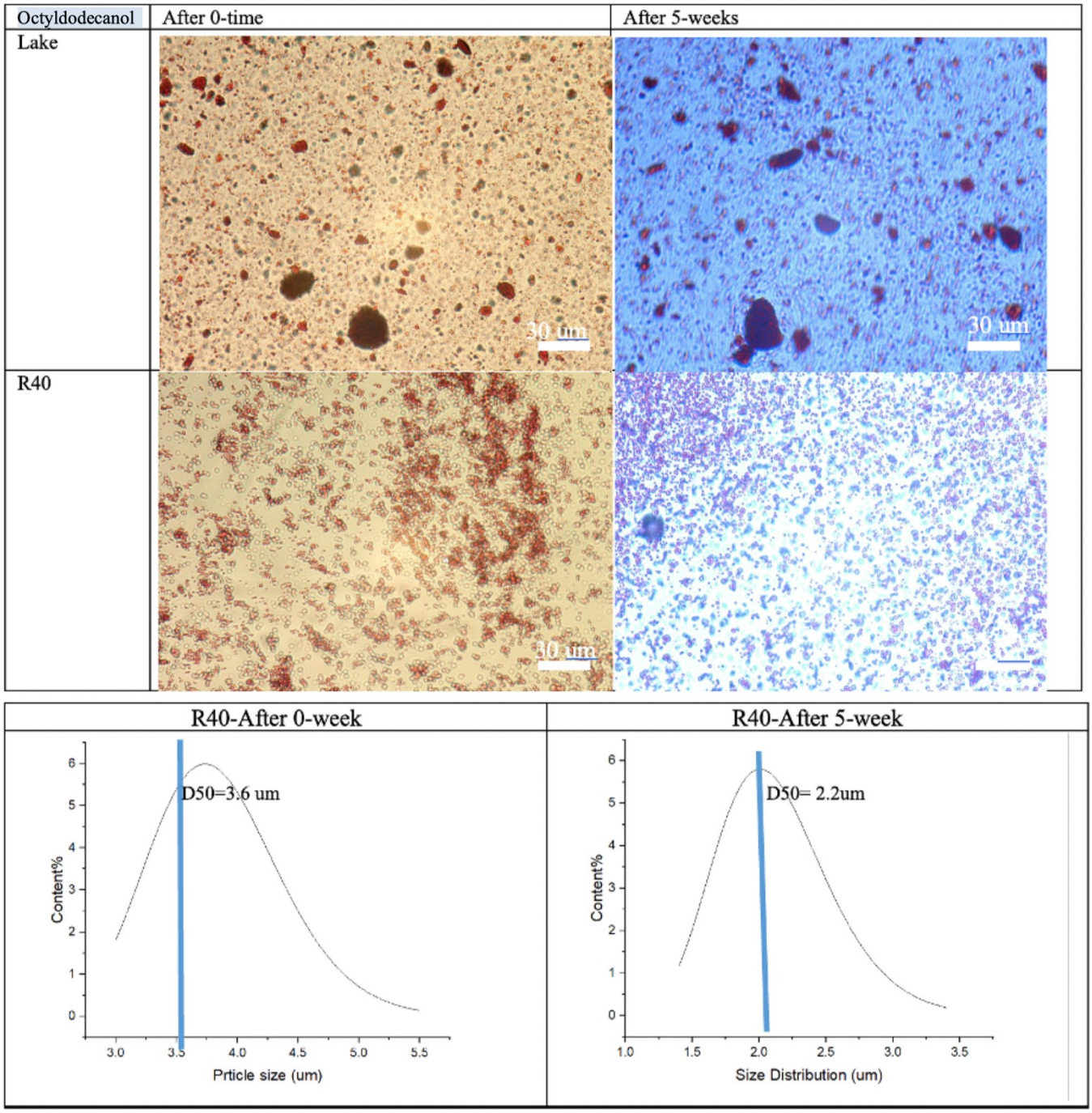

Figure 2.21: Optical microscope images and particle size distributions of Red 40 CNC and Red 40 Lake in octyldodecanol at week = 0 and 5 weeks at 45 °C.

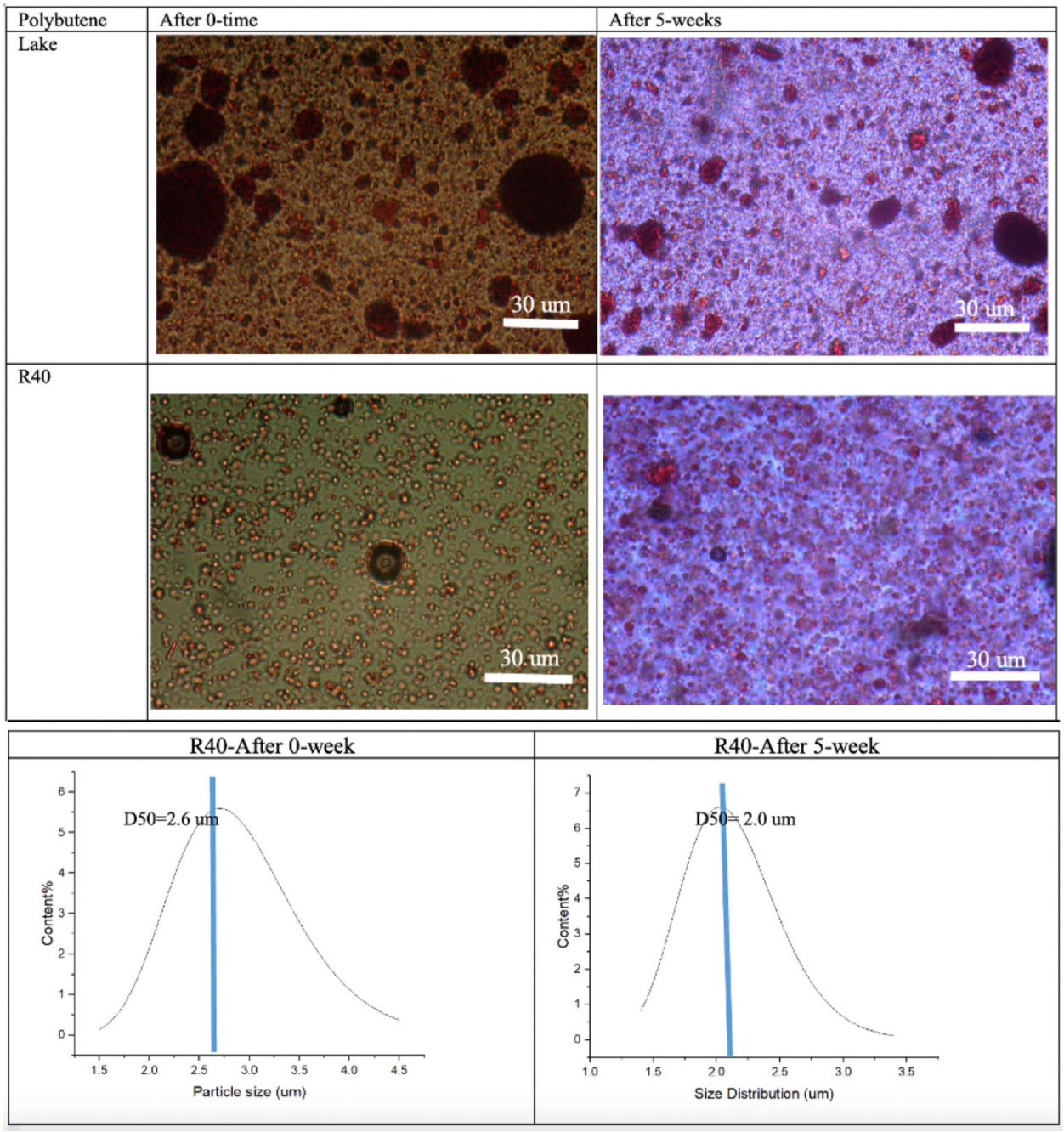

Figure 2.22 Optical microscope images and particle size distributions of Red 40 CNC and Red 40 Lake in Polybutene 10 at week = 0 and 5 weeks at 45 °C.

Figures 2.19, 2.20, 2.21, and 2.22 show the optical images of R40 CNC and lake which were mixed in Crodamol, diisostearoyl malate, octyldodecanol, and Polybutene oil after zero weeks (no heating) and five weeks at 45 °C, respectively. As can be seen in all of the figures, the Red 40 CNC pigment retains what appears to be a spherical shape in all the media even after 5

weeks at 45 ^{0}C. The Red 40 Lake particles are highly irregular in size and shape. This is evident from optical microscopy. Changes in the particle size distributions for the Red 40 Lake are evident after 5 weeks in the oven at 45°C. In every case, the particle size decreases after 5 weeks of thermal treatment in the oils. A possible explanation is that the microbeads shed nanocrystals during the thermal treatment.

2.4 Conclusions

CNC based pigments were produced for four individual dyes, Blue 1, Red 40, Yellow 5, and a naturally derived green dye. Pigments were also made by mixing two dyes on individual microbeads to make green, orange, and 'purple' pigments. The CIE L* a* b* values for all pigments were obtained to characterize the color of the dyes and compare them with their respective Lakes. Unsurprisingly, despite the same Red 40 dye present in both the Lake and the cellulose microbead, there were visibly noticeable differences in their respective color characteristics. Saturation and coverage values for the red CNC pigment and lake were obtained due to their significant value in cosmetics. It was found that at 10% dye loading in the cellulose microbead, the red lake had better coverage, most likely due to the 4 times larger loading of dye in the Lake. Coverage and saturation are affected by pigment morphology. Pigment morphology was explored using SEM. For cCNC, cCNC^{+}, and the CNC pigments all were found to have the desired spherical shape. The average size of all the pigments was also well below 4 μm as intended. High resolution SEM revealed that cCNC microbeads comprise agglomerates of nanocrystals on the surface, but upon the addition of PDDA, the surface became mostly smooth.

For use in conventional cosmetic formulations, the color stability and resistance to fragmentation of the Red 40 CNC pigment were tested in different media. It was found that there were small changes to the reflectance data that were imperceptible to the human eye for both the Red 40 CNC and the lake in the different mediums. We documented changes in luminosity with respect to Δb* and Δa*. We observed that the CNC pigment underwent larger changes when compared to those of the lake. Using digital microscopy, we established that during the time series, the microbeads maintain their spherical shape. Measurements of particle size from the microscopy images revealed that the microbeads become smaller throughout the testing period. This is possibly caused by nanocrystal shedding during thermal treatment.

2.5 References

1. Morse, T. Nanocrystalline Cellulose: Surface Chemical Transformation and Applications. McGill University, 2015.
2. Dalwadi, G.; Benson, H. A.; Chen, Y., Comparison of diafiltration and tangential flow filtration for purification of nanoparticle suspensions. *Pharmaceutical research* **2005,** *22*, 2152-2162.
3. Dobry, D. E.; Settell, D. M.; Baumann, J. M.; Ray, R. J.; Graham, L. J.; Beyerinck, R. A., A model-based methodology for spray-drying process development. *Journal of pharmaceutical innovation* **2009,** *4*, 133-142.
4. Khuenpet, K.; Charoenjarasrerk, N.; Jaijit, S.; Arayapoonpong, S.; Jittanit, W., Investigation of suitable spray drying conditions for sugarcane juice powder production with an energy consumption study. *Agriculture and Natural Resources* **2016,** *50* (2), 139-145.
5. Vicente, J.; Pinto, J.; Menezes, J.; Gaspar, F., Fundamental analysis of particle formation in spray drying. *Powder technology* **2013,** *247*, 1-7.
6. Peng, Y.; Han, Y.; Gardner, D. J., Spray-drying cellulose nanofibrils: Effect of drying process parameters on particle morphology and size distribution. *Wood and Fiber Science* **2012**, 448-461.
7. Vehring, R.; Foss, W. R.; Lechuga-Ballesteros, D., Particle formation in spray drying. *Journal of aerosol science* **2007,** *38* (7), 728-746.
8. Ly, B. C. K.; Dyer, E. B.; Feig, J. L.; Chien, A. L.; Del Bino, S., Research techniques made simple: cutaneous colorimetry: a reliable technique for objective skin color measurement. *Journal of Investigative Dermatology* **2020,** *140* (1), 3-12. e1.
9. X-Rite Pantone A Guide to Understanding Color. https://www.xrite.com/-/media/xrite/files/whitepaper_pdfs/l10-001_a_guide_to_understanding_color_communication/l10-001_understand_color_en.pdf (accessed May 2).
10. Endress + Hauser Group Services Process Spectrometer for Robust Inline Quality Control. https://www.pcne.eu/article/process-spectrometer-for-robust-inline-quality-control/ (accessed May 2).
11. Nix Color Sensor How do you Measure Color Accuracy. https://www.nixsensor.com/blog/measure-color-accuracy/ (accessed May 2).
12. Beetsma, J. The CIELAB L*a*b* System - the Method to Quantify Colors of Coatings. https://knowledge.ulprospector.com/10780/pc-the-cielab-lab-system-the-method-to-quantify-colors-of-coatings/ (accessed May 4).
13. Kong, X.; Murdoch, M. J.; Vogels, I.; Sekulovski, D.; Heynderickx, I., Perceived speed of changing color in chroma and hue directions in CIELAB. *JOSA A* **2019,** *36* (6), 1022-1032.
14. Rasband, W., ImageJ https://imagej. nih. gov/ij. *Bethesda: National Institutes of Health* **2018**.

Chapter 3- CNC-Polyelectrolyte Complex for CNC-Based Pigments

3.1 Introduction

In the introductory chapter 1, we described some features of polyelectrolytes. Here, we continue the description by examining in more detail the polyelectrolyte complex for CNC-based pigments.

The zeta potential is an important polyelectrolyte metric. For a particle or surface, the zeta potential measures the interface between the mobile fluid medium and the fluid medium that is bonded to the surface. Figure 3.1 shows this interface, which is called the slipping plane.

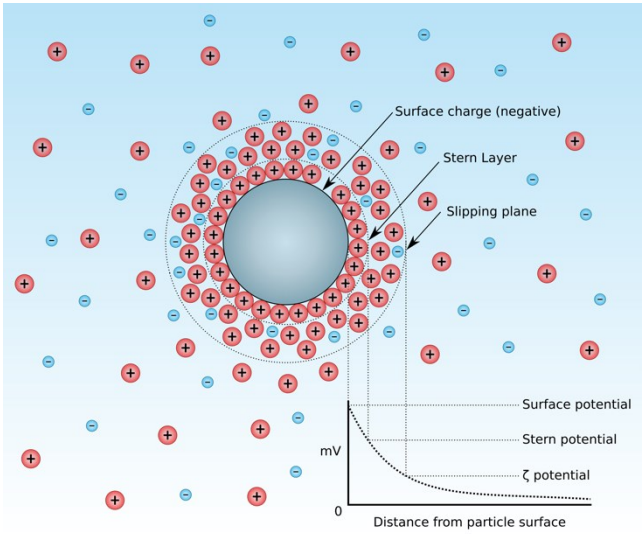

Figure 3.1: Diagram representing the location of the slipping plane & zeta potential for a colloidal particle.[1]

The potential at the interface between the slipping plane and the bulk fluid marks the zeta potential. This is indicated in the illustration by the black and white potential diagram at the bottom right. One observes that the potential falls off roughly exponentially from the particle surface. In the Figure, the surface charge is clearly negative, offering a potential that can attract positive ions. The Stern layer is the layer of charged ions bound to the surface of a charged particle in a solution. The Stern layer is charged opposite to the net charge of the particle surface. Observe that there exists a second diffuse layer composed of both positive and negative ions that are loosely charged. These two layers together are referred to as the electrical double layer. A distinction is made between particles that are within these two layers and particles that are free in solution. The zeta potential is inherently related to the surface charge of the particle.[2] Tracking the movement of charged particles of a solution in an electric field can be used to measure zeta

potential. A value of less than ±15 mV usually represents solutions with agglomeration. Solutions with a value of greater than ±30 mV generally represent solutions with enough repulsion to allow colloidal stability.[3] It is important to remember that in the process of charging the surface from highly negative to highly positive, there will be a period where the surface potential is close to zero. Even if the starting and ending particles in the solution have zeta potentials that theoretically would be stable, aggregation may occur due to the transition through the region of low zeta potential. During this period, there is partial coverage of the surface which leads to the formation of irreversible aggregates. As a result, turbidimetry that quantifies the turbidity of a suspension can be used to detect the formation of agglomerates due to particle-particle aggregation.

Turbidimetry measures the amount of light that is scattered by suspended particles as it passes through a sample.[4] Since optical scattering is wavelength dependent, turbidity can be measured by scanning through various spectral wavelengths, much as is done in an electronic absorption experiment. Indeed, in some cases of turbidimetry, both absorption and scattering occur, and these events are not mutually exclusive Scattering is an elastic photon event, meaning that the incoming and scattered wavelength are identical. Scattering = excitation + reradiation, since the basis of scattering is the oscillatory motion of electrons caused by the electric field of the incident wave. A sample with high turbidity will appear cloudy. Turbidimetry measures the transmitted light, i.e., light scattered (transmitted) in the forward direction towards a photodetector. The scattering of light depends on the size of the particle (and shape) and fluctuations in the concentration and orientations of particles. A wavelength centered at 410 nm is often used in the turbidimetric determination of colloid-sized particles.[5] When the particles are of nanometer dimensions, laser light scattering is the method of choice. Turbidimetry, therefore, offers a way to analyze $cCNC^{+}$ suspensions, especially effects due to particle interactions when agglomeration produces scatterers of colloidal dimensions. This is important if we are to discover optical regimes where the nanocrystals are not aggregated, which is the desired condition of the polyelectrolyte complex between cCNC and PDDA. Afterall, we are interested in binding dye molecules to individual nanocrystals, not agglomerates of them. Thus, it becomes important to measure if agglomeration occurs when mixing PDDA with cCNC.

Explorations of the UV-Vis spectra of the $[cCNC\text{-}PDDA]^{+}$ PEC with dye molecules can give information on the binding interactions based both on the shifts in the peak maxima which

occur and the relative change in absorbance as a function of wavelength. Moreover, one can learn about the strength of the binding of a dye by studying the desorption process, i.e., the tendency of the dye to leach from the pigment particle. Leaching (desorption) studies allow quantitative or qualitative assessment of the strength of dye + PEC interactions. Dye binding strength is important for color fastness in textiles and cosmetics.[6] This chapter examines aspects of dye-cCNC$^+$ binding in this class of pigment particles.

3.2 Experimental

3.2.1 Materials

Carboxylated cellulose nanocrystals (cCNC, trade name DextraCel) were supplied as a 3.75 wt. % aqueous suspension by Anomera, Inc. High molecular weight (400,000-500,000 M_w) PDDA (Poly(diallyldimethylammonium chloride)), 20 % in water was purchased from Sigma Aldrich. The following anionic dyes were used (see Chapter 2 p. 34, Figure 2.8): FD&C Blue 1, Erioglaucine disodium salt (Sigma-Aldrich). FD&C Yellow 5, Tartrazine (≥ 85%, Sigma-Aldrich). FD&C Red 40, Allura Red AC (≥ 80%, Sigma-Aldrich). The botanically derived green pigment was prepared from copper chlorophyllin, supplied by Natpure as Col Green LC 717. The orange pigment was prepared by binding 1:1 Allura Red 40 and Yellow 5 to cCNC$^+$ as described in Chapter 2, Experimental. A green pigment was prepared by binding 1:1 Yellow 5 and Blue 1 to cCNC$^+$ as described in Chapter 2, Experimental. Similarly, a purple pigment was prepared by co-binding 1:1 Blue 1 and Allura Red 40 to the cCNC-PDDA complexes.

A 6 mm Sonics microtip horn was used in combination with a Sonics vibra-cell VCX 130 probe sonicator. For purification, a diafiltration system based on a Repligen Minikros Sampler 20 cm with a 10 kDa diafiltration tube was used together with a MasterFlex L/S® 36 high-performance precision peristaltic pump (MasterFlex L/S easy-load II pump head) and associated tubing. Spray drying was done with a Buchi Mini Spray Dryer B-191.

A Cary 5000 UV-Vis-NearIR spectrophotometer from Agilent provided turbidimetric and absorption spectroscopy over a wavelength range from 190-3300 nm.

3.2.2 Reversing the Surface Charge of cCNC

To convert negatively charged cCNC to a positive potential substrate for binding anionic dyes, a 70 mL suspension of cCNC in water (0.96 % wt., 0.67 g) was prepared and equipped

with a stir bar. The suspension was simultaneously dispersed with the Sonics Vibra-cell VCX130 probe sonicator with 5 minutes of sonication at 100% power output. Immediately following sonication, a 40 mL solution of PDDA (0.068% wt.) was dispersed by agitation with a magnetic stir bar. $cCNC^+$ samples with variable amounts of PDDA were prepared by combining 10.4 mL of cCNC suspension with quantitative amounts of the PDDA, in volumes ranging from 0 to 10 mL. An additional 20 mL sample was prepared (sample G in the Table below), with a final concentration of 0.49 % cCNC and 0.069 % PDDA. The concentrations of all the solutions are collected in Table 3.1. Samples of $cCNC^+$ were sonicated for 1 minute at an amplitude of 50 % and a pulse of 10 seconds on and 10 seconds off. The total dispersion (mixing) time was 2 minutes. The pH and ionic strength of the samples were unchanged during sample preparation.

Table 3.1: Sample Concentrations of cCNC and PDDA

Sample	**cCNC Solution (g)**	**cCNC Conc. (% wt.)**	**PDDA Solution (g)**	**PDDA Conc. (% wt.)**	**H_20 Volume (mL)**	**Total Volume (mL)**
A	10.4	0.49	0	0	10	20.4
B	10.4	0.49	2	0.007	8	20.4
C	10.4	0.49	4	0.014	6	20.4
D	10.4	0.49	6	0.021	4	20.4
E	10.4	0.49	8	0.027	2	20.4
F	10.4	0.49	10	0.034	0	20.4
G	10.4	0.49	10 (different stock)	0.069	0	20.4

3.2.3 Zeta Potential

The zeta potential of the $cCNC^+$ suspensions with varying amounts of PDDA was measured using a ZetaPlus zeta potential analyzer from Brookhaven Instruments Corporation. Samples A to F from Table 3.1 were analyzed. The instrument was set at Temp. (°C): 25.00, Viscosity (cP): 0.8900; Refractive Index: 1.3310; pH: 7.00. Cell and electrode cell Description: Square Polystyrene Cell Electrode Assembly: BI-ZEL (1,250 µL).

3.2.4 Turbidimetric Titration

Turbidimetry results were obtained by acquiring the Cary 5000 transmittance of all samples, A to G from Table 3.1. Turbidimetry is calculated by subtracting the percent

transmittance of a sample at a given wavelength from 1. The transmittance of each sample was determined between 250-750 nm. The samples were analyzed in a random order with triplicates of each being obtained. To avoid differences between measurements due to coagulation, the samples were mixed by shaking before pipetting the sample into the cuvette. Each spectrum was baseline corrected by averaging the signal from 750 to 725 nm, then subtracting from the spectrum.

3.2.5 CNC Pigment Preparation

A 200 mL suspension of cCNC in water (0.5% w/v, 1 g) was prepared in a 600 mL beaker with sonication and magnetic stir bar agitation. A 4 mL solution of PDDA in water (3.5% w/v, 0.14 g) was added all at once to the cCNC solution. Immediately before adding this combination of materials, slow stirring and pulse sonication at 70% output (10 s on, 5 s off) were turned on. Mixing and sonication were continued for 37.5 minutes total (time including when the sonicator was off) to yield a viscous fluid suspension. The sample was purified by diafiltration until the conductivity of the water permeate was 30 μS/cm or less, yielding a stable translucent suspension of positively charged $cCNC^+$.

To prepare the dye-bound nanocrystals, a 200 mL suspension of $cCNC^+$ (0.5%, 1g) was rapidly blended with a 3-blade Rayneri mixer in a 600 mL beaker. Then 20 mL of dye dissolved in water (0.5 % w/v, 0.1 g) was slowly added to the $cCNC^+$ suspension stirred at 700 rpm. After adding the dye, stirring at 700 rpm was continued for an additional 20 minutes. The colored suspension was then spray-dried with the Buchi model B191 dryer as a 220 mL sample. The following parameters are relevant: 175 °C inlet temperature, 30% pump speed, and 70% aspirator.

3.2.6 Individual Dye Molar Absorptivity

Beer's law calibration curves for the three individual free dyes were obtained in distilled water using a Cary 5000 UV-Vis spectrophotometer. 6 dye concentrations were prepared quantitatively in standard volumetric flasks. The absorbance for each individual dye was obtained at its respective maximum wavelength. The data were plotted in the standard way.

3.2.7 Pigment Leaching

Dye leaching studies were conducted for all CNC pigments and Lake pigments. To determine each pigment, two 6-dram vials were filled with 10 mg of the pigment and 5 mL of distilled water. The vials are then mixed for 15 seconds using a vortex mixer. The vials were stored in the dark when not in use. Of the two pigment vials, one pigment sample was analyzed after 24 hours and the second after 48 hours. During this time, the pigment particles/microbeads settled to the bottom of the vials. After the designated time had elapsed (24 or 48 hours) the supernatant was extracted with a Pasteur pipette. A quantitative amount of supernatant was then diluted with water to a volume of 10 mL. The dilution was done to ensure sufficient volume to obtain UV-Vis spectra in triplicate. The volumes of samples used in the leaching studies were corrected to the initial concentration. The UV-Vis spectra were obtained for each sample in triplicate with the absorbance being obtained between 250-750 nm.

3.2.8 Dye Binding with cCNC$^+$

The cCNC$^+$ was prepared as described earlier (section 3.2.5). First, a solution of cCNC was diluted to make a 0.5% w/v suspension of cCNC in 200 mL of DI water. Next, PDDA was diluted to 3.5% w/v in 4 mL of DI water. The PDDA solution was then added to the cCNC suspension with sonication and magnetic stir bar agitation. Sonication was undertaken using a 13 mm probe for 25 minutes (37.5 minutes total), with a pulse of 10 secs on and 5 secs off. The sonication amplitude was set to 70%. The resulting cCNC$^+$ was purified by diafiltration until the conductivity of the water permeate was 30 μS/cm or less.

Dyed samples for the leaching studies were prepared with approximately 15 g of the cCNC$^+$ suspension as described in the paragraph above. The samples are labelled alphabetically (A, B, …, etc.) with each sample accounting for an increasing increment (50 μL) of dye stock solution. For clarity, sample A comprises 50 μL, B 100 μL, C 150 μL and so on. The 25 mL dye stock solution was prepared at 0.05 % w/v (0.0129 g in 25 mL). After adding the dye solution to cCNC$^+$, the samples were mixed using a vortex mixer until the dye was evenly dispersed.

The absorption spectra of each sample were obtained in triplicate within 24 hours of preparation. Depending on the identity of the dye, different wavelength regions were probed.

Each spectrum was baseline-corrected by averaging the signal from 750 to 725 nm and subtracting the average value from the spectra.

3.2.9 Increased Red Dye Content CNC Pigment Samples

See section 3.36. A sample of Red 40 CNC pigment was produced with an increased amount of red dye. The procedure was the same as the original pigments (section 3.26). The only difference was that the dye solution that was added and mixed with the $cCNC^{+}$ had a concentration of 0.8 % w/v, 0.16 g of dye in 20 mL of DI water. This meant that the dye loading was increased from 10 % to now being 16 %.

3.2.10 Optical Characterization of the Increased Dye Content Red 40 CNC Pigment

The reflectance values of the 16 % dye CNC pigment were obtained with the Konica Minolta Sensing spectrophotometer CM-700d (Chapter 2). Optical data were processed using the Spectra Magic NX Colour Data Software, CM-S100w. Pigment powder (~30 mg) was added to a 1-dram vial to provide a uniform layer across the bottom of the vial. The vial was then placed on top of the specimen measuring port of the spectrophotometer and the reflectance values were obtained.

Coverage and saturation values were obtained for the increased dye content Red 40 CNC pigment. The pigment was dispersed with 1g of diisostearyl malate (Salacos 222) in a 7-dram vial, and 4 different concentrations were prepared, (1, 2, 3, 4 wt. %). The sample was then mixed for 15 seconds using a vortex mixer to ensure uniform dispersion. The red fluids were sampled with a Pasteur pipette and droplets were deposited on a microscope slide. A glass cover slip was then placed over the sample. The a^* and b^* values were obtained with the CM-700d spectrophotometer and then used to calculate the saturation of the samples. For coverage, the sample L^* value was obtained with a white sheet behind the microscope slide. Then the sample L^* value was obtained with a black sheet behind the microscope slide. The difference between the black background L^* from the white background L^* was reported as the coverage value for the sample.

3.3 Results and Discussion

3.3.1 Zeta Potential Analysis of cCNC and cCNC$^+$

The zeta potentials as functions of the added PDDA are collected in Table 3.2 (See Table 3.1 for notation). The purpose of the Table is to identify approximately what concentration of PDDA is required to reach a balance on the combined surface potential that is sufficient to keep the nanocrystals apart (electrostatic repulsion) so that the incoming dye molecules bind to individual nanocrystals and not agglomerates of them. In the absence of PDDA, the cCNC in water at neutral pH is negatively charged owing to the surface carboxyl groups. With the simple application of the Henderson-Hasselbalch equation, and assuming a pKa on the order of 4 for a typical organic acid RCH_2COOH (i.e., at the C6 position of the glucose ring), we find that at neutral pH the carboxylic acid groups are 99.90% ionized (as $RCOO^-$), making the water somewhat acidic. Potentiometric titration gives a carboxy content of 0.15 mmol/g .[6] Systematic additions of PDDA neutralize and then invert the surface potential of the nanocrystals.

Table 3.2: Zeta potential for cCNC suspensions with different quantities of PDDA

Samples / PDDA Quantity (g)	**Zeta potential (mV)**
A / 0	-57.64± 0.2
B / 2	-16.49± 0.3
C / 4	+19.05± 0.5
D / 6	+50.11± 0.5
E / 8	+53.67± 0.1
F / 10	+60.42± 0.4

Samples B and C bracket the region where the polyelectrolyte partially covers the nanocrystals. Referring to Table 3.0, for a sample of 0.49 w% cCNC, there will be partial coverage of the nanocrystals at a concentration of PDDA between 0.007 % and 0.014 %. In terms of pigment preparation, this corresponds to a relative concentration of 2 % PDDA with respect to cCNC where we require the onset of reversal of the surface charge. Given the known low surface charge density on cCNC, only a small concentration of PDDA, at fixed molecular weight, is required to begin to reverse the charge.

3.3.2 Turbidimetric Titration of cCNC and $cCNC^{+}$

The purpose of this study was to determine the range of conditions over which one might expect to obtain a polyelectrolyte-cCNC complex suitable for binding of anionic dye molecules. Flocculation during PEC formation is undesirable. Flocculation can occur via polymer (PDDA) bridging, charge neutralization, and polymer adsorption. Any of these events can destabilize the cCNC-polyelectrolye interaction species. Adsorption of polyelectrolytes onto oppositely charged surfaces like anionic $cCNC^{-}$ is a very complex process that can be affected by changes in the balance of interactions occurring in the solution, and those between the solution and the solid nanoparticle surface. This balance depends on pH, ionic strength, presence of surfactants, polymer charge density, solvent medium and polymer molecular weight. Turbidimetry combined with zeta potential measurements and studies of dye interactions with polycations and cellulosic interfaces can provide insight into the stability regime required to optimize the binding of dye molecules. Variables that modify the ionic equilibrium of polyelectrolyte solutions can ultimately affect the process of deposition onto solid surfaces, and in our case, the formation of the PDDA polyelectrolyte complex with cCNC particles. We note that reductions in the effective charge density of the polyelectrolyte will drive polymer chains to adopt a coiled conformation. This is the result of charge screening that reduces the intra- and inter-chain electrostatic repulsions. One consequence is that the polyelectrolyte (PDDA in our case) can deposit as multilayers with chain loops and tails protruding into the fluid medium. Increases in the effective charge density of the polymers drive polymer chains to adopt a more extended conformation. In this case, the polymer might be better able to attach to a surface in an extended conformation, resulting in the deposition of a thin layer. How these variables in detail affect dye binding and dye stability in CNC-based pigment particles, go well beyond the scope of this thesis. Nevertheless, important insights into the pigment particles can be acquired by summoning some simple investigative tools.

Samples for turbidimetry were obtained under two different mixing conditions. The first used mixing with a magnetic stir bar and the second used sonication. The purpose of this study was to investigate the impact of mixing conditions on the turbidity of the cCNC/PDDA PECs. Mixing was introduced to try to break up agglomerates that might arise from the addition of aliquots of PDDA to the cCNC. We first show the results for turbidimetric titration with mixing

by magnetic stir bar. These are assembled as images in Figure 3.2 A and plotted as functions of PDDA concentration in %w/v in Figure 3.2 B.

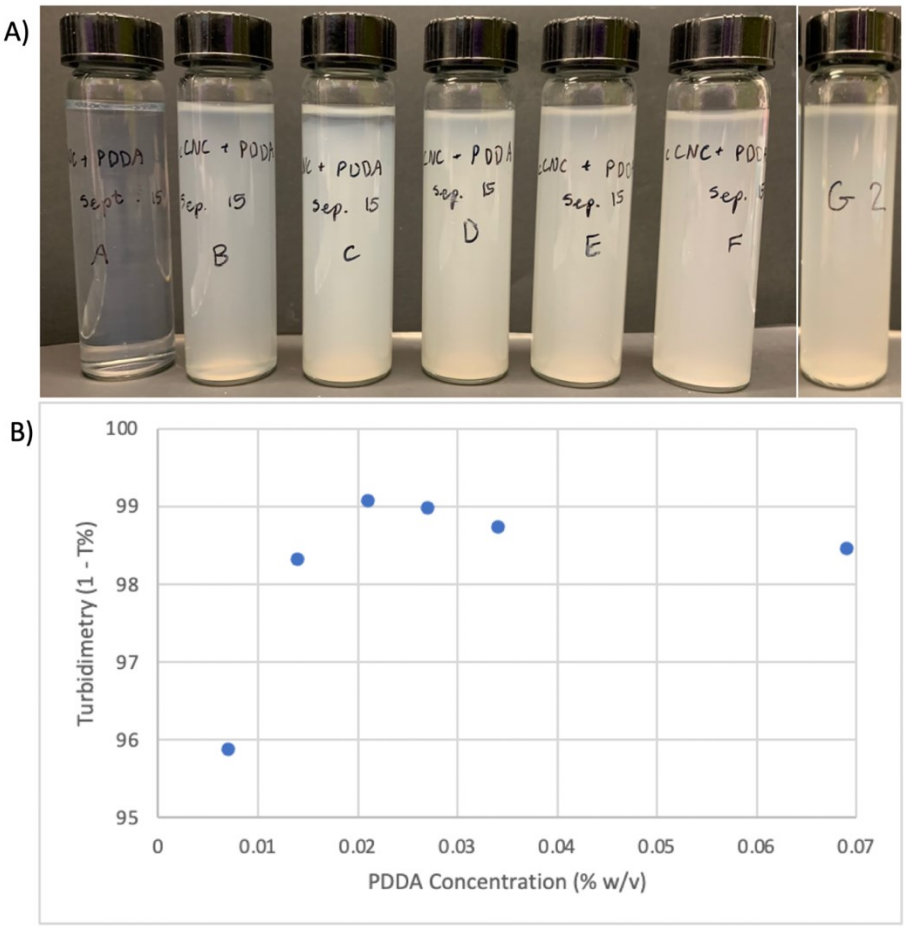

Figure 3.2: A) Image of all cCNC and cCNC$^+$ samples with different quantities of PDDA prepared by stir bar mixing. B) Turbidimetry results for samples B – G

Sample A contains no PDDA (See Tables 3.1 and 3.2). It can be seen in Figure 3.2 that on addition of 0.007 wt% PDDA (sample B) the suspension becomes cloudy. This is due to flocculation, which is the result of contact and adhesion of particles cCNC$^+$ particles caused by additions of charge screening PDDA. Flocculation is synonymous with agglomeration. The plot in part B beneath the images shows the increasing turbidity with added PDDA. The turbidity plateaus between 98-99%. The zeta-potential results in Table 3.2 show that samples D - G have acquired a positive surface charge, where aggregation would not be expected. This means that the flocculation is likely due to irreversible binding which occurs immediately after adding PDDA to cCNC (perhaps assisted by bridging PDDA polymer chains across cCNC crystallites).

This means that mixing with a stir bar was not sufficient to disperse cCNC$^+$ particles. To test this, we repeated the study with mixing by ultrasound.

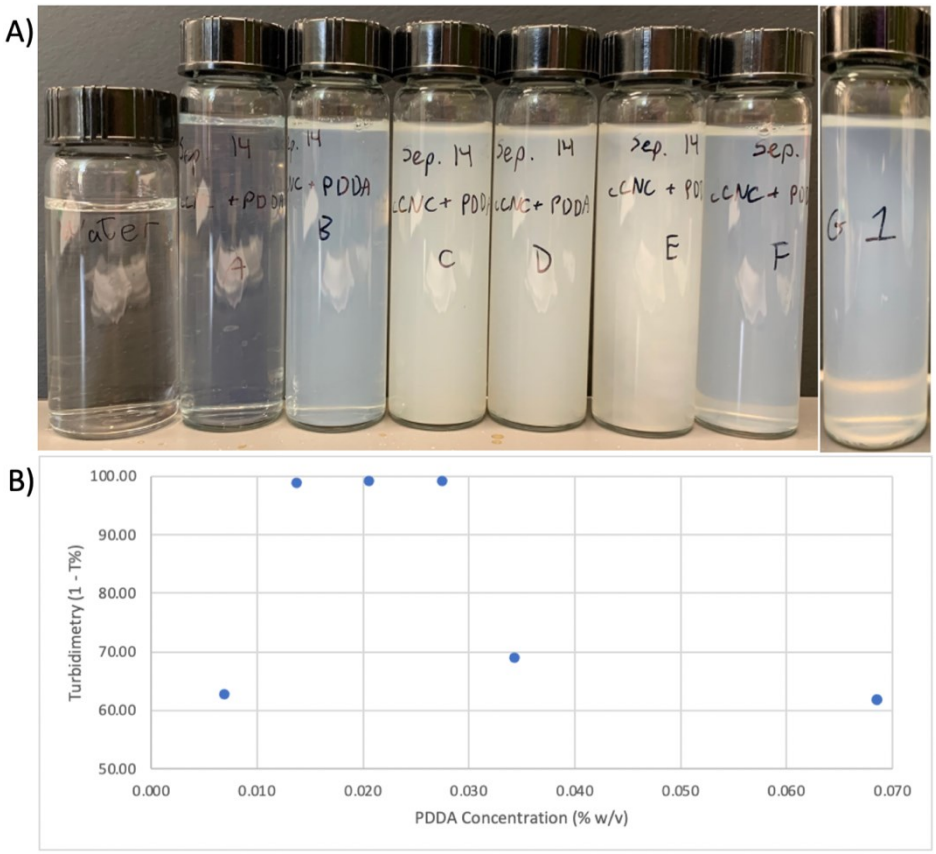

Figure 3.3: A) Images of cCNC and cCNC$^+$ samples with varying amounts of PDDA prepared using sonication. B) Plot of turbidimetry results for samples B – G

Evidently, some of the samples shown in Figure 3.3 are better dispersed when ultrasound was used to assist in the mixing of PDDA with cCNC. The reader is invited to compare the images in Figures 3.2 A and 3.3 A. For example, samples B, F, and G are less turbid (values between 60 and 70 %) compared with the same formulation (Figure 3.2 A) obtained by mixing with a stir bar. Sample B retains a negative zeta potential at -16.49. Samples F and G have the positive zeta potential > +60. Ultrasound clearly reduces the turbidity of these most positive cCNC$^+$ aqueous suspensions. The study shows not only that the mixing conditions are important, but also that one can obtain suspensions with the highest surface potential so that more dye molecules can be bound, whilst still avoiding significant agglomeration. Indeed, when making the pigmented particles in water, the cCNC$^+$ samples are more dilute, meaning that the samples are even less turbid – better dispersed. Another way to express this is as follows. The

turbidimetric study reveals that flocculation is greatest for PDDA concentrations lying between 0.01 - 0.03 % w/v when combined with a 0.49% w/v suspension of cCNC. Scaling these numbers upwards, a relative PDDA concentration in the range of 2 – 6 w% will cause unwanted $cCNC^{+}$ agglomeration. But one can exceed the PDDA concentration beyond than 6% relative to cCNC and still benefit from the excess positive potential whilst achieving dispersed particles (little or no agglomeration). This means that the PDDA concentration (0.069 % w/v, sample G2 above) used to make CNC pigment, when scaled to production levels for spray drying (i.e., to13.8 % PDDA relative to the amount of cCNC used), will still give well dispersed $cCNC^{+}$; hence the importance of the turbidimetric analysis.

3.3.3 Dye Molecule Molar Absorptivity Study

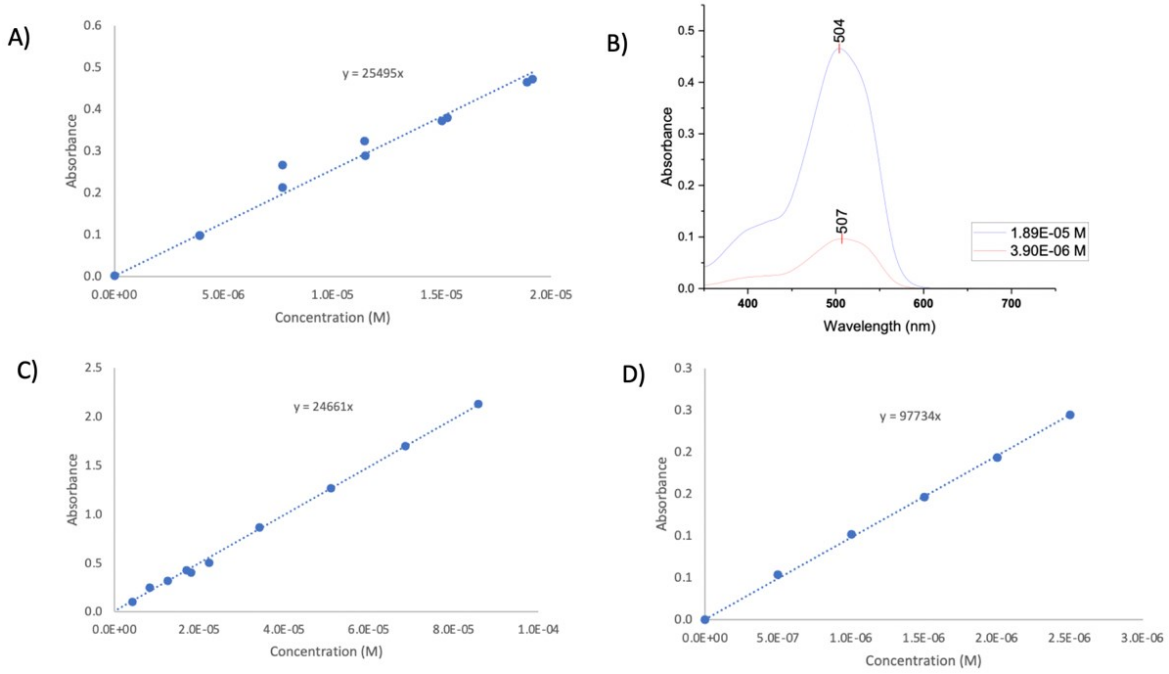

Figure 3.4: A) Red 40 dye Beer's law curve in water, B) Spectra of Red 40 dye at 2 different concentrations in water, C) Yellow 5 dye Beer's law plot in water, D) Blue 1 dye Beer's law plot in water.

Calibration curves were determined for the three individual dyes in water. Note that these dyes can exhibit solvatochromism, shifts in peak positions and absorption profiles that depend on solvent polarity (see below). From the curves, the molar absorptivity was determined by standard analytical dilutions from the slope of plots of absorbance versus concentration for each dye.

For Red 40, we obtained 25,495 M/cm. This is close to a reported value of 25,900 M/cm. [7] Spectra of red 40 dye are included in Figure 3.3 B to show the peak shape and positions. The main n→π* (nitrogen lone-pair-to-arene) peak is located around 504-507 nm. Vibronic coupling to high energy UV π, π* states (not shown here) introduces intensity into this otherwise forbidden transition.

For Blue 1, we obtained 97,734 M/cm. Reports of its extinction coefficient vary depending on the solvent. In water, the extinction coefficient has been reported to lie between 80,000- 93,000 M/cm. Let us look into Blue 1 in a little more detail. Chebotarev et al. [8] studied the acid-base and solvatochromic properties of the dye. They established that the molar absorptivity at 625 nm is 97,000 M/cm, which is close to the value we report. The molar absorptivity increases with increases in the relative dielectric permittivity of the solvent. Increasing the solvent polarity induces a hypsochromic (blue) shift in the dominant n→π* transition, an effect largely attributed to the stabilization of the ground state relative to the excited electronic state. Their analysis reveals several important equilibria. These are shown in the scheme below which is reproduced from their paper. A strong acid medium induces the formation of a protonated lactone (I). Dissociation of sulfo groups and benzyl fragments yields (II) and (III), respectively. One ammonium nitrogen atom is deprotonated in neutral or slightly alkaline media, yielding the tautomer (IV), with evident rupture of the lactone (III). Further increases in pH yield the new species (V). The electrically neutral form (III) dominates over the wide 0-8 pH range in water. We shall return to this when we discuss dye desorption from the pigment microbeads.

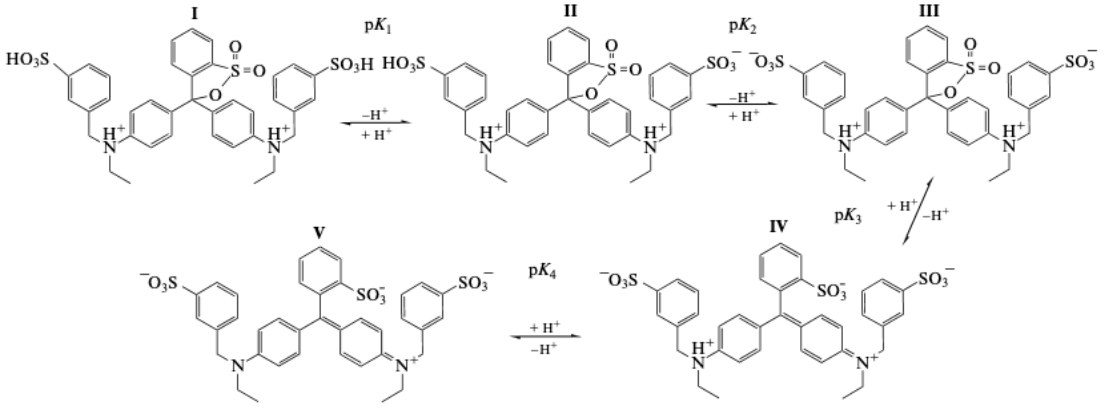

The authors point out that the tautomer equilibrium shown below depends strongly on solvent polarity, with the form (III′) dominating with increasing solvent polarity.

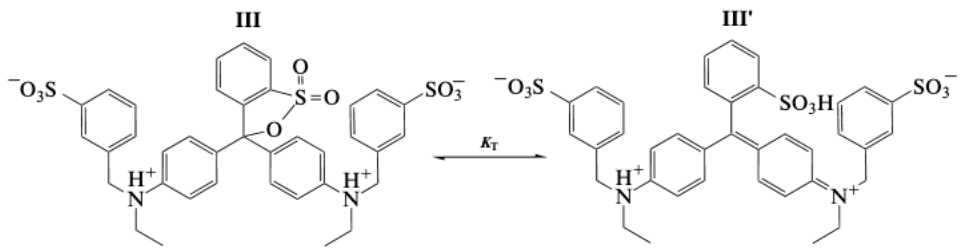

Figure 3.5: Tautomeric forms of the dominant structure of Blue 1 in water between pH 0-8. The constant K_T is the tautomer equilibrium constant. Tautomer shifts in favor of (III′) in polar media.

The absorptivity of yellow 5 was found to be 24,661 M/cm. Which is again close to the reported value of 27,300 M/cm. [7]

3.3.4 CNC Pigment Dye Leaching

The following study examined the leaching (desorption) of Red 40, Blue 1 and Yellow 5 dyes from the pigment particles. The study intended to answer the simple question, "Is the dye bound irreversibly to the cCNC nanocrystal PDDA polyelectrolyte complex comprising the microbead pigments when the microbeads are mixed with water, Salacos 222 oil (diisostearyl malate) or ethyl acetate?" As described in the experimental section, pigments were suspended for well-defined periods of time in these fluid media. The pigments were allowed to settle, and the supernatant was decanted and analyzed via spectrophotometry. The test results of the pigment in the diisostearyl malate (Salacos 222 oil) and ethyl acetate were negative, meaning by optical absorption there was no discernable leaching of dye from any CNC pigment compositions. The response of the CNC pigments to immersion in water was, however, markedly different. The results are presented next.

Figure 3.6 collects spectral scans of the aqueous supernatant resulting from exposure of CNC pigment (CNC) and Lake pigments to water at room temperature after 24 and 48 hours.

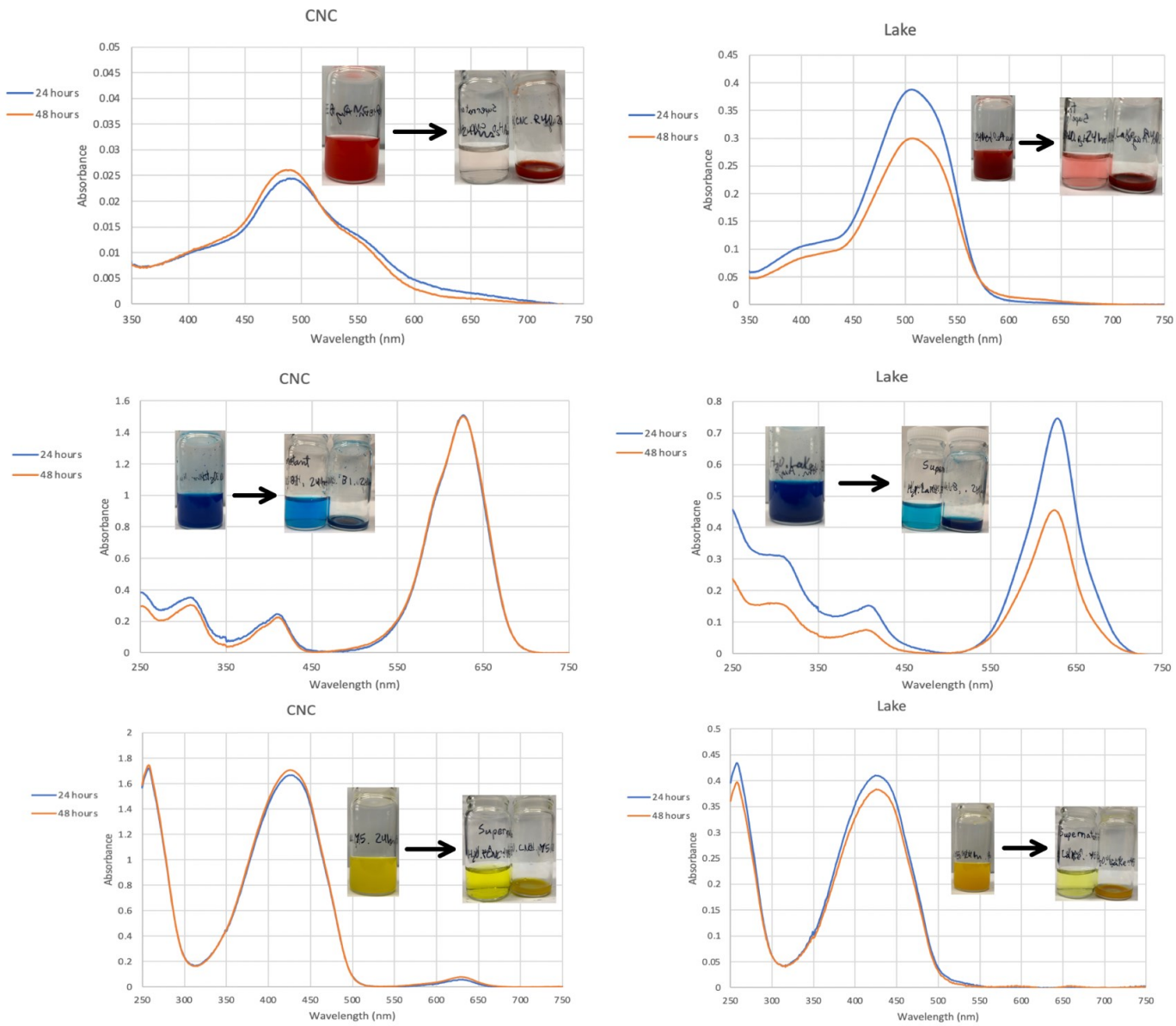

Figure 3.6: Spectral scans of the supernatant resulting from exposure of CNC pigment (CNC) and Lake pigments to water at room temperature after 24 and 48 hours. The left column collects the results of CNC microbeads in water. The right column records the outcome of exposing the corresponding Lakes to water. The image inserts show the samples immediately after mixing the pigment in water. The black arrow points to the supernatant (decanted) and the residue after 24 hours.

We begin with Allura Red 40. In water, there is significantly less leaching of the dye from its corresponding microbead pigment. This is evident from the absorbance measured after

24 and 48 hours when compared with the Lake pigment. The maximum absorbance change is less than 0.03 when the CNC microbeads are immersed in water. Note also that there appears to be a hypsochromic shift of the peak maximum from 504 nm (free dye in water Fig. 3.4 B) to ~ 485 nm when the dye desorbs from the CNC microbead. Moreover, the shape of the absorption spectrum differs markedly from the control shown in Figure 3.4 B. Note that we cannot assume that the absorption spectrum shown in the top left of Figure 3.6 is due to free Allura Red 40. It is possible that the dye is bound in a polyelectrolyte complex with PDDA (See later). By comparison, the Lake pigment appears to desorb free dye. Its spectral peak maximum and profile are unchanged from the control shown in Figure 3. 4 B. Apparently, Allura Red 40 is bound more strongly to the CNC than is the dye to its hydrous alumina substrate in the Lake pigment. The story differs when we examine the binding and release of Blue 1 and Yellow 5.

We turn our attention first to Blue 1 bound to CNC^+ versus the Lake. The data are visible in the middle images of Figure 3.6. We focus on the major band centered at 625 nm in the CNC microbead complex. After 24 h, the absorbance maximum in the water supernatant reaches 1.5 for the CNC pigment and 0.45 for the Lake. After 48 h, there is no change in the absorbance from the supernatant originating from the CNC pigment. This suggests a kind of "burst kinetics" where dye located at the surface and near subsurface regions departs the surface early after exposure to water. By comparison, the Lake pigment evolves color that increases from 0.45 to 0.74 absorbance units. We conjecture that dye, if bound to PDDA, leaves the surface of the microbead together with PDDA if they are weakly bound or physisorbed. The PDDA/dye which leaves the surface remains attached during the sample preparation. Otherwise, Blue 1 is so strongly bound to PDDA, which in turn is bound to the CNC matrix, that the PDDA/Dye PEC cannot desorb from the CNC pigment particle. Dye bound to the Lake construct is not subject to the same constraints.

Like Blue 1, the Yellow 5 CNC pigment microbeads desorb dye (as a PDDA complex?) in a "burst" with no change in the absorbance between 24 and 48 h. The Lake appears to desorb 4 times less dye than the CNC pigment particle. Nevertheless, the Lake shows continual dye desorption, though it is less than what is observed for the Blue 1 system. Note that the peak maxima and absorbance profiles for Blue 1 and Yellow 5 on CNC or hydrous alumina are similar. This state contrasts with that of Allura Red 40. The implication is that the way Allura

Red 40 binds to PDDA, and perhaps also to cCNC, differs from how Blue 1 and Yellow 5 bind. Due to the similar structures for the dyes, the reason for the difference is not known.

Interestingly there is evidence in Figure 3.7 from TEM that the coloration of the Red 40 Lake supernatant might not only be due to free dye, but also due to dye bound to hydrous alumina nanoparticles.

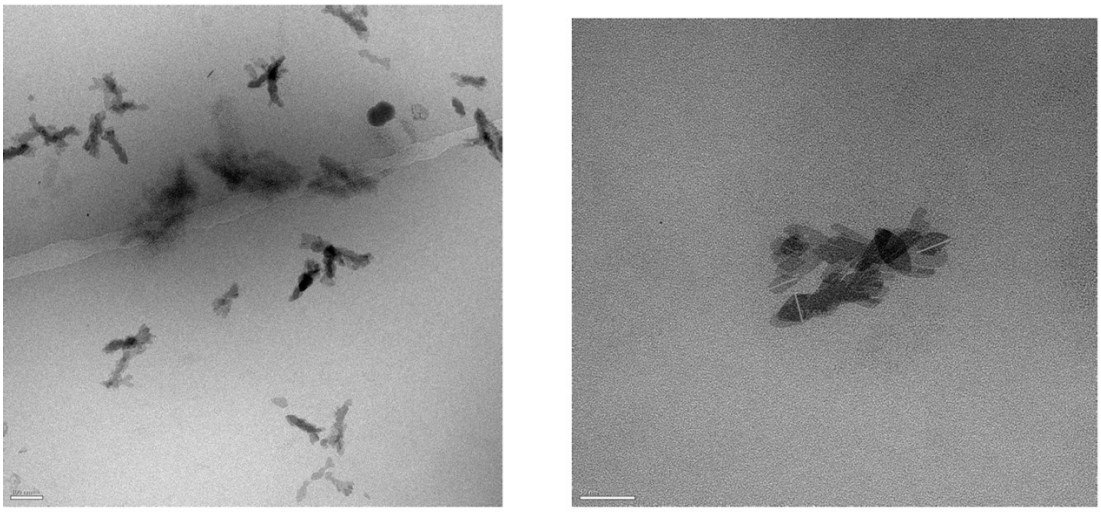

Figure 3.7: TEM images of Red 40 Lake pigment nanoparticles collected from the water supernatant after 24 hours of leaching.

Next, we describe the leaching results for pigments prepared by molecular mixing on $cCNC^+$ as well as naturally derived green sodium copper chlorophyllin CNC pigment. Images of the supernatant solutions are assembled in Figure 3.8. In order from left to right, these are green copper chlorophyllin CNC pigment, purple based on 1:1 mixing of $cCNC^+$ with Red 40 and Blue 1, a green microbead pigment prepared by combining Blue 1 and Yellow 5 dyes in a 1:1 ratio on $cCNC^+$, and orange pigments prepared by molecular mixing of Red 40 and Yellow 5 in either a 1:1 or 1.7:1 ratio. The green copper chlorophyllin pigment does release some dye, evidenced by the green tint of the supernatant, and it has a maximum absorbance of 1.06. The purple pigment releases blue dye almost exclusively. The quantity is again small but notably the Red 40 dye component remained strongly bound. This is why the purple pigment yields a teal blue colored supernatant. Not surprisingly, the green microbeads prepared from 1:1 Blue 1 and Yellow 5 yield a pale green supernatant since both dyes are released from the microbead. Yellow dye is the dominant agent released from the orange pigments which also contain Red 40. These are shown in the last two on the right-hand side of the images.

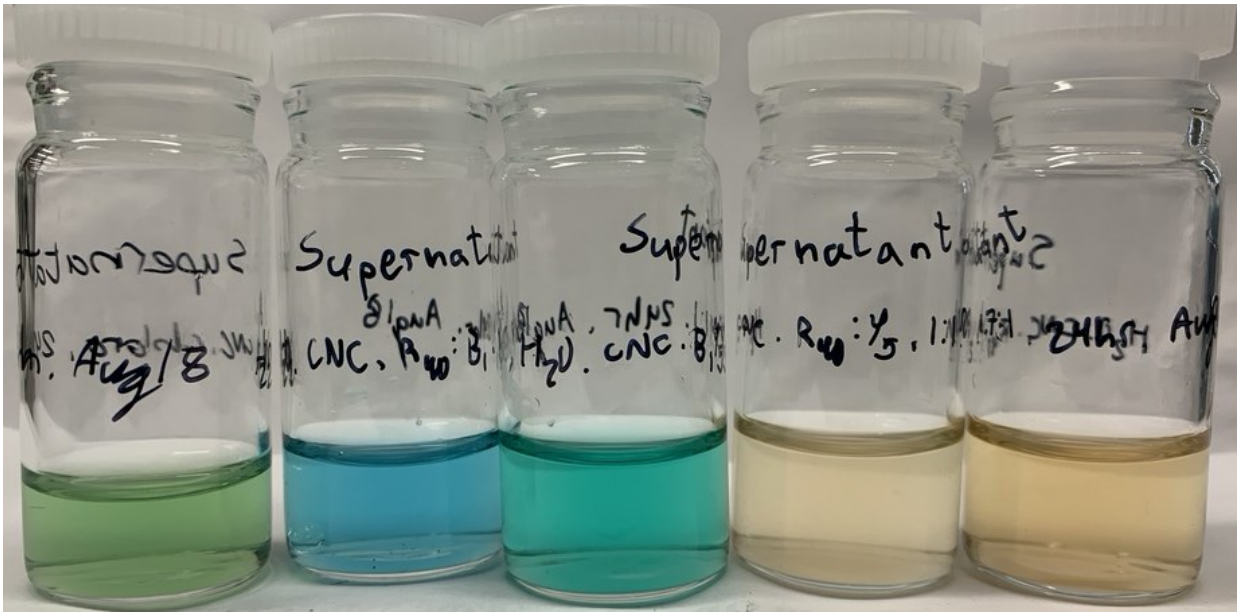

Figure 3.8: Images of dye leaching into water supernatant decanted from pigments after 24 hours. (Left to right) Copper chlorophyllin (natural green), 1:1 B1 and R40 (purple), 1:1 B1 and Y5 (green), 1:1 R40 and Y5 (orange 1), 1.7:1 R40 and Y5 (orange 2).

These leaching studies are consistent with what is known about dying cotton, microcrystalline cellulose, and other cellulose fibers with what are called "direct dyes". [9] Direct dyes are water-soluble dyes applied by a one-bath process without the use of mordants. Their mode of binding relies largely on hydrogen bonding and van der Waals interactions with the crystalline and amorphous regions of the cellulose. The rate of dying and yield are enhanced by adding salts like NaCl and Na_2SO_4 to the water medium. The cations screen the negative charge on the fibers, resulting in improved H-bonding and van der Waals interactions with negatively charged dyes. Nevertheless, the dye-to–fiber cellulose bond is unstable, and the wet-fastness properties (resistance to leaching) are known to be poor. In our studies, we replace the salt with PDDA, and meticulously "titrate" the surface of cCNC with positive charge to create an electropositive PEC environment through the PDDA. The PEC is the entity that binds anionic dyes largely by electrostatic interaction. Red 40, Blue 1 and Yellow 5 contain sulfonate anion moieties that provide the negative charge. Yellow 5 is also equipped with a carboxylate anion. The structures of these dyes are given in Chapter 2. The common sulfonate feature cannot alone account for the stronger binding of Allura Red 40 to the nanocellulose microbeads. For clues about the differences, we turn to examining the binding of the respective dyes to $cCNC^+$. These studies are described next.

3.3.5 cCNC$^+$ Dye Binding Interactions

Dye molecules have often been used to determine concentrations of cationic polyelectrolytes in water. PDDA is no exception. For example, Maldonado et al. titrated PDDA with toluidine blue O (OTB). [10] The maximum absorbance of free OTB undergoes a hypsochromic shift from 628 to 520 nm when the PDDA/dye PEC forms. Similarly, PDDA in water has been quantified by titration with acridine orange. [11] A hypsochromic shift in the peak absorbance of the free dye is observed as the PEC-dye interaction forms. The implication of these prior studies is that we might anticipate that the formation of the cCNC$^+$ PEC with the anionic red, blue and yellow dyes is likely to be accompanied by the evolution of new bands, perhaps to the blue of the free ion absorption maximum. This is indeed what we find.

Dye binding interactions were examined by adding increasing aliquots of dye to suspensions to cCNC$^+$. The concentration of cCNC$^+$ was 0.5 wt. % and the PDDA concentration relative to the cCNC$^+$ was 14%. Figure 3.9 shows how the absorbance profiles

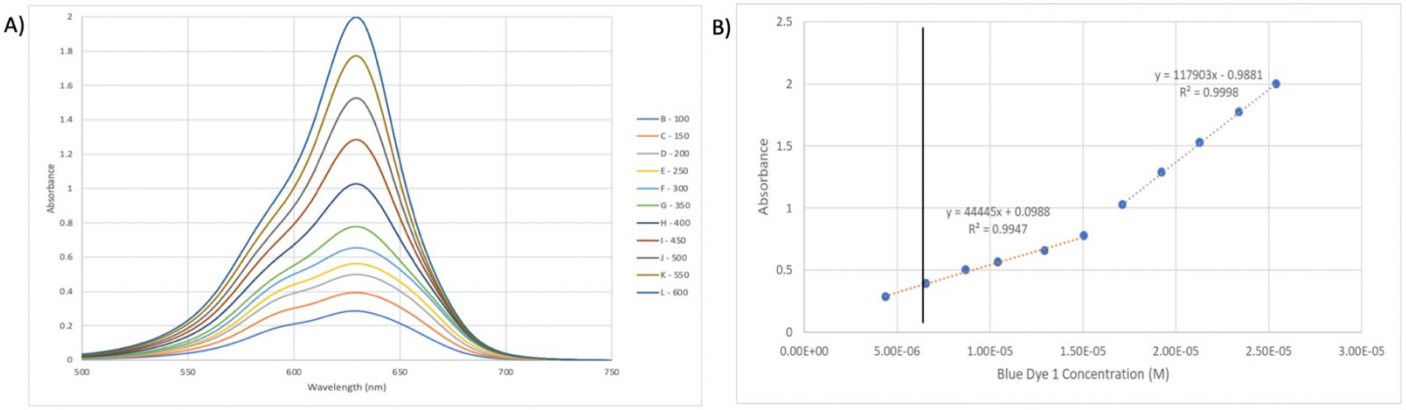

Figure 3.9: A) Changes in electronic absorption spectra of cCNC$^+$ solutions with increasing quantities of added Blue 1 dye. B) Plots of the maximum absorbance as a function of the concentration of dye added to the sample. The vertical black line represents the concentration of Blue 1 used to make Blue 1 CNC pigment.

of Blue 1 interacting with cCNC$^+$ change with increasing loading of Blue 1 on the PDDA-bound nanocrystals. In Figure 3.9 A, note how the peak centered near 630 nm gradually increases in intensity with increasing additions of dye. A shoulder is observed near 595 nm. Not shown is a peak near 410 nm that can be attributed to a prototropic equilibrium in water. [8] The legend to the right of the absorbance curves indicates the sample label B-L, and the given aliquot volume (in

μL) of the stock Blue 1 solution added. In Figure 3.9 B we plot the absorbance against the Blue 1 dye concentration. The plot shows an inflection point near 1.5 x 10^{-5} M added dye. Two linear regimes are evident. The first regime at low concentration has a slope of 44,400 and the second a slope of 117,900. The first slope correlates with the binding of dye to the $cCNC^{+}$ PEC complex through PDDA. This type of binding apparently causes a hypsochromic shift in the n→π* 630 nm transition which shows up as the shoulder near 595 nm. In the absence of $cCNC^{+}$ there is no shoulder on the main band, reinforcing the notion that the 595 peak is due to a dye PEC complex. The main peak is at 630 nm and belongs to the free Blue 1 dye. The molar extinction of free dye in this case is higher than what we measure for free dye in water alone. Initially, with increasing dye concentration, both the shoulder and the main peak increase together. It is not clear if there is an equilibrium between dye in the PEC and free dye in solution in this first regime. By sample H (7^{th}) and other higher dye concentrations, the increase in the free dye contribution to absorbance exceeds that of the 595 nm absorbance. This suggests that the PDDA has become fully titrated by the negatively charged dye, i.e., that the $cCNC^{+}$ complex is fully loaded with dye. The region to the right of the vertical black line in Figure 3.9 B suggests that there is a capacity for $cCNC^{+}$ to take up dye to 1.5 x 10^{-5} M before the dye is no longer able to bind.

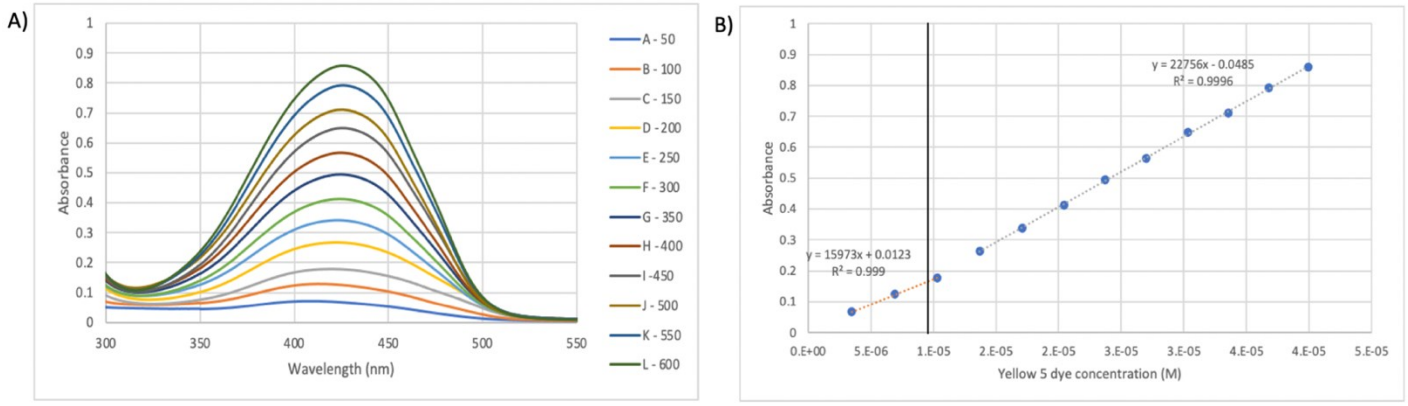

Figure 3.10: A) UV-Vis spectra of $cCNC^{+}$ solutions with increasing quantities of Yellow 5 dye. B) Plot of the maximum absorbance as a function of the concentration of each sample. The black line represents the current concentration used to make yellow CNC pigment.

The evolution in the absorbance with increasing concentrations of Yellow 5 dye is shown in Figure 3.10 A. In this case, we also observe a partitioning between dye bound to the PEC and free dye in water. While difficult to discern in the Figure, in the early stages of dye binding there is again a hypsochromic shift in the absorption maximum of Yellow 5 dye to 425 nm. The first

three aliquots of Yellow 5 dye yield bound dye complex. Beyond aliquot C the absorption spectrum appears to be dominated by free dye. The molar absorptivity in the early low dye concentration regime is ~ 16,000. The added "free" dye exhibits a molar absorptivity of 22,750 which is much closer to what we measure for the free dye in water without cCNC or PDDA. Again, the vertical black line locates the concentration of dye actually used to prepare the pigment microbeads. There is a capacity for the cCNC+ to add dye up to about 1.75 x 10^{-5} M.

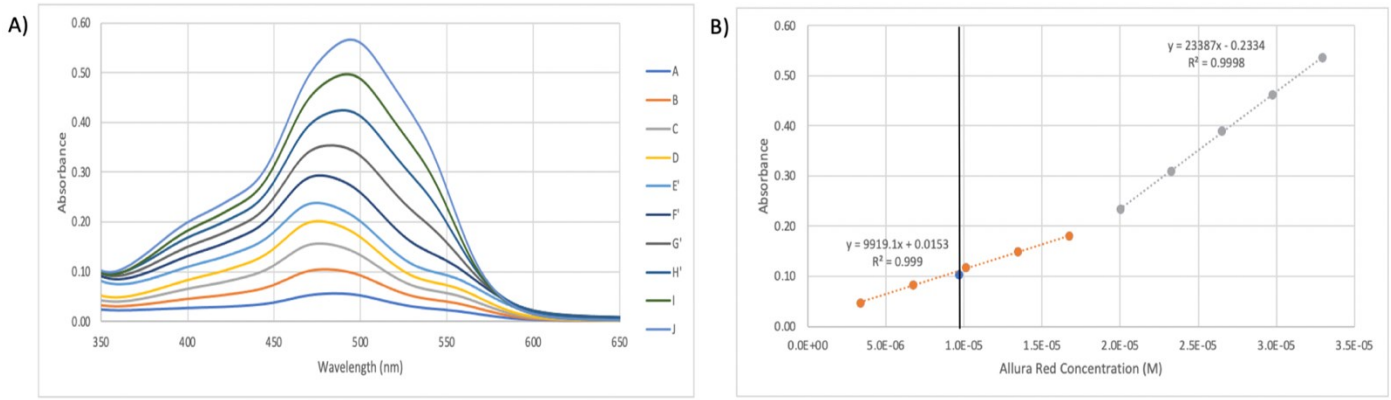

Figure 3.11: A) UV-Vis Spectra of cCNC^{+} solutions with increasing quantities of Red 40 dye. B) Plot of the maximum absorbance as a function of the concentration of each sample. The black line & blue dot represents the current concentration used to make yellow CNC pigment.

Free Red 40 dye in water exhibits an absorption maximum at ~ 504 nm. Additions of Red 40 dye to the PEC produce a band that we attribute to dye binding to the cCNC^{+} complex. The peak maximum is located near 480 nm. With increases in Red 40 dye to the suspension, we observe the "free" dye peak absorbance to evolve near 490 nm. This represents a shift of ~ 14 nm from the free dye in water in the absence of the PEC. The first is a blue shift to 480 nm in absorption that is obviously caused by bound Red 40 dye. The peak absorbance wavelength remains unchanged for the first five dye aliquots, A to E. From aliquot F onward, there is a red shift in the peak maximum, ostensibly originating in unbound dye. The affinity of Red 40 for the PEC is evident in the absorption profile of sample E from Figure 3.11 A. The peak absorbance is significantly larger for the bound dye than the peak for the free dye. Comparing the data with that for Blue 1 and Yellow 5, perhaps the clue to the resistance of Red 40 to leaching lies in the stronger complex formed between Red 40 dye and cCNC^{+}. Turning to Figure 3.11 B the slope for "free" dye yields a molar absorptivity of 23,400 M-cm^{-1}, which is close to what we measure (25,945 M-cm^{-1}) for the free dye in water. The early-stage regime yields an absorptivity of 9900

$M\text{-}cm^{-1}$. The vertical black line in Figure 3.11 B represents the concentration which is currently used to make the Red 40 CNC pigment. Its location indicates that one can increase the concentration of the Red 40 dye to saturate binding to PDDA. Accordingly, we conducted experiments to test the idea that the plot of bound versus free dye might be used to enhance the loading of Red 40 on the nanocrystals and therefore increase both saturation and coverage. These experiments are described next.

3.3.6 Increasing R40 Loading in CNC Pigment

Having expanded the range over which the Red 40 dye can be loaded onto the $cCNC^{+}$ polyelectrolyte complex, we are in a position to test how the additional dye content on the nanocrystals affects the reflectance values, coverage and saturation. For these experiments, a concentration of 16% Red 40 dye relative to the CNC will be used. In Figure 3.11 B this would be located slightly to the right of the fourth point on the slope and is still well before the final point before the increase in slope. This increase means that there is x1.6 red dye in the new loading, as the initial concentration was 10% relative to the CNC. Table 3.3 compares the L*a*b parameters for Red 40 pigment prepared in the standard manner to that with enhanced dye content.

Table 3.3: Reflectance values for the original red CNC pigment and the red CNC pigment with an increased amount of red dye.

Sample Red 40	**L***	**a***	**b***	**ΔE***
Standard preparation	57.38	29.71	13.61	1.11
Increased dye content	56.56	30.43	13.79	

It is gratifying that the reflectance values are unchanged within experimental error. There is no significant difference between the two samples for any of the individual L*, a*, and b values. The delta E of 1.1 lies inside the range where the human eye cannot discern a color difference. This is testimony to the robustness of the preparation and to the strategy we have developed to increase the dye loading without compromising the state of dispersion of the PEC. In Table 3.4 we compare saturation values for the Lake pigment with those of the CNC microbead pigment with enhanced dye loading. As described in section 2.2.3, we dispersed the pigments in Salacos 222 oil (diisostearyl malate).

Table 3.4: Saturation values for red CNC & lake pigments.

Concentration of pigment in oil (wt. %)	CNC - 16 wt% Saturation	Lake adjusted - 16 wt% Saturation	Lake - 40 wt% Saturation
1	19.96	15.47	24.06
2	23.12	19.03	26.23
3	28.17	20.38	28.17
4	29.40	23.31	31.04

The saturation values for the CNC red pigment were obtained along with those for the Red 40 Lake. For the latter, additional measurements were completed by adjusting the amount of pigment used so that the amount of dye added to the formulation equalled the amount of dye brought to the formulation by the CNC microbead pigment. In Table 3.4, this adjustment is the column labelled "Lake adjusted - 16 wt% Saturation". Otherwise, the lake is formulated at a loading of 40 wt% dye content (last column on the right). The left-hand column indicates the wt% pigment loading in the Salacos 222. The column labelled "CNC - 16 wt% Saturation" corresponds to the "increased dye content" sample of Table 3.1. Examining Table 3.4 we see that the Red 40 Lake formulated with 40 % dye in the pigment, shows the highest saturation. When the Lake pigment is adjusted to have the same dye content as the CNC pigment, the latter outperforms the Lake for every concentration of pigment in the oil. It still has slightly lower saturation values for some amounts, especially when there is only 1% dye in the oil.

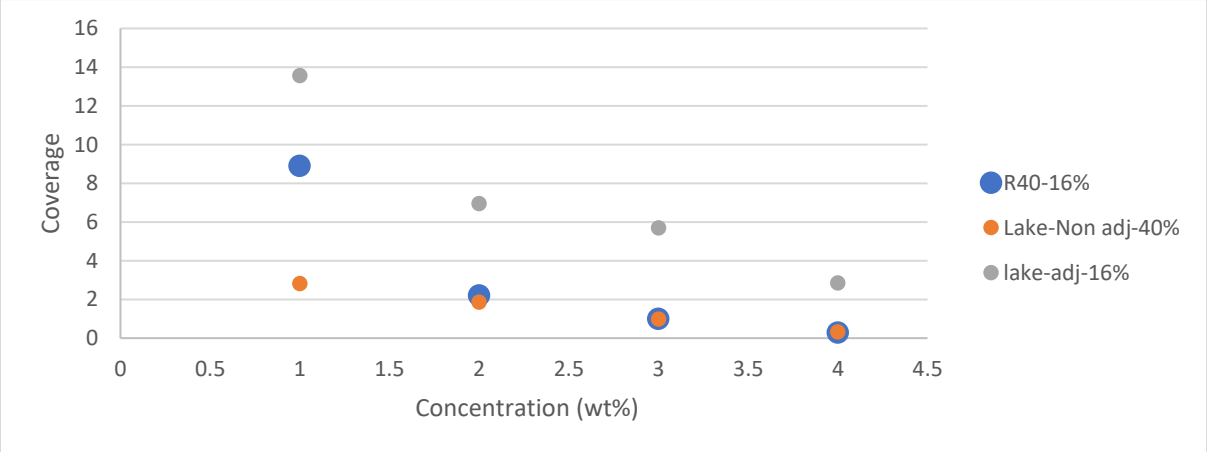

Figure 3.12: Coverage values for different concentrations of red 40 CNC pigment with 16% loading, red lake, and red lake with concentration adjusted to be for the dye, not the pigment.

The results for coverage are plotted in Figure 3.12. The smaller the ordinate number, the higher the coverage. At 1 w% loading of Lake pigment (not adjusted for dye content), the coverage is superior to the CNC pigment and the Lake adjusted for dye content to match that of the CNC pigment. At 2, 3 and 4 w% pigment, the increased dye content CNC pigment matches that of the Red 40 Lake, despite the larger dye content in the latter. The Red 40 Lake which was adjusted to match the dye content of the CNC pigment exhibits inferior coverage. Overall, the use of the plot to guide the selection of quantities of dye binding to the CNC^+ PEC (Figure 3.10B) in the absence of free dye, significantly improves both the saturation and coverage.

We next examined the impact of increasing the Red 40 dye loading on the CNC^+ particles. The changes in nominally "free" dye content after exposing the CNC Red 40 pigment with enhanced dye loading are shown in the absorption spectra in Figure 3.13. The absorption maximum occurs near 504 nm. Note that this absorption profile is identical to that of free Red 40 dye in water (compare Figure 3.4 B), and not at all like that of the supernatant in Figure 3.6 (top left spectrum). This finding strongly suggests that what little dye is released to water from the pigment with enhanced Red 40 loading is not bound to PDDA. The absorbance change is constant within experimental error.

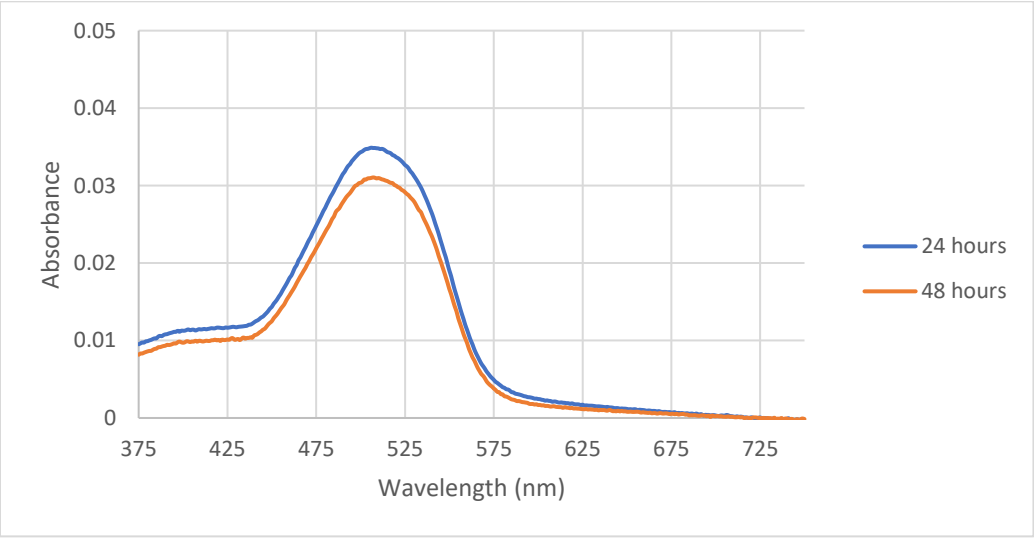

Figure 3.13: Absorption spectra of Red 40 supernatant derived from 24 and 48 h desorption study from Red 40 pigment with enhanced dye loading.

For the Red 40 pigment with enhanced dye loading, we conclude that saturation and coverage are improved, with no significant increase in leaching.

3.4 Conclusions

Polyelectrolyte complexes between anionic cCNC and polycationic PDDA to yield CNC^+ were examined as functions of PDDA concentration via concentration-dependent zeta potential, turbidimetry, and electronic absorption. At a concentration, of 2% w/w PDDA/cCNC, the surface charge changed from negative to neutral, leading to flocculation. Turbidimetric studies determined concentration conditions that reduced flocculation. These conditions were used to encourage the binding of cCNC+ with various anionic dyes. Ultrasonic mixing was found to limit flocculation when the concentration of PDDA was high. Lowest turbidity was exhibited by samples that were negatively charged (sample B at -16.49 mV) and by samples with high positive potential (samples F and G at > + 60 mV). The large excess of positive charge on $cCNC^+$ will bind the largest quantity of anionic dye. This was established by titrating 0.5 wt. % $cCNC^+$ where the PDDA concentration relative to the $cCNC^+$ was 14%. Beer's law plots in this potential regime were linear until a break point and change in slope in plots of absorbance versus dye concentration indicated that the $cCNC^+$ binding sites had become saturated. Beyond the break point, the linear Beer's law plot yielded molar extinction coefficients identical to those of free dye in water. With knowledge gathered from these studies, a 14% w/w PDDA/cCNC concentration is recommended to invert the charge from (-) to (+) to make a host nanocrystal platform, CNC^+, that is likely to bind the most dye. Red 40, Blue 1 and Yellow 5 dyes show hypsochromic shifts when binding to cCNC+. Dye desorption studies revealed that Red 40 CNC pigment resists desorption, whereas Blue 1 and Yellow 5 pigments release some dye. In some cases, dye might desorb as a soluble PDDA-dye polyelectrolyte complex. Evidence for this was based on observed hypsochromic shifts in absorption bands in the supernatant that was isolated following time dependent dye desorption. By TEM it was found that the Lake pigments can also release dye pigment hydrous alumina nanoparticles in the supernatant. Leaching from the mixed dye CNC pigments confirmed that the yellow and blue components are preferentially released, leaving Red 40 dye strongly bound to the microbead.

Among the three types of dye, Red 40 dye is most strongly bound to $cCNC^+$. Loading more Red 40 dye onto $cCNC^+$ up to the break point where free dye can no longer bind was used to raise the dye content in the CNC-based pigment microbead. The method was used to increase the Red 40 dye content in the CNC microbeads such that the saturation and coverage values were

competitive with those of the corresponding Red 40 Lake pigment. The CNC microbead Red 40 pigment showed no significant increase in leaching at higher Red 40 loadings.

3.5 References

1. Wikimedia Commons Diagram of zeta potential and slipping plane. https://commons.wikimedia.org/wiki/File:Diagram_of_zeta_potential_and_slipping_planeV2.svg.
2. Clogston, J. D.; Patri, A. K., Zeta potential measurement. *Characterization of nanoparticles intended for drug delivery* **2011**, 63-70.
3. Zhou, Y.; Fu, S.; Zheng, L.; Zhan, H., Effect of nanocellulose isolation techniques on the formation of reinforced poly (vinyl alcohol) nanocomposite films. *Express Polymer Letters* **2012,** *6* (10).
4. Ullman, E. F., Homogeneous immunoassays. In *The immunoassay handbook*, Elsevier: 2013; pp 67-87.
5. Kolev, S. D.; McKelvie, I. D., Advances in flow injection analysis and related techniques. **2008**.
6. Morse, T. Nanocrystalline Cellulose: Surface Chemical Transformation and Applications. McGill University, 2015.
7. Thermo Fisher Scientific Food Dyes and Beer's Law. https://assets.thermofisher.com/TFS-Assets/MSD/Scientific-Resources/FL53099-food-dyes-beers-law-qc-lesson-plan.pdf (accessed May 21).
8. Chebotarev, A.; Bevziuk, K.; Snigur, D.; Bazel, Y. R., The brilliant blue FCF ion-molecular forms in solutions according to the spectrophotometry data. *Russian Journal of Physical Chemistry A* **2017,** *91*, 1907-1912.
9. Clark, M., *Handbook of Textile and Industrial Dyeing: Volume 2: Applications of Dyes*. Elsevier: 2011.
10. Maldonado, E. A. L.; Terán, A. O.; Guzmán, M. T., A multiparameter colloidal titrations for the determination of cationic polyelectrolytes. **2012**.
11. Ziółkowska, D.; Szeflińska, I.; Shyichuk, A., Quantitation of poly (diallyldimethylammonium chloride) by complexation with acid orange 7 dye. *Polimery* **2014,** *59* (11-12), 859-861.

Chapter 4- Hyperspectral Imaging of CNC-Based Pigments

4.1 Introduction

To this point in the thesis, we have used zeta potential analysis, turbidimetry, electronic absorption and reflectance spectroscopy in combination with electron microscopy to characterize cCNC-PDDA polyelectrolyte complexes, pigment colour properties, and dye desorption from CNC pigment microbeads. This chapter describes our use, and outcomes, of hyperspectral imaging (HSI) to examine the distributions of dye molecules on the surface of the pigment microbeads and thus to provide additional insight into the dye release process (leaching) when the microbeads are hosted in water.

Hyperspectral imaging was developed in the early 1970s. Since then, HSI has been implemented for chemical detection, geology, mining, environmental monitoring, surveillance, and agriculture. HSI is a diffuse reflectance non-destructive imaging technique that uses a pixelated sensor (camera imaging spectrometer) to collect a continuous spectrum of wavelengths of light from a large number of images over the same spatial area.[1] The front-end optics of the instrument focuses images of the target area of a sample onto a slit whose role is to pass light from a narrow line in the area under view. The light is collimated, and then a dispersive element (i.e., a transmission grating) separates the different wavelengths. The dispersed light is then focused onto a pixelated 2-dimensional detector array. Thus, for each pixel interval (a slice) along the line defined by the slit, a corresponding spectrum is projected on a column of detector pixels on the array. Thus, by scanning over the target, the camera collects slices from adjacent lines defined by the slit. The data are then read out from the detector array. The data comprise a slice of a hyperspectral image, with spectral (λ) information in one direction and 2D spatial ((x, y), image) information in the other for each pixel. In this way, the instrument produces a hyperspectral data "cube" (a hypercube) as in Figure 4.1 B. Data cubes are acquired either by scanning techniques such as push-broom sensors or snapshot technology for non-scanning spectral cameras (spectrographs), the latter meaning that the complete data cube is gathered with one sensor readout. Improvements in HSI technology now allow the collection of data on the nano-scale.[2] HSI can be performed using both dark-field and bright-field optical imaging modes.[3-6] HSI generates a data set which is much more complete when compared to other imaging techniques.[2] Below, we discuss hardware and software components of the *Photon etc* HSI system used in the current study.

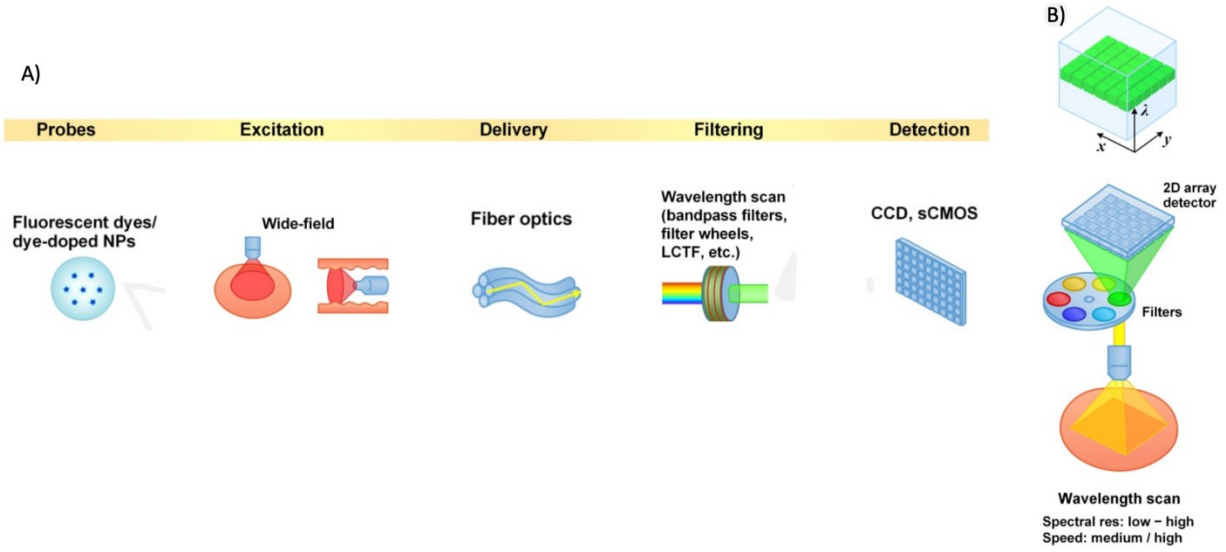

Figure 4.1: A) Schematic of optical imaging approach for the HSI instrument used. B) HSI as a wavelength scan with optical filtering.[7]

Light in the spectral region of interest is provided by a supercontinuum laser with "wide-field imaging". This configuration allows a large spatial region to be excited. The light transmitted through the sample is then detected using a camera gated by spectral filters (see Figure 4.1 B) and discussion below). This approach is faster than one requiring mechanical scanning. Light admitted by the slit is dispersed over the CMOS sensor array at a fixed exposure time. In this mode the HSI camera detects spectral and spatial information over millions of (spatial) pixels. The image cube is obtained by acquiring two-dimensional images at multiple wavelength channels over time. This is shown in Figure 4.1 B as a wavelength scan. This method can achieve high spectral resolution with tunable filters, though the main drawback to the hardware configuration is its lengthy imaging time compared to the snapshot method.[7]

4.2 Experimental

4.2.1 Setting up Hyperspectral Imaging

Our study used a *Photon etc* IMA Dark visible and near-infrared Hyperspectral Imaging System shown in Figure 4.2 below. The system comprises components that are assembled into the final HSI spectrograph. Excitation was provided by a NKT Photonics SuperK FIANIUM FIU-15 supercontinuum laser. These are followed by a Fiber Mode Shaker Controller, Laser Line Tunable Filter, and a Motorized Focus. The CCD chip intelligence is based on a

Hamamatsu ORCA-Flash4.0 V3 sCMOS Camera with an ASI motorized stage controller. A Nikon ECLIPSE Ti2-U Inverted Microscope is incorporated to assist in imaging and recording the location of pigment microbeads. Fiber optic cables were used to connect the laser, fiber mode shaker controller, and the tunable filter.

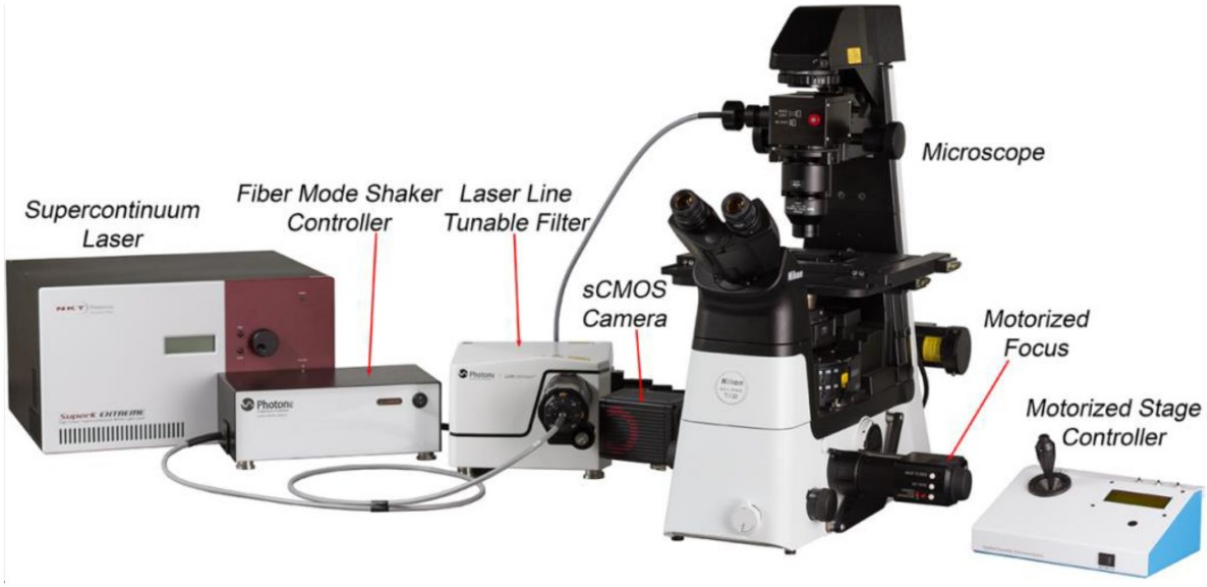

Figure 4.2: An image of the Photon etc IMA Dark HSI with components labelled.[8]

A sample of CNC pigment microbeads was dispersed by drop-casting pigment microbeads from water onto a 25mm X 25mm glass microscope slide. The sample slide was then placed in a holder fabricated by 3D-printing to accommodate different sizes of glass sample substrates.

A hyperspectral data cube was obtained by acquiring images and transmittance information over a wavelength range 425 to 750 nm with a 5 nm step size between any two images.

4.2.2 Hyperspectral Imaging Analysis

Hyperspectral imaging of individual pigments was used to map the distribution of dyes on the microbeads. To do this, image cubes were first obtained of the CNC pigment containing only one dye, either Red 40, Blue 1, or Yellow 5. The cubes were then obtained for pigments hosting two dyes: Purple (Blue 1 + Red 40), Orange (red 40 + yellow 5), and Green (Blue 1 + Yellow 5). Multiple cubes were obtained from each sample to analyze different microbeads. The

analysis was done with many microbeads over multiple different cubes to ensure accuracy. Due to the large file only one cube was obtained for each microbead.

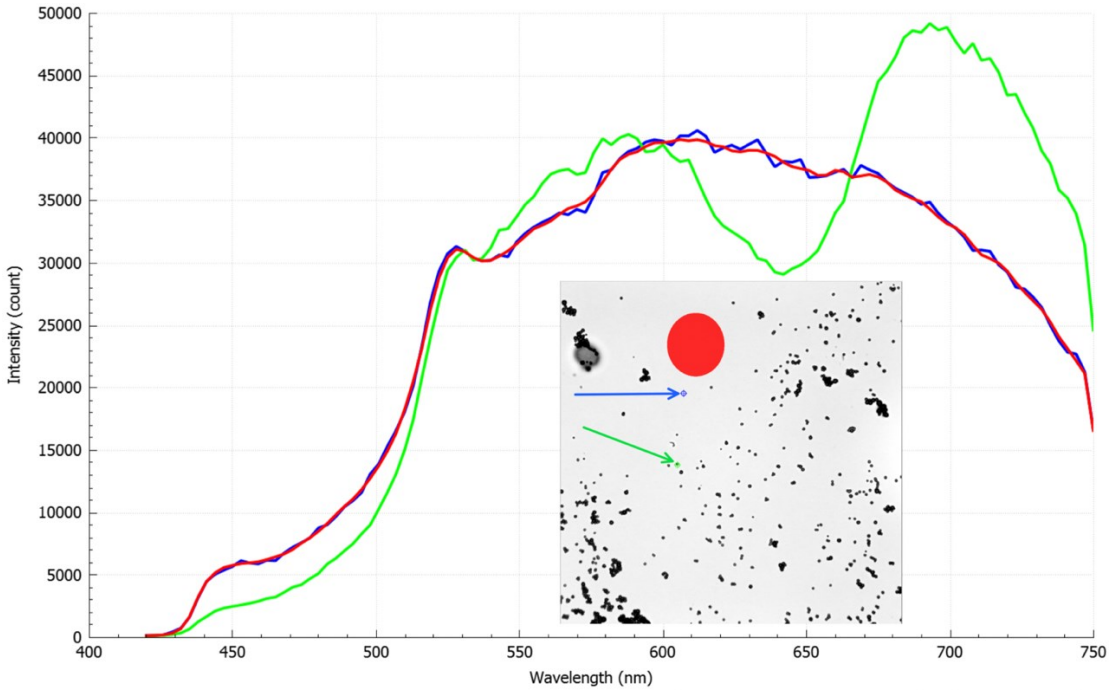

Figure 4.3: Transmittance plot of the background average [red curve] (average of all the pixels in the red circle of the image), the transmittance plot of an individual background pixel [blue curve] (endpoint of the blue arrow in the image), the transmittance plot of a pixel in a green microbead which is not background-corrected [green curve]. The green arrow points to the green microbead.

To illustrate, we provide an example of how one analyzes a green pigment microbead. The pigment particles were produced by combining 1:1 Yellow 5: Blue 1 dye molecules on the cCNC^{+} nanocrystals. Background corrections must first be made by measuring the transmittance in regions where there are no green pigment microbeads. In Figure 4.3, this region is represented by the filled red circle. (The black dots in the image insert are green pigment microbeads viewed at low magnification.) The average transmittance of the background at each wavelength for all the pixels in the array was then plotted. This plot is shown in Figure 4.3 above in red. Next, we obtained the transmittance recorded for each pixel in the data cube acquired by wavelength- and (x,y)-scanning of a single microbead. The location of the microbead is indicated at the tip of the magenta arrow in the microscope image insert. The resulting transmittance was divided by the average background plot. The background-corrected equivalent of Figure 4.3 is shown below in Figure 4.4.

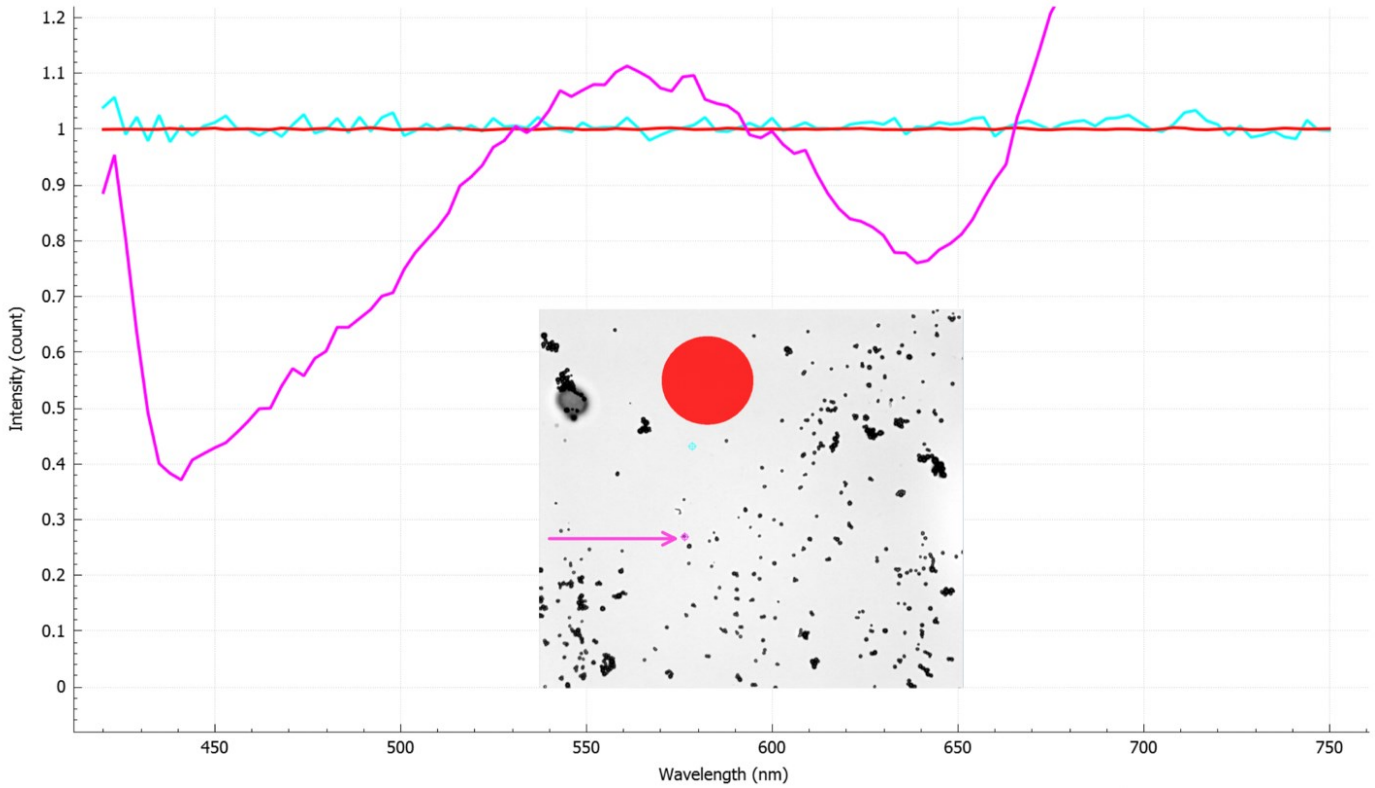

Figure 4.4: Background corrected transmittance plot of background average (red), background pixel (cyan), and green microbead pixel (magenta curve). The magenta arrow points to the location of the green microbead pigment particle.

Because the green microbead was obtained from nanocrystals nominally decorated by 1:1 yellow:blue dye molecules, we are interested both in the average dye distribution that produces the green hue and how the blue and yellow dyes might be distributed over the surface of the microbead. In short, we ask if we can determine how close to the 1:1 ratio is the dye binding to the CNC^{+} that comprises the microbead. Obviously, the data set is enormous, given the number of microbeads and the magnitude of the data sets for each. To map the location of dyes on the microbeads of the pigments three types of spectral acquisitions were obtained. The reader is directed to Figure 4.5. The grayscale image insert at the top left of the Figure shows an aerial view of the pigment microbead particles on the plane of the microscope slide. The small red circle in this image locates the microbead of interest. The image of the microbead is expanded in the pixelated image in the top center of the Figure. We averaged the spectra from the 30 red colored pixels concentrated at the center of this image. This average spectrum is plotted as the smooth red curve in the Figure. The standard deviation for these pixels was usually around 5%.

To examine different spatial regions on the surface of the microbead we focused on acquiring spectra from individual pixels. The resolution, in this case, would be on the order of ~ 3 nm/pixel. Accordingly, the spectrum for two different pixels was obtained. These pixels are identified by the targets ⊕ and vertical green and blue arrows in the grayscale pixelated image. The spectrum from the center target ⊕ is shown in green and the spectrum from right hand edge pixel is the dark blue target ⊕ at the tip of the blue arrow. A third target ⊕ is visible at the top edge of the dark gray "donut ring" of the grayscale image. Its spectrum is plotted as the pink curve.

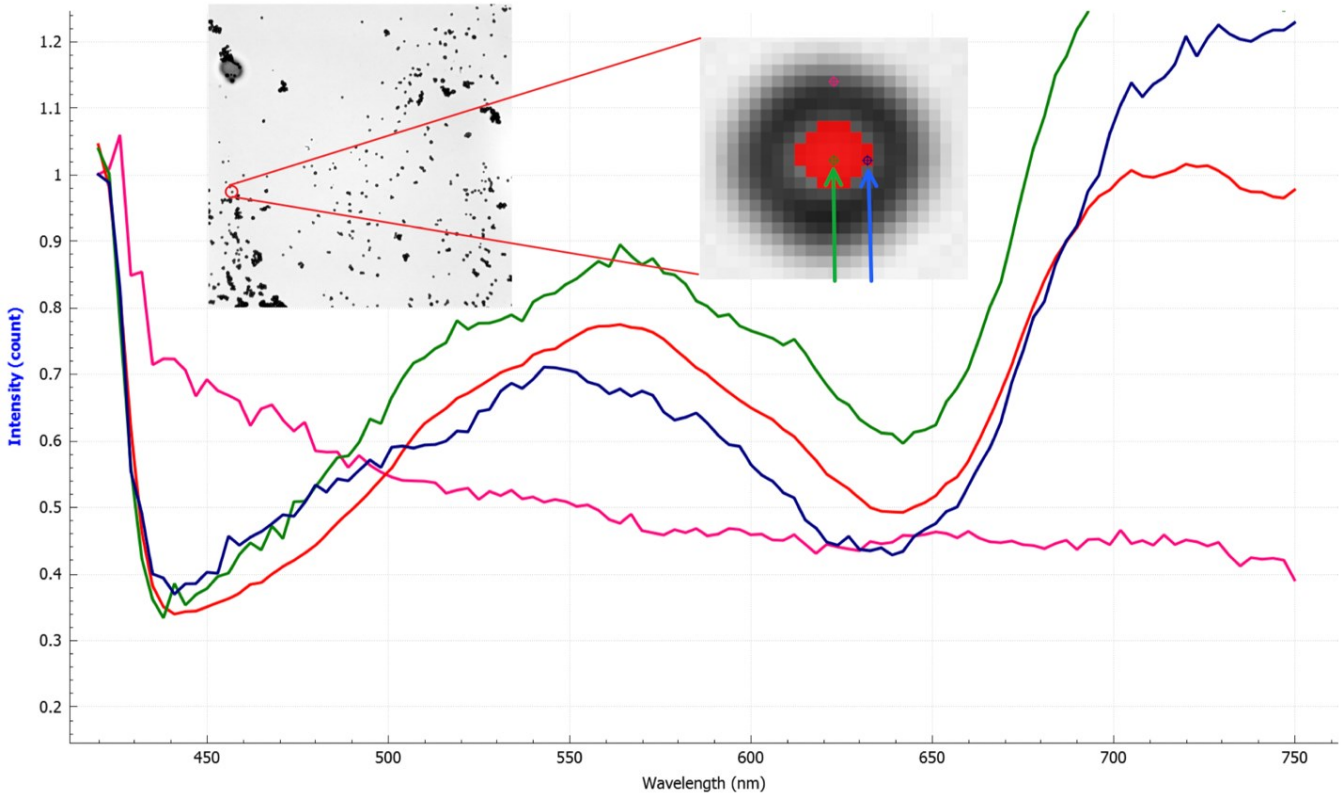

Figure 4.5: Transmittance spectra for a green CNC microbead (1:1 Yellow 5:Blue 1). A black and white microscope image is shown with the selected ("green") microbead (black dot) circled in red. A second enlarged image is provided as a grayscale pixelated plane with the locations where the spectra were obtained. The green and blue spectra are from individual pixels located at the center of the microbead (green target) and the far-right hand side (blue target). The red spectrum is the average over all the red colored pixels in the center of the microbead, and the pink spectrum is from a pixel on the edge of the microbead (Top target in the "donut ring".).

The reader is referred to Figure 4.5 where Yellow 5 and Blue 1 show absorption maxima in water at 425 and 625 nm, respectively. One might question our use of the absorption maxima

of the dyes in water to inform our interpretations of the spectral features in Figure 4.5. A more detailed approach would apply corrections to the image. For HSI, the problem of image quality requires characterization of the charged coupled device (CCD) or complementary metal-oxide semiconductor (CMOS) sensor and the lens set in front of the detector, which comprises several glass components. To date, accurate prediction of its characteristics for HSI is unsolved. The resulting digital image quality of the microbead pigment particle is thus the result of the combination of the lens and sensor properties in terms of resolution, color rendering, and aberrations. For example, when we measure the spectrum (pink curve) from the target located in the "donut ring" at the top of the pixelated plane, the spectral features pertaining to the dyes are lost. This is also likely due to the curvature of the microbead that takes the edges of the microbead out of focus. To reduce uncertainty in our measurement, we chose to collect data from regions like those shown in the red zone of the grayscale pixel map in Figure 4.5. This approach, while qualitative, allows us to assume that the aberrations associated with the instrument are the same when collecting spectra from the same spatial region of multiple pigment particles.

As described above, the red spectrum in Figure 4.5 is the average over all the red pixels in the center of the microbead. The green spectrum was acquired from a single pixel identified in the center by a green target ⊕ and indicated by the green arrow. The dark blue spectrum was obtained from the pixel identified by a blue target ⊕ (green arrow) as the last red pixel to the right of the central target. The spectra must be read as "transmittance". Therefore, the low intensity counts near 640 nm correspond to the *maximum absorbance* of Blue 1 (~ 625 nm maximum in water) and the low intensity counts near 440 nm correspond to the maximum absorbance of Yellow 5 (~ 425 nm in water). Clearly, there is a bathochromic shift in the absorption maxima of both dyes when bound to the cellulose nanocrystals at the nominally dry microbead surface. Compared with the averaged spectrum (red curve) there is qualitatively little change in the spectra. The counts for the 2 dyes in the different pixel locations are similar, suggesting that the dye components are distributed roughly equally on the microbead in the surface region we examined. The findings suggest for the green pigment particles that the hue originates in the outcome of competitive adsorption and "molecular mixing" of the Blue 1 and Yellow 5 dye molecules on the individual nanocrystals that make up the microbead. Repeating the experiment by examining other microbeads gave similar results. Some of the findings are presented below in section 4.3.2

4.3 Results and Discussion

4.3.1 Individual dye CNC pigment HSI

This section details our studies of the Blue 1, Red 40 and Yellow 5 pigments. This section is the background to the following section that uses the HSI instrument to examine the dye distribution on the surface of pigment particles prepared from binary dye binding. In all cases, within a given color regime below, many pigment particles were examined to establish particle-to-particle dye reproducibility over the microbead surfaces. All pigment particle types were sampled under identical conditions. The present section expands on the reflectance data of Chapter 2 and the polyelectrolyte complex formation studies of Chapter 3.

Figure 4.6 compares the spectra obtain from a Blue 1 pigment particle. The particle is circled in red in the false color optical micrograph insert. The average transmittance (red spectrum) was collected from 30 pixels located in the center of the microbead. The blue spectrum was collected from a single pixel also located in the center of the microbead. We surveyed other pixels in the central region and found no differences among the spectra. In other words, the dye distribution in the central region was uniform. The lowest transmittance (greatest absorbance) bottomed out between 575 and 680 nm. The blue pigment has a transmittance that is significantly lower than the background signal. This results in an anomalous background correction to the spectra.

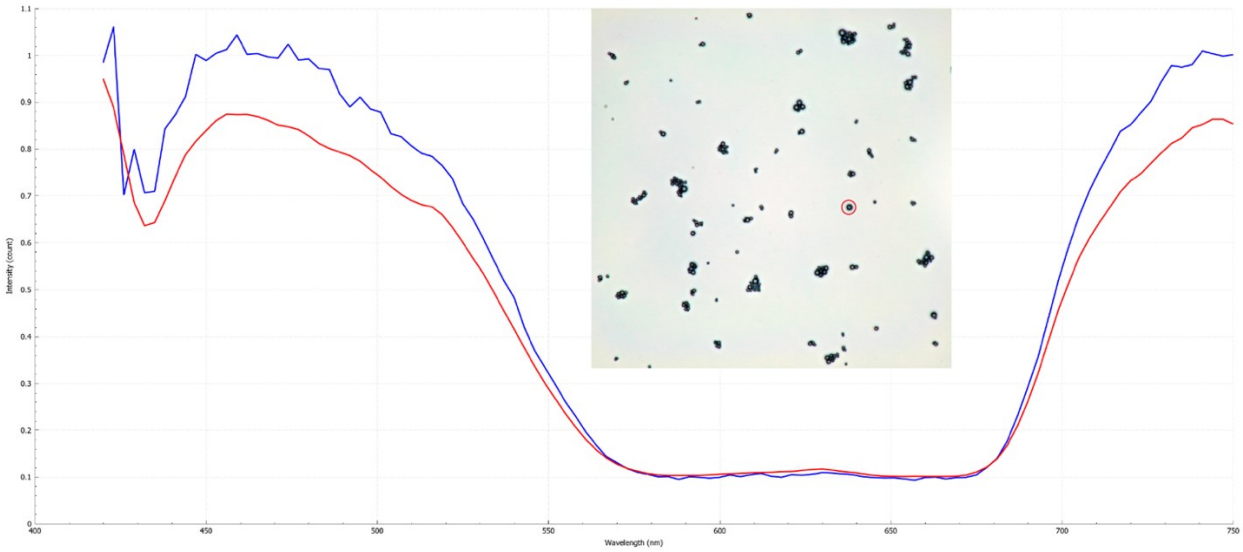

Figure 4.6: Transmittance spectra for a Blue 1 CNC microbead. A false colour image of the HSI cube is shown with the selected microbead circled in red. The blue spectrum represents the

transmittance for a pixel, and the red spectrum represents the average transmittance for the center 30 pixels of the microbead.

Figure 4.7 assembles the transmittance spectra for a Red 40 microbead. The spectra were acquired in the same manner as the Blue 1 sample. The lowest transmittance was found in the region of 435 and 550 nm. The transmittance maximum is blue-shifted compared with that of Blue 1. This simply reflects how the electronic transitions differ between the two types of dye molecules. Individual pixels arrayed within the center of the microbead exhibited transmittance very close to that of the average. We conclude that the distribution of dye at the surface of the microbead is approximately uniform.

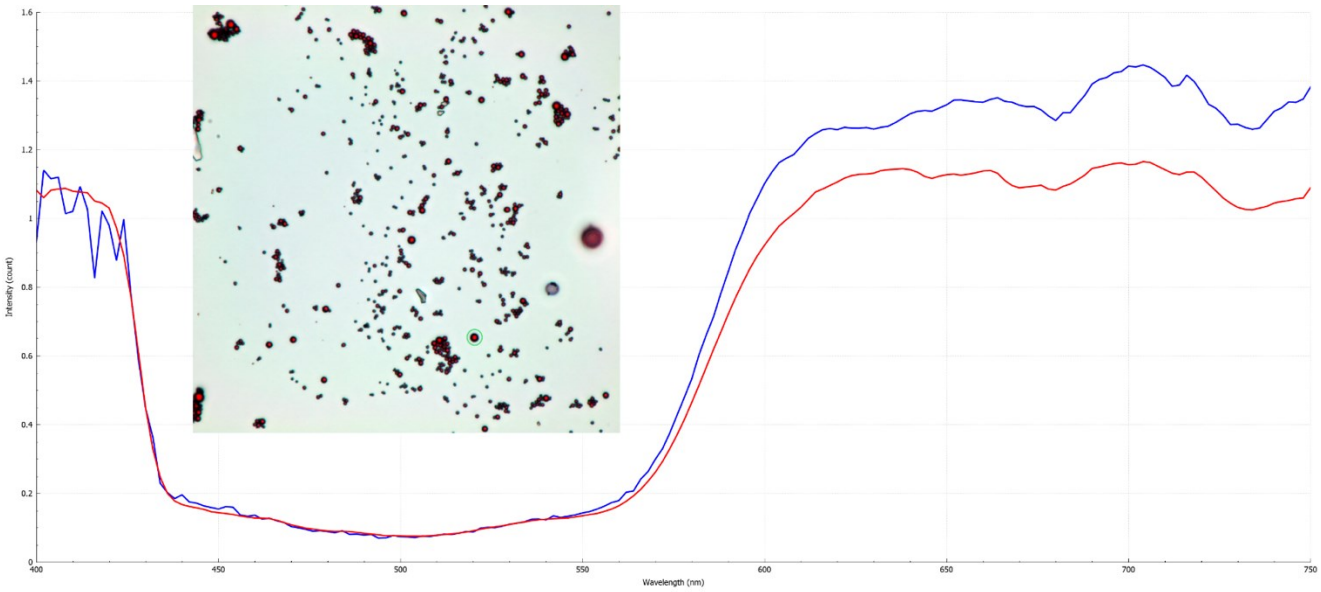

Figure 4.7: Transmittance spectra for a Red 40 CNC microbead. A false colour image of the HSI cube is shown with the selected microbead circled in green. The blue spectrum represents the transmittance for a single pixel, and the red spectrum represents the average transmittance for the center 30 pixels of the microbead.

Data for the Yellow 5 pigment particle were acquired in the same manner as described above. The results are collected in Figure 4.8, where it is seen that the transmittance minima span from 440 nm to approximately 475 nm. All 30 pixels within the center of the microbead had a transmittance very close to that of the average. The false colour processing makes the pigments appear more orange than yellow.

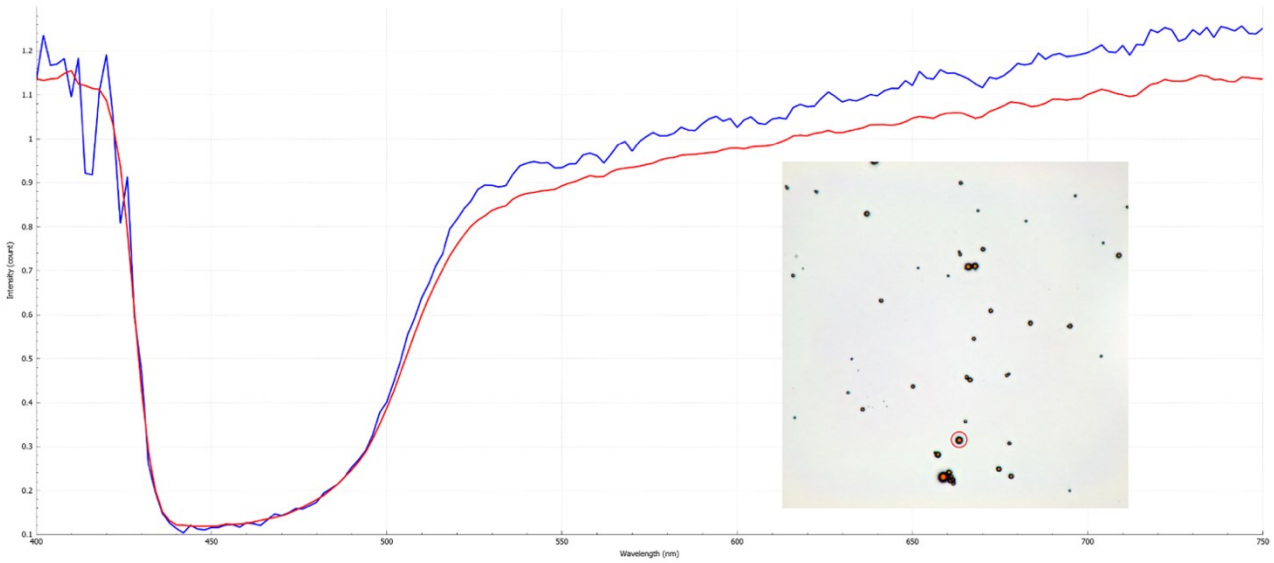

Figure 4.8: Transmittance spectra for a Yellow 5 CNC microbead. A false colour image of the HSI cube is shown with the selected microbead circled in red. The blue spectrum represents the transmittance for a pixel, and the red spectrum represents the average transmittance for the center of the microbead.

Overall, the three pigment types show that the dye is approximately uniformly distributed over the surface of the microbead. The HSI "spectra show anomalous saturation" evidenced by the flat bottom of Figures 4.6 and 4.7 (and 4.18 below). Nevertheless, the centers in minima in transmittance correspond approximately to the expected positions for each of the pigment types.

4.3.2 Dye Mapping of CNC Pigments

Here we use HSI to map the spectral response of binary dye pigment particles. We first examine the purple pigment prepared by 1:1 competitive molecular mixing of Red 40 and Blue 1 dye molecules on CNC+ nanocrystals, followed by spray drying. The ratio refers to the feed ratio in the aqueous medium used to mix CNC^{+} and dye molecules. Competition for dye adsorption sites might change the ratio.

By HSI most microbeads were found to have a uniform distribution of both dye species of molecules on the surface. In exceptional cases, we observe that the Red 40 dye appears to be inhomogeneously distributed. This is evident in Figure 4.9 below for two microbeads where we interrogate different regions of them. The locations of the microbeads in the sample plane of the microscope slide are identified as the red circled beads in the optical micrograph inserts. The corresponding pixel maps are shown in the enlargement to the right. The central red pixelated

zone comprises 162 pixels. The central target is indicted by a green ⊕. The blue target at the bottom right of the pixel plane identifies where the blue spectrum was collected. The transmission minima occur at ~500 nm (Red 40) and ~640 nm (Blue 1). Comparing the red and blue spectra, there appears to be slightly more Red 40 dye that has been accumulated by nanocrystals in the spatial region identified by the blue target. This is also true of the microbead identified in the bottom Figure, where the bead appears to be in contact with another.

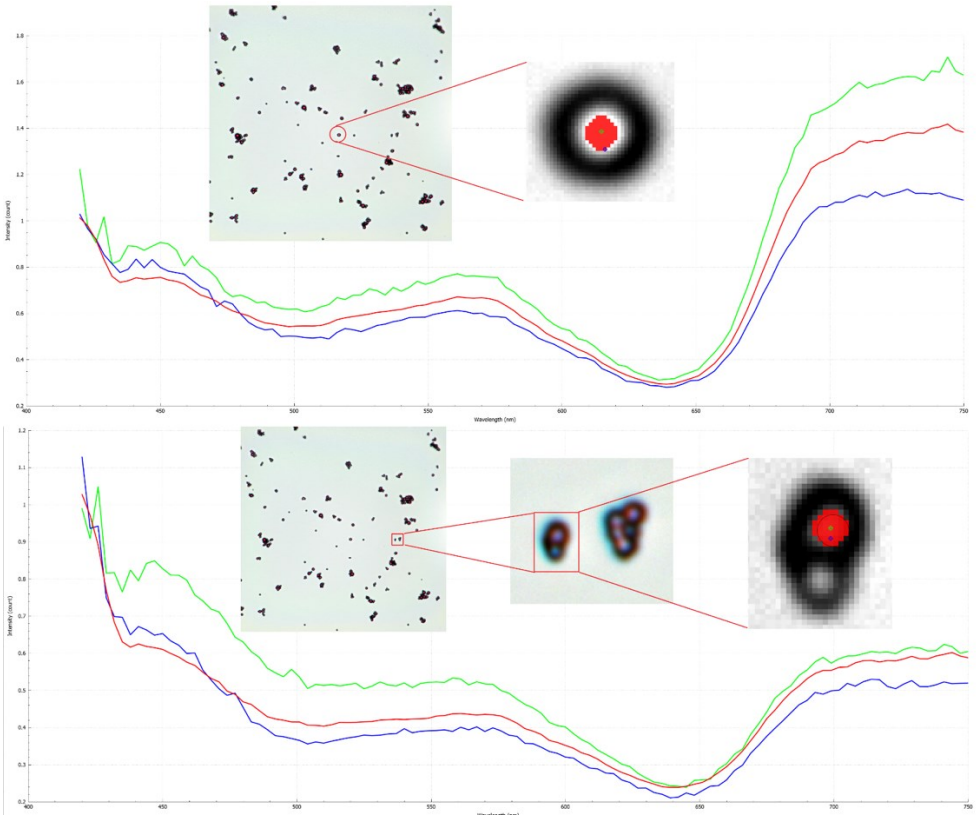

Figure 4.9: Transmittance spectra for purple 1:1 Red 40: Blue 1 CNC-based microbeads. Top spectra: False colour images of the HSI cube are shown with the selected microbead circled in red. The ⊕ targets identify the single pixels where the green and blue spectra were collected. The red spectrum is the average over all of the red pixels. Bottom spectra: A larger scale false colour image is provided. An image of where the spectra are selected from is shown for each microbead. The ⊕ targets identify the single pixels where the green and blue spectra were collected. The red spectrum is the average over all of the red pixels.

On average, the two microbeads have approximately the same composition. This is evident by comparing the red spectra that average the red pixelated region for the two microbeads. Thus, overall, the purple pigment appears to be uniform in color from microbead to microbead. This uniformity is consistent with what the human eye can distinguish.

The green CNC pigment was produced by co-adsorption of Blue 1 and Yellow 5 dye in a 1:1 ratio. Our survey of the sample revealed that few microbeads exhibited nonuniformities in dye distribution on the microbead surface. In two cases shown in Figure 4.10, there appeared to be larger accumulations of blue dye in regions indicated by the blue targets.

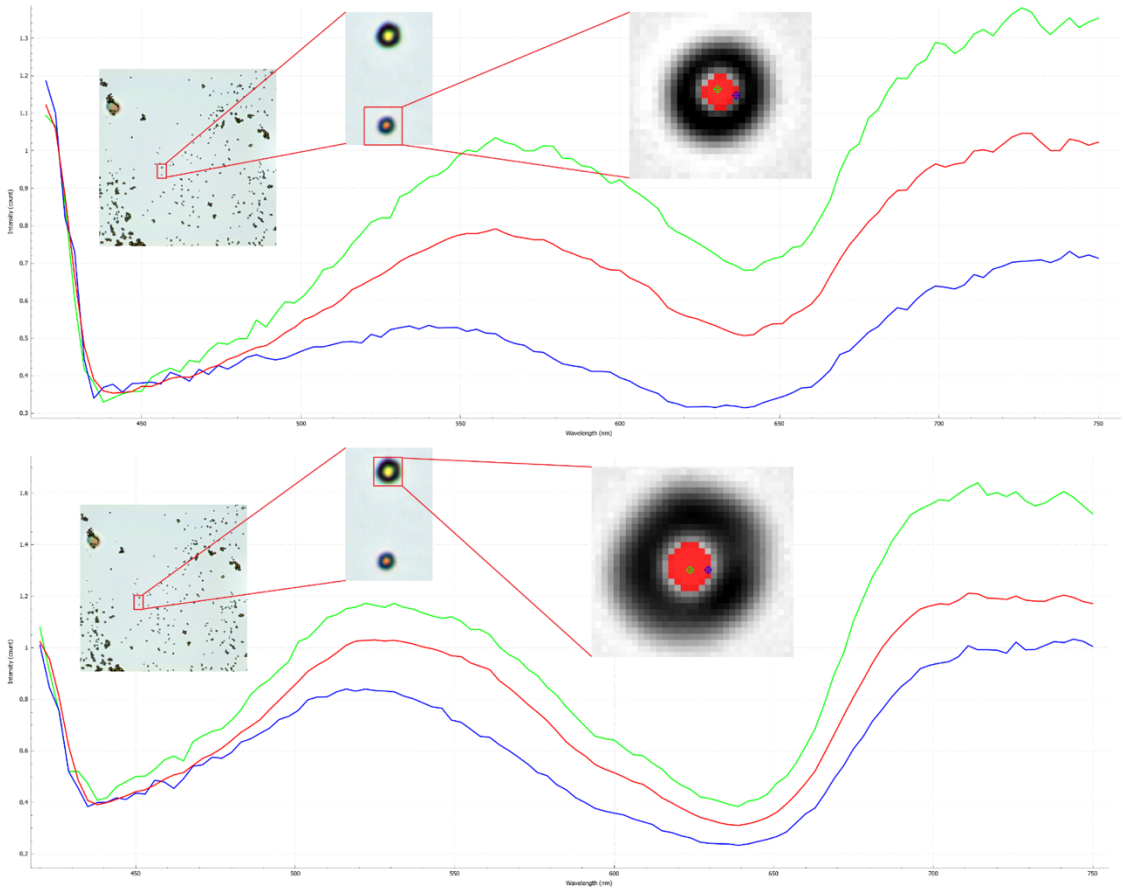

Figure 4.10: Transmittance spectra for green 1:1 Blue 1: Yellow 5 CNC-based microbeads. Top spectra: False colour images of the HIS cube are shown with the selected microbead circled in red. The ⊕ targets identify the single pixels where the green and blue spectra were collected. The red spectrum is the average over all the red pixels. Bottom spectra: A larger scale false colour image is provided. An image of where the spectra are selected from is shown for each microbead. The ⊕ targets identify the single pixels where the green and blue spectra were collected. The red spectrum is the average over all of the red pixels.

The red spectra correspond to the average over the red pixelated areas in each case. Observe that the spatial dependence of the spectra that arises when comparing the red and blue target areas brackets the averaged spectrum. We conclude that on average, small variations in the spatial distribution of the dyes will have no impact on the perception of the hue by the human eye.

We were unable to extract meaningful data from the pigments exhibiting orange hues. Spectral overlap of the dye absorptions distorted the transmittance features and background corrections were unsuccessful in separating the two absorption lineshapes.

4.3.3 Observing CNC Pigment Dye Release/Uptake by Hyperspectral Imaging

In this section, we revisit the study of dye release described in Chapter 3, section 3.3.4. Serendipitously, we discovered that locating 2 different colored pigment particles together in water not only encouraged the release of dye but also resulted in dye exchange in the microbeads such that they took on different hues. For example, yellow microbeads co-located with blue microbeads in water produced green microbeads by dye exchange. Although dye leaching is undesirable for many commercial applications, the phenomenon opens the door to exploring the process as a paradigm for controlled release relevant to pharmaceutical drug delivery vehicles, and even the study of adsorption-desorption phenomena and chemical reactions in nanoporous microbead structures. Moreover, there are very few studies of binary adsorption of dyes by cellulose matrices.[9] This chapter sheds new light on the impact of binary dye binding to produce new hues of pigment CNC microbeads.

We first study the interaction between Blue 1 and Red 40 pigment particles. These were prepared as described in Chapter 2. Because the diffusion (release) of Blue 1 is rapid on the time scale of initiating the HSI experiment, we added glycerol to water to increase the local viscosity. Accordingly, 1:5 water:glycerol solution was first prepared. Then a small amount of Blue 1 CNC pigment powder was placed on a slide. A Pasteur pipette was used to deposit a single drop of the water:glycerol solution on top of the pigment. Next, a small quantity of Red 40 CNC pigment was placed next to the drop containing the blue pigment. With a micro-spatula, the red pigment was mixed into the aqueous suspension of Blue 1 microbeads. The sample was inserted beneath the objective of the HSI unit and data collection was initiated. It required approximately 30 seconds to acquire a data cube. We inserted a 30-second delay before acquiring the next cube. This means that the image cubes were obtained at approximately one-minute intervals. A total of 10 cubes were obtained so that dye release was observed for about 10 minutes. The image cubes were then analyzed using PHySpec software. Background correction was performed for each cube as described in section 4.2.3. We analyzed 20 microbeads. As shown in Figure 4.12 below, the spectra were obtained as averages of 30 pixels at the center of the microbeads (red circular

pixelated region). To ensure that the pixel area used to obtain the spectra were consistent between time points, the same pixel area was interrogated for all microbeads under study. Transmittance spectra were obtained at time points, t = 0, 2, 4, 6, 8, 9, and 10 minutes.

There is a distribution of distances among the microbeads. Obviously, once diffusion starts the trajectory of the diffusing dye is undetermined since the beads are spherical, the adsorption strength of the dyes is unknown, and the beads are immersed in an aqueous medium where they exhibit Langevin dynamics. By trial and error, we observed that the uptake of blue dye by red microbeads depended on the spatial separation of the pigment particles. We assigned the microbeads letter symbols A, B, C, and D according to their approximate spacing. Microbeads labelled A and B were assigned to Red 40 pigment particles. The designation A indicates that the Red 40 microbead has no Blue 1 microbead directly adjacent (contact), while B means contact. C and D designates blue microbeads. C means that no microbeads (red or blue) are in contact, while D means a blue microbead contacts a red microbead. All labels for the microbeads are shown in Figure 4.11 below. The numbers are used in the text so that the reader can locate the particle(s) under study.

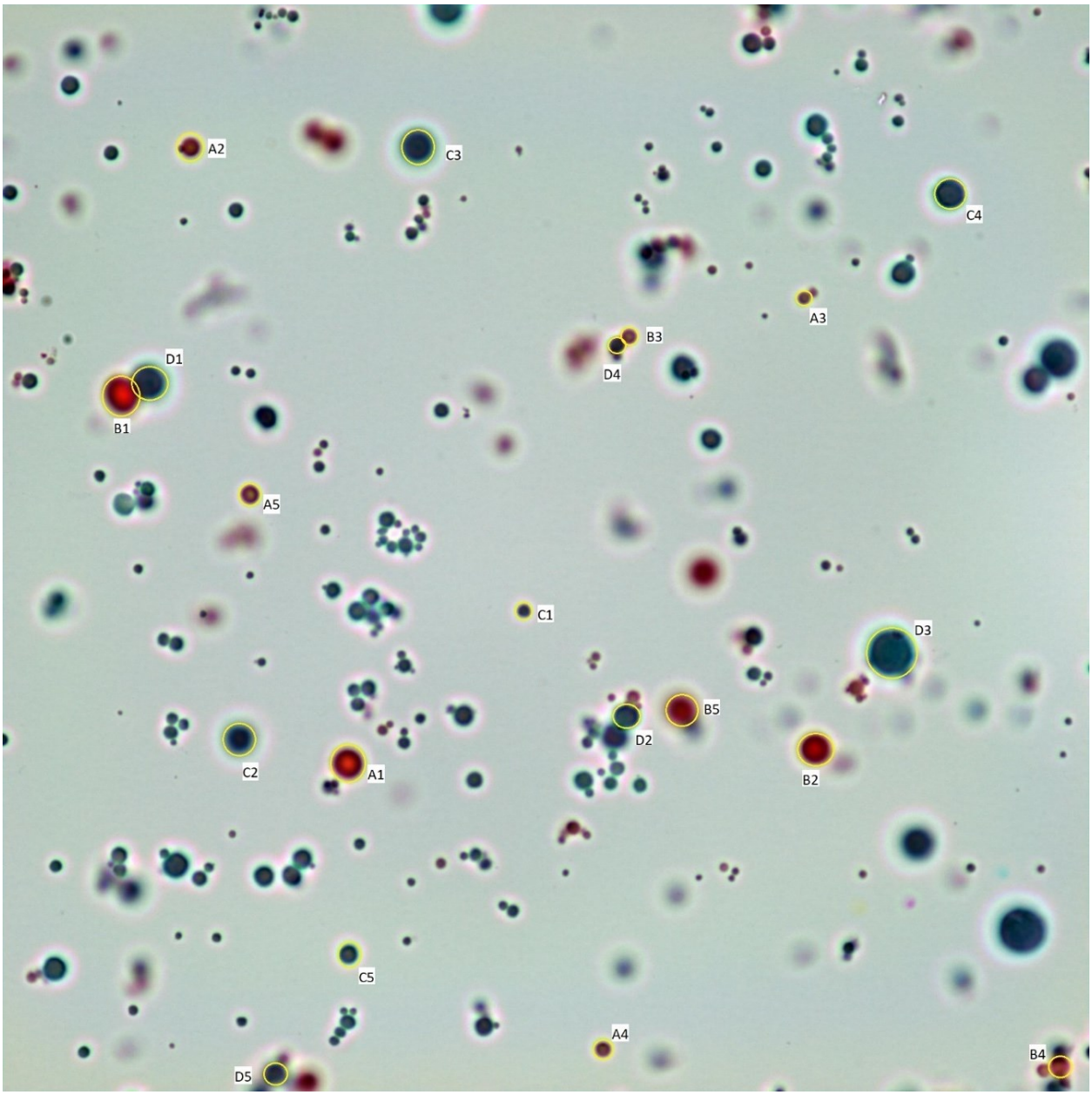

Figure 4.11: False colour image of an HSI cube with red and blue CNC microbeads in water glycerol 1:5 at time, t = 0. The 20 microbeads whose transmittance spectra are analyzed are circled in yellow and labelled. 'A' and 'B' microbeads are Red, and 'A' indicates the microbead does not have a contacting Blue microbead. 'B' indicates a contacting Blue microbead. 'C' and 'D' microbeads are Blue. 'C' indicates the microbead does not contact a Red microbead. 'D' indicates that it contacts a Red microbead.

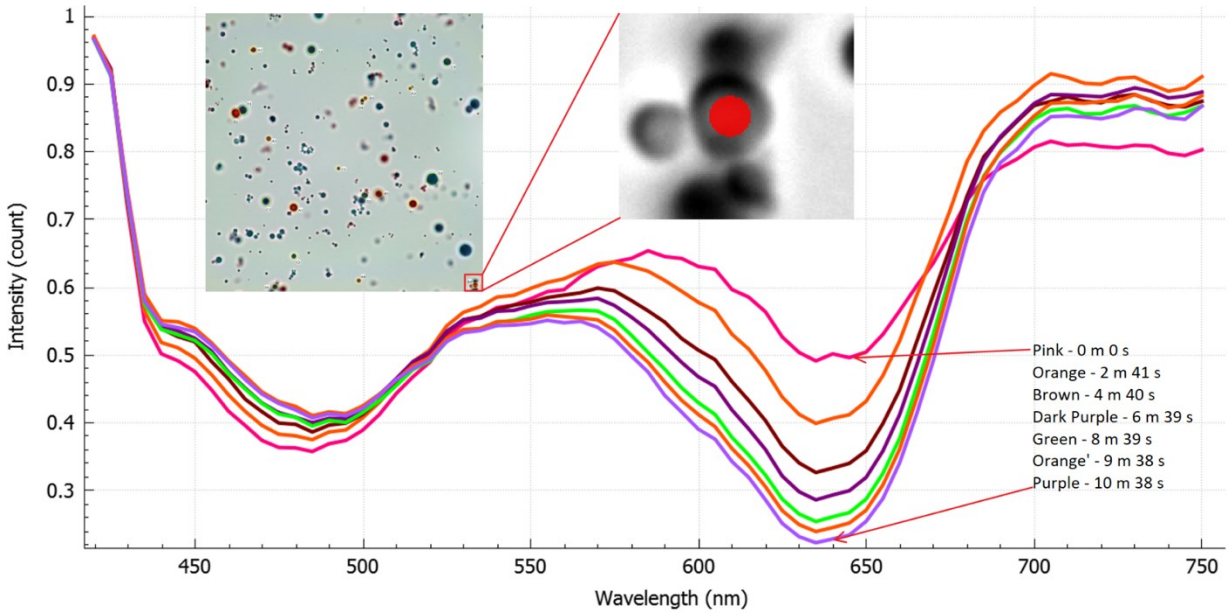

Figure 4.12: Transmittance spectra of a B4 (red contacting blue) microbead at different times. A false colour image of the entire sample is shown in the insert. The expanded insert shows an image of the B4 microbead with the pixel area (in red) whose transmittance is averaged. The timestamp of each spectrum is labelled in the bottom right.

Figure 4.12 shows the time evolution of changes in the transmittance spectra of a B4 (Red 40) microbead (bottom right of the Figure) touching Blue 1 microbeads. Clearly, the absorbance of the blue component of the dye increases near the peak absorption maximum (transmittance minimum) at 640 nm. Simultaneously, we observe a decrease in absorbance of the component of Red 40 in the microbead. We interpret the findings as follows. From the experiments described in chapter 3, Blue 1 appears to be more labile (more easily released) than Red 40. In Figure 4.12 there is an isosbestic point at 520 nm. This suggests that the Blue 1 and Red 40 dye compete in the interconversion (dye exchange) to give the pigment particles with a different (purple) hue. Note that we measure the change in absorbance at the microbead surface, not in the surrounding medium. Thus, the peak maximum in absorbance is ~ 635 nm for the increase in Blue 1 on the red microbead, and 440 nm for the loss of Red 40 on the same microbead. From chapter 3 the molar extinction coefficient of Blue 1 (97734) is almost 4 times as large as that of Red 40 (25495). In Figure 4.12, this difference appears to enhance the change in the spectral absorption (decreases transmittance) of Blue 1 compared with Red 40. Clearly, there is an uptake of blue dye by the red pigment microbead. This suggests that new binding sites must open to accommodate the blue dye at least on the surface of the red microbead.

Modelling of multi–component dye adsorption is a complex problem since it is affected by the interactions and competitions between adsorbents and adsorbates.[10] If Red 40 dye leaves, then desorption of red dye might account for the uptake of blue dye in the microbead. Figure 2.9 in chapter 2 reveals that the Blue 1 dye molecule appears to offer more adsorption sites than Allura Red 40. Both dyes can engage the PDDA/CNC surface via electrostatic attraction/repulsion, π-π stacking (attraction), and hydrogen bonding (attraction). These are indicated in Figure 4.13 below.

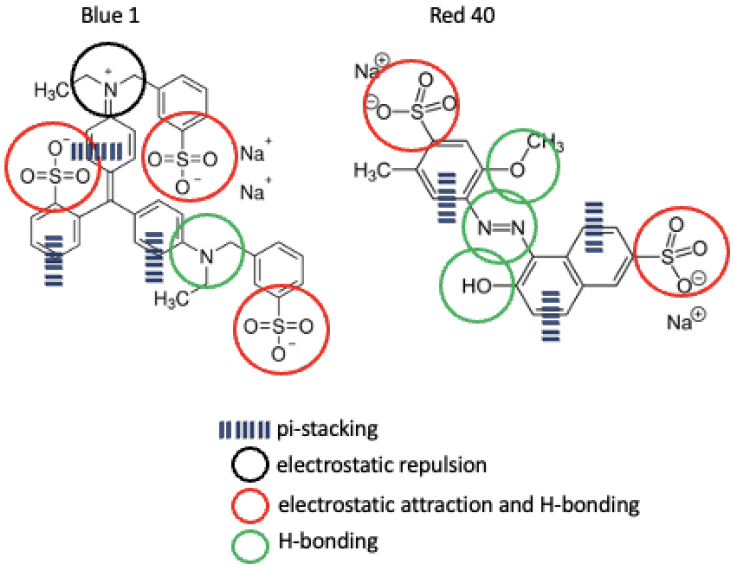

Figure 4.13: Modes of interaction for dyes with PDDA and CNC.

The presence of three sulfates in the Blue 1 molecule suggests the potential for stronger or more numerous attractive electrostatic interactions with PDDA. Figure 3.4 (previous chapter) suggests this is unlikely because the tautomers up to pH 8 have only 2 sulfates that are charged. Sulfates are rather weak ligands, so we do not expect direct coordination with the dimethylammonium moieties of PDDA. The cation in PDDAA is a sterically crowded saturated nitrogen heterocycle with dimethylammonium supplying the charge. The Coulomb potential between one dye molecule sulfate and a monomer unit of PDDA will vary roughly as $1/r^2$, where r is the interaction distance. Of course, it is possible that a dye molecule will interact with more than one monomer unit, in which case we might think of the PDDA as having a surface charge density with which to interact with the dye. PDDA has 1 unit of positive charge per 0.54 nm along the length of the chain. In a simplified view where we regard the PDDA as a rod-like entity, the axial linear charge density will be on the order of σ = e/1.0 nm, where e is the charge.

Dye molecules like those considered here are typically 1-1.5 nm long by 1 nm wide. This suggests that the sulfate anion substituents for both Red 40 and Blue 1 can access the backbone PDDA charge density about equally. Blue 1 has 2 tertiary amines. The tautomeric equilibrium (Figure 3.4) shows that the alky ammonium (species III) or the iminium (species III′) are positively charged, so for the 2 negative charges on Blue 1, there are also 2 positive charges. It is therefore possible that the apparent weaker binding of Blue 1 compared with Red 40 is due to the additional repulsive potential towards PDDA on the former. Moreover, from Figure 4.13 above there appear to be fewer H-bonding interactions available to Blue 1. The putative pi-interactions will be weak. In the end, we recommend a study of the competitive binding of the dyes to CNC and $cCNC^{+}$ microbeads to learn if the adsorption capacity of the dyes is reduced by competitive binding.

We simultaneously acquired data cubes for the 20 microbeads shown in Figure 4.11. The spectra are plotted together to follow the time rate of change in dye transmittance (absorbance) profiles. We begin by referring to Figure 4.15. These are B1-D1 (Red contacting Blue at position 1) and A1 (Red isolated from Blue 1 microbeads at position 1). We first examine the changes in transmittance of the 475 nm peak corresponding to the red dye. These are shown in the top and bottom spectra of the Figure. In both cases (contacting and isolated) the Red 40 microbead exhibits a decrease in absorbance (increase in transmittance) in Red 40 dye content over time. This must mean that Red 40 dye is desorbing from the red pigment microbead. Simultaneously, we observe systematic decreases in transmittance corresponding to blue at ~ 635 nm. This indicates that the Red 40 microbead is adsorbing Blue 1 dye. The isosbestic point at ~520 nm indicates an equilibrium between the dye species.

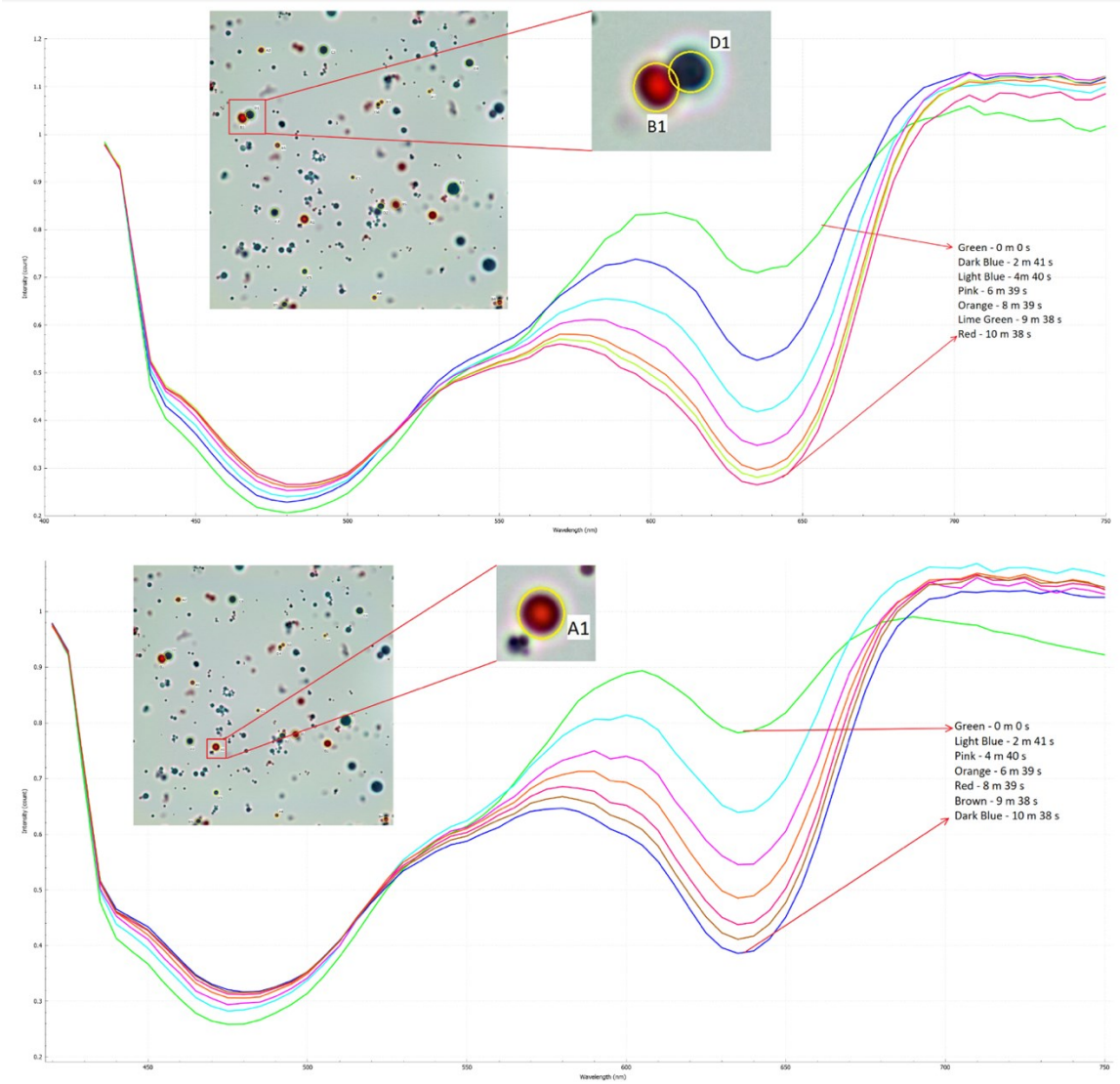

Figure 4.15: Time evolution of changes in transmittance spectra of B1 (top) and A1 (bottom) microbeads. The timestamp of each spectrum is labelled on the right. False colour image inserts show the respective microbeads, their identity, and their positions as indicated in Figure 4.11.

To clarify the kinetics, we plotted the transmittance of the red and blue transmittance against time in microbeads labelled A1 through B5. The results in Figure 4.16 are also normalized for easier comparison among the different microbeads. Figure 4.16 shows the results for the maximum blue transmittance at 635 nm. In all cases the transmittance at 635 nm decreases with time, i.e., the content of Blue 1 dye in the Red 40 microbeads A (isolated) and B (contacting a Blue 1 microbead) increases. From the normalized plots, the majority of the Red 40 microbeads in contact with Blue 1 microbeads show a steeper initial decrease in the

transmittance. This suggests that dye uptake depends on the spatial distribution of the pigment particles: adjacent or touching particles adsorb Blue 1 dye more readily than isolated red 40 particles.

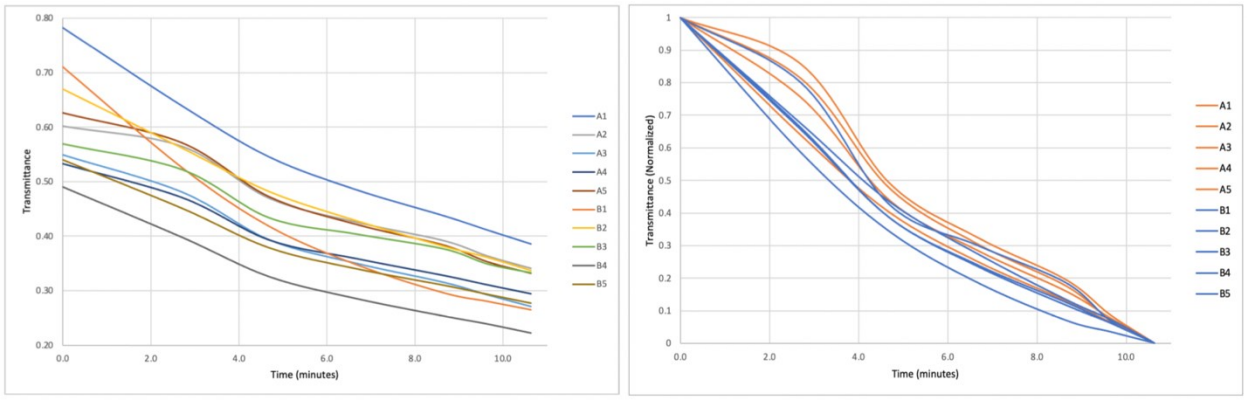

Figure 4.16: Transmittance time dependence of Blue 1 dye uptake by Red 40 A 1-5 (isolated) and B 1-5 (touching) microbeads. Transmittance at 635 nm (left) and normalized transmittance (right).

We then studied changes in the Red 40 dye composition on the microbeads, A1-B5. Accordingly, the plots for the peak (maximum transmittance) at 475 nm are assembled in Figure 4.17 below. There appears to be a greater initial increase in transmittance for the isolated red microbeads, i.e., the Red 40 dye departs at a rate commensurate with the increase in the rate of uptake of the Blue 1 dye. This makes sense, given the existence of the isosbestic point. Overall, we find that every microbead examined shows an increase in transmittance, representing a decrease in the amount of red dye.

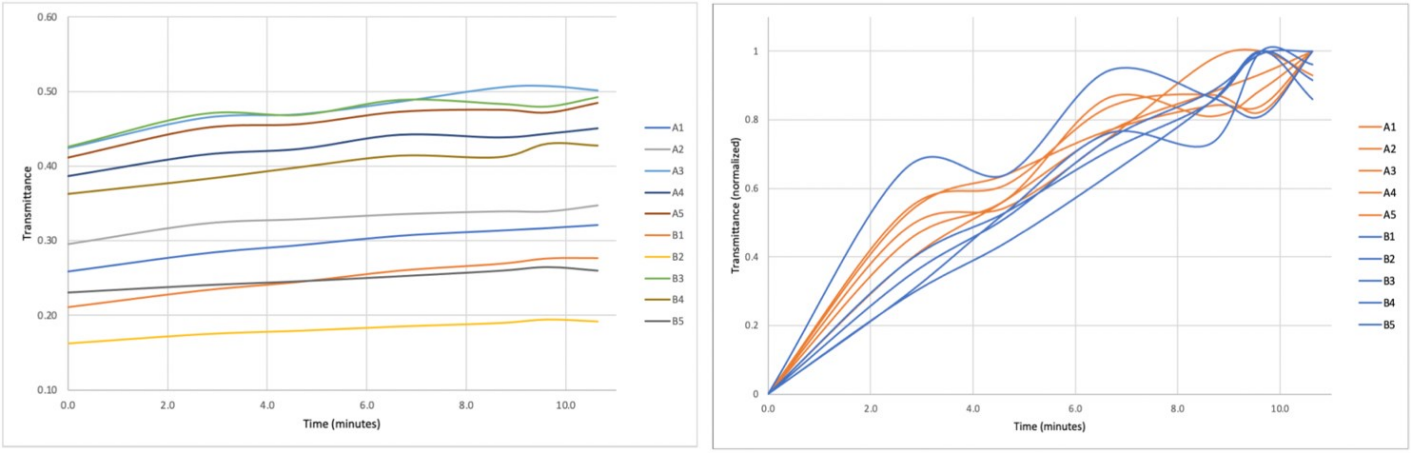

Figure 4.17: Time-dependent change in transmittance (left) and normalized transmittance (right) at 475 nm plotted for all red microbeads, A 1-5 (isolated) and B 1-5 (touching).

Next, we studied the time evolution of changes in the transmittance of 10 blue microbeads. The transmittance spectra were obtained and all ten showed similar trends. The spectra associated with the beads are identified as C1-5 and D1-5, isolated and touching, respectively. Figure 4.18 below shows the spectra of microbeads C4 (isolated) and D2 (touching Red 40). Overall, the changes in the spectra between different time points are much smaller for the blue microbeads when compared to the red. This can be explained by the tighter binding of Red 40 (slower release) and the fact that there is an excess of Blue 1 pigment microbeads over the Red 40 microbeads. Despite the anomalous spectral line shape in the region 575-675 nm for Blue 1, there is a clear isosbestic point for both the isolated and touch Blue 1 microbead. Evidently, the bottom spectrum reveals that the acquisition of Red 40 dye is greater when the microbeads are in contact.

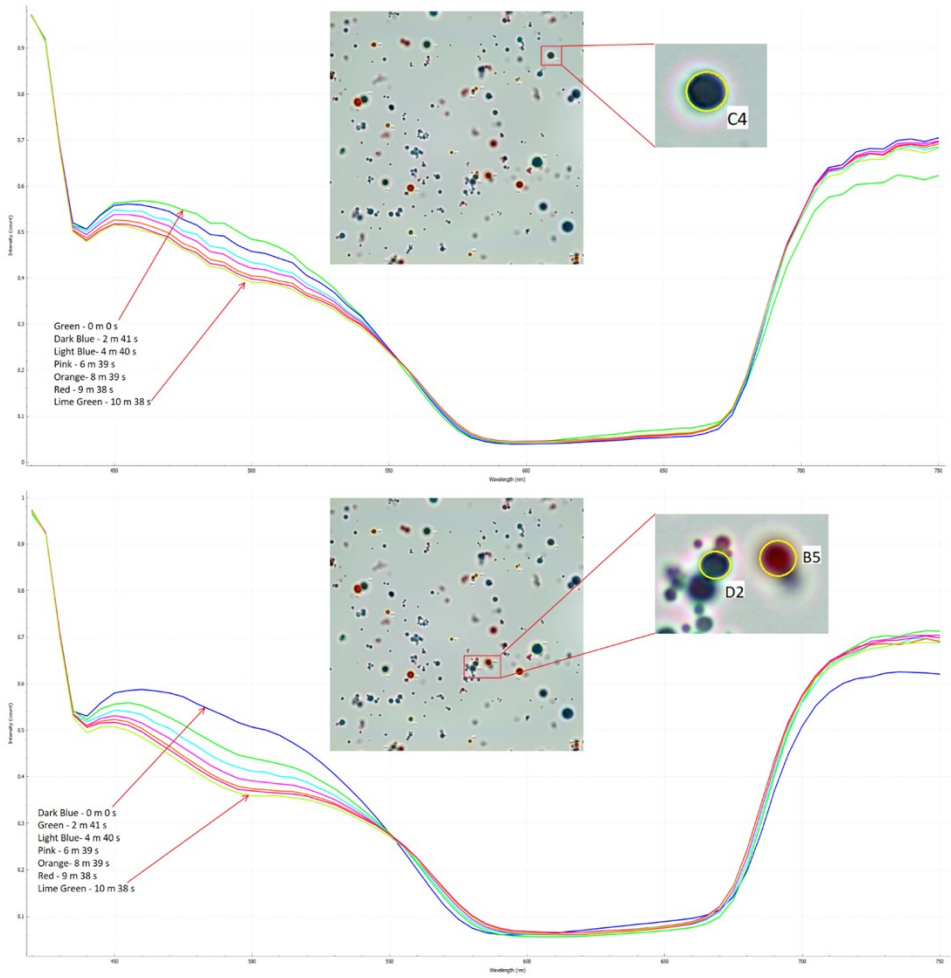

Figure 4.18: Transmittance spectra of C4 (top) and D2 (bottom) microbeads at different times. The time of each spectrum is labelled at the bottom left.

The kinetic plots of Figure 4.19 reveal some additional information. The left-hand plot shows the time evolution of the change in transmittance measured at 635 nm. The normalized spectra (right) make it clear that all samples show a steep decrease in transmittance over the first 3 minutes. Then the amount of dye present then becomes stable, and only small fluctuations occur over the remaining time. There is also no clear difference in the trend for blue microbeads that are isolated or located with an adjacent red microbead.

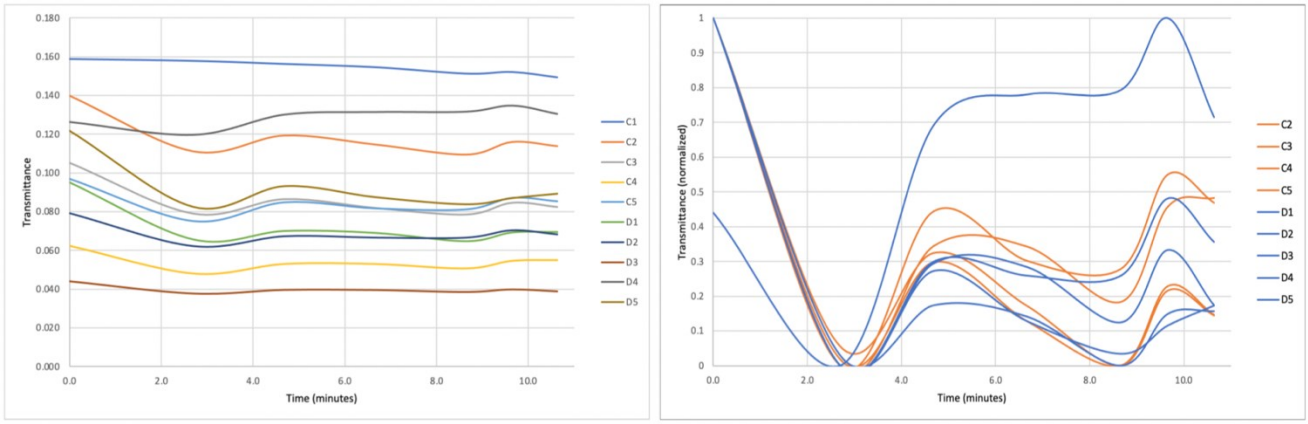

Figure 4.19: Transmittance (left) and normalized transmittance (right) at 635 nm plotted for all blue microbeads, C 1-5 (isolated) and D 1-5 (adjacent), at varying times. C1 is not included in the normalized plot.

The trend for transmittance at the Red 40 dye wavelength at 475 nm provides the expected result; there is a gradual decrease in transmittance over time for all the microbeads except for a D4 outlier. The latter is an individual blue microbead surrounded by many red microbeads, visible in Figure 4.11. Figure 4.20 also indicates that there is generally a more rapid decrease in transmittance for microbeads with an adjacent, touching red microbead. The proximity of the microbeads likely accelerates dye diffusion and adsorption. Although all blue microbeads followed the trends explained above, one exception is C1, which as seen in the normalized plot has very little change in both blue and red. This is likely due to it being extremely isolated as seen in Figure 4.11.

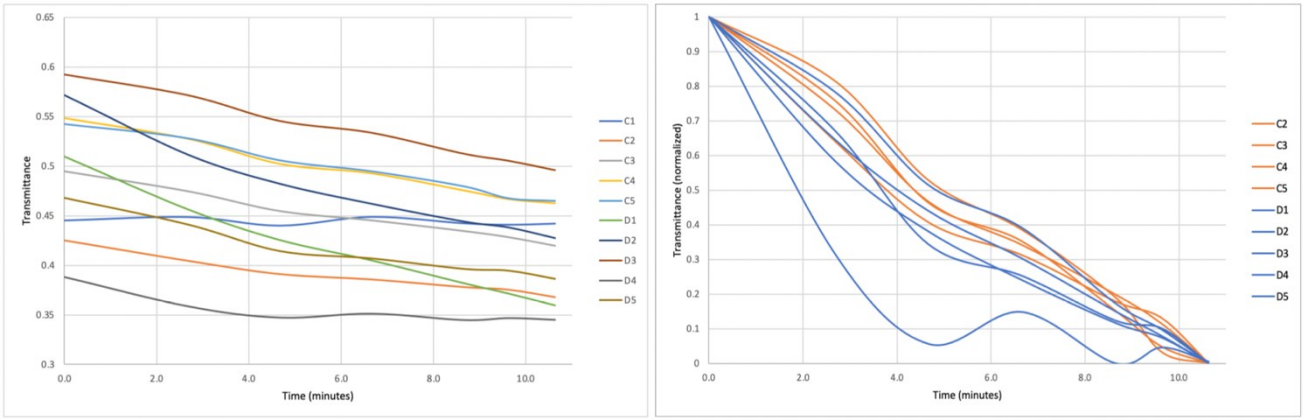

Figure 4.20: Transmittance (left) and normalized transmittance (right) at 475 nm plotted for all blue microbeads, C 1-5 (isolated) and D 1-5 (adjacent), at varying times. C1 is not included in the normalized plot.

4.4 Conclusions

HSI was used to map dye distributions by reflectance from nominally dry CNC-based pigment microbeads. The blue pigment showed a peak absorbance near 635 nm, and both the red and yellow pigments showed maxima in the range 430 – 500 nm. The peaks are red-shifted from the peak maxima of the free molecules and cCNC+ dye complexes in water. For the pigments with only one type of bound dye, the dye distribution was uniform on average. For hues obtained from binary combinations of dyes, the distributions of the two types of dyes was approximately uniform, though the HSI experiment suggests that competitive binding might lead to a different dye distribution over the topography of the microbead.

Dye release and uptake were analyzed for the case of co-located blue and red microbeads in water. The study used an excess of blue microbeads over the red. Red microbeads took up blue dye more than blue microbeads took up red dye. The rate of uptake of blue dye increased when microbeads were proximal.

4.5 References

1. Amigo, J. M.; Babamoradi, H.; Elcoroaristizabal, S., Hyperspectral image analysis. A tutorial. *Analytica chimica acta* **2015,** *896*, 34-51.
2. Mehta, N.; Sahu, S. P.; Shaik, S.; Devireddy, R.; Gartia, M. R., Dark-field hyperspectral imaging for label free detection of nano-bio-materials. *Wiley Interdisciplinary Reviews: Nanomedicine and Nanobiotechnology* **2021,** *13* (1), e1661.

3. Conti, M.; Scanferlato, R.; Louka, M.; Sansone, A.; Marzetti, C.; Ferreri, C., Building up spectral libraries for mapping erythrocytes by hyperspectral dark field microscopy. *Biomedical Spectroscopy and Imaging* **2016,** *5* (2), 175-184.
4. Wang, X.; Cui, Y.; Irudayaraj, J., Single-cell quantification of cytosine modifications by hyperspectral dark-field imaging. *ACS nano* **2015,** *9* (12), 11924-11932.
5. More, S. S.; Vince, R., Hyperspectral imaging signatures detect amyloidopathy in Alzheimer's mouse retina well before onset of cognitive decline. *ACS chemical neuroscience* **2015,** *6* (2), 306-315.
6. Lu, G.; Fei, B., Medical hyperspectral imaging: a review. *Journal of biomedical optics* **2014,** *19* (1), 010901-010901.
7. Wang, Y. W.; Reder, N. P.; Kang, S.; Glaser, A. K.; Liu, J. T., Multiplexed optical imaging of tumor-directed nanoparticles: a review of imaging systems and approaches. *Nanotheranostics* **2017,** *1* (4), 369.
8. Photon etc, IMA DARK User Manual; Visible and Near-Infrared Hyperspectral Darkfield Imaging System. 2020.
9. Bai, H.; Chen, J.; Zhou, X.; Hu, C., Single and binary adsorption of dyes from aqueous solutions using functionalized microcrystalline cellulose from cotton fiber. *Korean Journal of Chemical Engineering* **2020,** *37*, 1926-1932.
10. Mohammed, N.; Lian, H.; Islam, M. S.; Strong, M.; Shi, Z.; Berry, R. M.; Yu, H.-Y.; Tam, K. C., Selective adsorption and separation of organic dyes using functionalized cellulose nanocrystals. *Chemical Engineering Journal* **2021,** *417*, 129237.

Chapter 5- Conclusions and Future Work

5.1 Summary and Conclusions

Carboxylated cellulose nanocrystals, cCNC, were combined with cationic polyelectrolyte, PDDA, and anionic dye molecules in water to make pigment microbeads by spray drying. Pigment synthesis conforms to many of the principles of green chemistry and engineering. Multi-step covalent bond formation was avoided in favor of coulombic binding, much as practiced in the textile industry. Though the predominant mode of binding to the nanocrystal is electrostatic, there are likely contributions from van der Waals and hydrogen bonding forces. Pigments were prepared from FD&C Red 40, Blue 1 and Yellow 5 anionic dyes. Hues of green, orange and purple were prepared by binary competitive coadsorption of these dyes. Dye binding was assisted by attraction to a cationic polyelectrolyte complex (PEC) formed between PDDA and cCNC. When dispersed by ultrasound, the PEC yielded well-dispersed suspensions of charge inverted nanocrystals, $cCNC^{+}$. This PEC "platform" was then exposed to solutions of dye molecules. The resulting metachromic PEC suspension was spray dried to yield dry powders of vibrantly colored microbeads. The microbeads exhibited spherical morphology and diameter, D50, less than a target dimension of 4 μm. Small spherical microbeads were soft to the touch due to the ease with which they rolled on the skin. Pigment color was assessed according to CIELAB reflectance. Reflectance spectra of the Red 40 cellulose-based microbeads were compared with those of Red 40 Lake, a commercial hydrous alumina pigment widely used in the cosmetics industry. The comparative analysis was conducted in the frame of a standard cosmetics industry protocol. This standard quantitative assessment compared the coverage and saturation. Red 40 CNC pigment at 10% dye loading was inferior in terms of saturation and coverage compared with a commercial sample of Red 40 Lake. When adjusted for the difference in dye loading, the pigments performed equally. The adjustment was made by developing a method based on Beer's law to pinpoint how much dye might be loaded on the $cCNC^{+}$ platform. This was used to maximize dye loading without generating free dye in solution. The method was used to raise the Red 40 dye content to be competitive with the loading of the dye in the commercial sample of the Red 40 Lake. The commercial Lake pigment contained nanoparticles, and this enhanced its coverage and saturation. Nevertheless, Red 40 cCNC-based pigments were competitive in the category of saturation and coverage, despite the lower surface area of the microbeads. This suggests that other factors might be at play in determining the optical

properties. Nanocrystal cellulose microbead refractive index, uniformity of particle size, and the scattering properties of the microspheres and nanocrystals in the microbeads might be responsible for the differences, though correlations were not established in this thesis. An extensive study of Red 40 nanocellulose pigment stability was conducted as a function of time and temperature over a range of fluids commonly used to formulate pigments for color cosmetics. The study used Red 40 Lake as a standard for comparison. Overall, the two pigment classes performed similarly. The color stability study was pushed into the domain of water as a host medium. Emphasizing Red 40, both the cellulose microbead and Lake pigments released dye to the host medium. Comparatively, the release of Red 40 from the cellulose bead was quantitatively less than from the Lake. It was discovered that Blue 1 and Yellow 5 desorbed from the cellulose microbead more readily than did Red 40. Theories and experimental data were advanced to explain the difference.

Studies were undertaken to understand the impact on the optical properties of binding anionic dye molecules to the $cCNC^{+}$ platform. The study relied on understanding the outcome of binding PDDA to the cCNC nanocrystal to make the PEC. Zeta potential and turbidimetry were used to find the range in which the PEC was stable against flocculation. Zeta-potential analysis and turbidimetry revealed that stable dispersions could be obtained for both negative and positive potentials of the PEC. In the end, a concentration of 14% w/w PDDA was recommended to give $cCNC^{+}$ concentrations that were stable against agglomeration. Having established conditions for stability of the $cCNC^{+}$ platform, perturbations to the optical response to binding of the different dyes to the PEC were studied. All dyes exhibit a hypsochromic shift in the absorption maximum when bound to $cCNC^{+}$. The change in the spectral response adds new information on how the CNC pigment particles might respond to changes in the polarizability (refractive index) of the host medium.

Hyperspectral imaging (HSI) was introduced to examine the spatial distribution of dyes over the surface of the CNC microbeads. The technique was also shown to provide additional insight into dye desorption and competitive binding in aqueous media. On average, dye molecules appear to be uniformly distributed over the surface of the microbeads for Red 40, Blue 1 and Yellow 5. With minor exceptions, this state holds true for binary combinations of dye. Competitive binding studies were undertaken. These studies focused on the release and uptake of Red 40 and Blue 1 from their respective homoleptic dye complexes. Uptake of blue dye by red

microbeads was favored, a situation that likely reflects in part the lower binding affinity of Blue 1 at the surface of the cCNC$^+$ platform. The presence of a well-defined isosbestic point in these competitive exchange reactions suggested an equilibrium between binding and release.

5.2 Future Work

Currently, the CNC-based pigments produced are made with cCNC, PDDA, and anionic dyes. While cCNC is considered 'green' and biodegradable, there is interest to replace cationic PDDA.[1] Possible polycation replacements include chitosan, polylysine, and cationic starches. The pressure to replace the FD&C dyes encourages more study of a wider range of botanically derived dyes.[2] The naturally derived green dye, sodium copper chlorophyllin (chapter 2) is an encouraging start. Studies here should include knowledge of the impact of co-agents that suppress oxidation and a detailed study of the impact of cCNC and cCNC$^+$ on natural dye photooxidative stability, and stability to pH and ionic strength.

The dynamics of the dye desorption and competitive binding need further development. Such studies would benefit from an exploration of the impact of adsorption isotherms as these would provide much desired thermodynamic data concerning binding and stability. We recommend studies that use advanced models that combine diffusion and kinetics, rather than the commonplace reliance on "standard" models. Studies might examine pH and ionic strength dependence in relation to dye concentration and the type of cCNC PEC. A push to examine the relevance of cCNC and cCNC+ microbeads as micro-reactors and drug delivery vehicles is encouraged.

5.3 References

1. Cosmetic Ingredient Review Safety Assessment of Polyquaternium-6 as Used in Cosmetics. https://online.personalcarecouncil.org/ctfa-static/online/lists/cir-pdfs/FR826.pdf.
2. Lehmkuhler, A.; Miller, M. D.; Bradman, A.; Castorina, R.; Chen, M.-A.; Xie, T.; Mitchell, A. E., Levels of FD&C certified food dyes in foods commonly consumed by children. *Journal of Food Composition and Analysis* **2022,** *112*, 104649.